Development of optical platforms for elucidating the intracellular molecular mechanisms and immune cell dynamics induced by multispectral near infrared laser

August 2020

Wataru Katagiri

A Thesis for the Degree of Ph.D. in Engineering

Development of optical platforms for elucidating the intracellular molecular mechanisms and immune cell dynamics induced by multispectral near infrared laser

August 2020

Graduate School of Science and Technology
Keio University

Wataru Katagiri

Abstract

This thesis aims to elucidate the mechanism of immune cells response to near-infrared (NIR) laser light *in vivo* and to investigate the potential applications of a new optical method, the NIR technique. The technique can be used to observe the migration of antigen-presenting cells (APCs) and the intracellular signals induced by NIR lasers in cell culture systems in real-time.

Fluorescent nanoparticles for the non-invasive observation of vaccines were prepared by binding ovalbumin, an antigen, to silicon nanoparticles with diameters of 20 nm and 100 nm and labelling them with a zwitterionic NIR fluorescent molecule. In mouse models, the vaccine reached the lymph nodes via the lymphatic vessels and was quantitatively observed. The results showed that the fluorescent nanoparticles were superior to existing methods and were useful for tracking APCs.

In order to elucidate the molecular mechanism, the absorption spectrum of cytochrome C oxidase, a candidate photoreceptor among intracellular proteins was simulated. Calculation of absorption wavelengths using time-dependent density functional theory (DFT) suggested that in addition to the known visible region, absorption peaks exist in the NIR region of around 961 nm and 1319 nm.

In addition, an experimental system to observe the behaviour of intracellular molecules in real time by simultaneously irradiating them at 1064 nm and 1270 nm was established. The results showed that the combination of 1064 nm at 300 mW/cm^2 and 1270 nm at 50 mW/cm^2 irradiance inhibited the accumulation of intracellular signal transmitters.

In summary, this study developed two novel optical systems for observing the behaviour of immune cells in response to NIR laser light, revealing the effect of light on biological immunity. This system can be applied to other wavelengths, cell types and intracellular molecules, and is expected to provide a platform for clarifying the biological effects of NIR light.

List of Abbreviations

2D	Two dimensional
3D	Three dimensional
5-ALA	5-aminolevulinic acid
ACF	Autocorrelation function
AFM	Atomic force microscopy
AIC	Akaike information criterion
ANOVA	Analysis of variance
AP-1	Activator protein 1
APC	Antigen presenting cell
ATP	Adenosine triphosphate
B3LYP	Three-parameterized Becke-Lee-Yang-Parr
BCG	Bacillius Calmette-Guerin
BSA	Bovine serum albumin
CDC	Center for Disease Control and Prevention
cDC	Clasiccal dendritic cell
CGMP	Guanosine 3',5' -cyclic monophosphate
CI	Confidence Interval
CNS	Central nerve system
CO	Carbon monoxide
CPS	Capsular polkysaccharide
Cy5	Cyanine 5
Cy7	Cyanine 7
Da	Dalton
DAG	1,2-diacylglycerol
DC	Dendritic cell
DIW	Distilled water
DMSO	Dimethyl sulfoxide
EDTA	Ethylenediaminetetraacetic acid
EM	Electron microscopy
EMA	European Medicine Agency

ER	Endoplasmic reticulum
ETC	Electron transport chain
FDA	Food and Drug Administration
FMO	Fluorescence minus one
FOV	Field of view
FOXO	Forkhead box O
GGA	Generalized gradient approximation
GigE	Gigabit Ethernet
H&E	Hematoxylin-and-eosin
HD	Hydrodynamic diameter
HOMO	Highest occupied molecular orbital
HPV	Human papillomavirus
ICG	Indocyanine green
id	Intradermal injection
Ig	Immunoglobulin
IP3	Inositol triphosphate
IR	Infrared
ITAM	Immunoreceptor Tyrosine-based Activation Motif
iv	Intravenous injection
LDA	Local density approximation
LED	Light emitting diode
LLLT	Low level laser therapy
LPS	Lipopolysaccharide
LSDA	Local spin density approximation
LUMO	Lowest unoccupied molecular orbital
MB	Methylene blue
MGH	Massachusetts General Hospital
migDC	Migratory dendritic cell
MO	Molecular orbital
MW	Molecular weight
NADH	Nicotinamide adenine dinucleotide
Nd:YAG	Neodymium-doped yttrium-aluminium-garnet

Nd:YVO_4	Neodymium-doped yttrium orthovanadate
NF-κB	Nuclear factor-kappa B
NIR	Near Infrared
NO	Nitric oxide
OVA	Ovalbumin
PET	Positron emission tomography
PpIX	Protoporphyrin-IX
ROI	Region of interest
ROS	Reactive oxygen species
RT	Room temperature
SBR	Signal-to-background ratio
SD	Standard deviation
SEM	Standard error
SiNP	Silica nanoparticle
SOD	Superoxide dismutase
TBR	Tumor-to-background ratio
TCR	T cell receptor
TDDFT	Time dependent density functional theory
TEM	Transmission electron microscopy
TLR	Toll-like receptor
TRP	Transient receptor potential
UK	United Kingdom
US	United States
ZW700-1C	Zwitterionic 700-1C
ZW800-1C	Zwitterionic 800-1C

Contents

Chapter 1

Introduction

1.1 Background of the study

Human beings have been combating infectious diseases since the first vaccine was created in the late 18th century. The mass vaccination programme targeting influenza vaccine is one of the most successful examples in modern medical history, preventing millions of infections worldwide each year. Generally, these vaccines contain chemical compounds, called adjuvants, that enhance immune response against vaccine antigens. Together with the vaccine, the chemical adjuvant molecules contribute to protecting human health. Although the safety of adjuvants is guaranteed by clinical trials, because of the large number of subject populations, safer and more affordable adjuvants are highly anticipated. Recent studies reported that brief exposure of skin to near-infrared (NIR) laser light, at wavelengths of 1064 nm, 1258 nm and 1301 nm, facilitates stronger immunity against pathogens.[1,2] Thus, the adjuvant effect of physical light has shown great promise as an alternative tool to chemical adjuvants.

To date, several key actions of immune cells against NIR light at 1064 nm have been reported. Morse *et al*. demonstrated that NIR laser light enhances the migration of dendritic cells, which are enriched in skin epidermis and dermis, and initiates a protective immune reaction against pathogens.[3] Interestingly, these adjuvant effects are created only by continuous wave laser light, not by pulsed lasers.[1,3] Kimizuka *et al*. reported that mast cell function is deeply involved in the adjuvant effects of laser light. They showed that the activation of mast cells in the skin through the generation of reactive oxygen species (ROS) is necessary for dendritic cell (DC) migration. These characteristics of immune cells are essential factors in the

adjuvant effects of lasers; however, the detailed mechanism of action remains shrouded in mystery because of the lack of a tool that can observe the dynamics of immune cells and intracellular molecules in real time.

Recently, the physical interaction between light and biological tissue has attracted attention and has consequently been intensively investigated.[4–10] The action of cells or organs against light is called photobiomodulation. Up until now, the photobiomodulation effect on visible and NIR light below 1000 nm has been studied, meaning that evidence of photobiomodulation against NIR in ranges over 1000 nm is very limited.[11–13] NIR light between 1000 nm and 1300 nm is less absorbed by melanin; therefore, the method can be applied in clinical medicine irrespective of ethnicity or race.

The action mechanisms of photobiomodulation in the context of medicine have been partially revealed by previous research. For instance, it is known that the mitochondrial signal is an essential signal pathway involved in the action of photobiomodulation.[14,15] In this context, the generation of ROS is associated with mitochondrial activation. ROS are generally considered as essential intracellular molecules that maintain the homeostasis of cellular reactions. ROS control cell proliferation, effector functions and the resolution of effector functions (death).[16,17] Since a previous study using NIR also demonstrated the ROS function in the adjuvant effect of lasers,[18] it is expected to be revealed in a real-time manner in order to determine whether NIR light affects the cellular signal pathways and is immediately followed by the generation of ROS.

The most profound mystery of photobiomodulation by NIR is the existence of photoreceptor molecule(s). Many studies have indicated the possible photoreceptor molecule of visible light; however, the NIR range is insufficiently understood. The difficulty in discovering the proper photoreceptor is attributable to the complexity of intracellular molecules, including the cytosol. As the cytosol is a veritable ocean of proteins, peptides, ions and organelles, it poses challenges to the experimental methodologies used to identify unique photoreceptors.

To address these problems, this study reports two novel optical systems to elucidate the mechanisms of immune cells response to NIR laser light *in vivo* and *in vitro*. An NIR imaging system accompanied by a zwitterionic NIR fluorophore provided a non-invasive observation method to visualize migration of antigen presenting cells (APCs), while a dual laser illumination system was used to elucidate the intracellular signals of mouse-derived T cells induced by the NIR laser. Density functional theory (DFT) was applied to determine the absorption spectrum with potential photoreceptor molecules.

1.2 Significance

In this thesis, several unique and significant points are presented. First, a multispectral imaging system together with a novel NIR fluorophore were established. Compared to conventional NIR fluorophores, the novel NIR zwitterionic fluorophore shows a high signal-to-noise ratio and low toxicity.[19] These unique characteristics of the zwitterionic fluorophore provide a safe imaging system with clear fluorescent images in a real-time manner. Accordingly, this study performed, for the first time, a vaccine visualisation technique via the use of the novel NIR zwitterionic fluorophore and a multispectral imaging system, with no danger of toxicity and a sustained signal over time.

Second, DFT was applied to estimate the absorption among two proteins: superoxide dismutase 1 (SOD1) and cytochrome C oxidase (COX). DFT is a method of computational chemistry used to estimate the energy state of subject molecules. The calculation discovered that COX absorbs light in the NIR range. The result indicated that the absorption peaks at 961 nm and 1319 nm dissociate nitric oxide (NO) molecules from COX binding sites. NO is a key molecule that leads to various biological reactions in the human body. This new finding could accelerate further studies on the mechanisms of photobiomodulation and immune reaction.

Third, in the optical system used to observe intracellular molecules, two laser lights, 1064 nm and 1270 nm, were combined into one beam. This enabled the illumination of T cells at two different wavelengths simultaneously. The combined beam was given a gradient towards two different directions. By doing so, the system could illuminate a countless number of T cells at one time, realising high-throughput analysis with numerous combinations of irradiances in one experiment. A two-way gradient beam gave us the chance to determine the combination of irradiances that induces the biggest changes in fluorescence compared with the control group. The result suggested that a combination of 300 mW/cm^2 at 1064 nm and 50 mW/cm^2 at 1270 nm suppresses the accumulation of ROS and calcium ions immediately after the laser irradiation, yielding a new aspect of photobiomodulation. Future application of NIR lasers could determine the best irradiance by using the proposed system.

In short, this study developed an optical system for observing the behaviour of immune cells induced by NIR laser light, revealing the effect of light on biological immunity. This system can be applied with other wavelengths, cell types, and intracellular molecules, and is expected to provide a platform for clarifying the biological effects of NIR light.

1.3 Structure of the thesis

The structure of this thesis is as follows.

Chapter 2 describes the general background of the study. The basic immune response and the immunostimulatory effect of NIR lasers, as well as their mechanisms of action, are outlined. The state of the art of the photobiomodulation induced by lasers is also explained. In addition, the properties of the NIR zwitterionic fluorophore and the NIR imaging system used in this study, as well as the outcomes of previous studies, are described. Lastly, recent NIR fluorophore trends and the applications of the NIR imaging system are reviewed.

Chapter 3 proposes a new system to observe the behaviour of intradermal vaccines in a non-invasive manner in a mouse model using fluorescent nanoparticles and a multi-channel NIR imaging system. By measuring the fluorescence intensity from lymph nodes at different timepoints, the concentration of vaccine molecules in the lymph nodes was estimated. Histological and flow cytometry analysis of the lymph nodes were performed to evaluate the validity of the novel method.

Chapter 4 introduces the basis of DFT, which has recently been widely used in the field of computational chemistry. Further, the molecular energy level and absorption spectra of COX, which has been considered as a candidate of photoreceptor, applying DFT, are discussed. Two notable absorption wavelengths – 961 nm and 1319 nm – are reported.

Chapter 5 proposes a new method to irradiate cultured cells with dual-wavelength NIR laser beams, 1064 nm and 1270 nm, with a gradient in the intensities. The system aims to reveal the action of intracellular ROS and calcium ions in response to NIR laser light, and to determine the best combination of laser irradiances at the two different wavelengths. In this way, the best combination of the two laser irradiances is proposed for future application.

Chapter 6 summarises the results and refers to the future development of NIR laser applications. Specifically, the potential applications in cancer therapy are discussed.

References

1. Kashiwagi, S. *et al.* Near-infrared laser adjuvant for influenza vaccine. *PLoS One* **8**, (2013).
2. Kimizuka, Y. *et al.* Semiconductor diode laser device adjuvanting intradermal vaccine. *Vaccine* **35**, 2404–2412 (2017).
3. Morse, K. *et al.* Near-Infrared 1064 nm Laser Modulates Migratory Dendritic Cells To Augment the Immune Response to Intradermal Influenza Vaccine. *J. Immunol.* ji1601873 (2017) doi:10.4049/jimmunol.1601873.
4. Khokhlova, A. *et al.* The photobiomodulation of vital parameters of the cancer cell culture by low dose of Near-IR laser irradiation. *IEEE J. Sel. Top. Quantum Electron.* **25**, 1–11 (2019).
5. Kim, H. P. Lightening up Light Therapy- Activation of Retrograde Signaling Pathway by Photobiomodulation. 491–496 (2014).
6. De Freitas, L. F. & Hamblin, M. R. Proposed Mechanisms of Photobiomodulation or Low-Level Light Therapy. *IEEE J. Sel. Top. Quantum Electron.* **22**, 1–37 (2016).
7. Hamblin, M. R., Nelson, S. T. & Strahan, J. R. Photobiomodulation and Cancer: What Is the Truth? *Photomed. Laser Surg.* **XX**, pho.2017.4401 (2018).
8. Hamblin, M. R. Mechanisms and applications of the anti-inflammatory effects of photobiomodulation. *AIMS Biophys.* **4**, 337–361 (2017).
9. Hamblin, M. R. Shining light on the head: Photobiomodulation for brain disorders. *BBA Clin.* **6**, 113–124 (2016).
10. Amaroli, A., Ferrando, S. & Benedicenti, S. Photobiomodulation Affects Key Cellular Pathways of all Life-Forms: Considerations on Old and New Laser Light Targets and the Calcium Issue. *Photochem. Photobiol.* **95**, 455–459 (2019).
11. Wang, Y., Huang, Y. Y., Wang, Y., Lyu, P. & Hamblin, M. R. Red (660 nm) or near-infrared (810 nm) photobiomodulation stimulates, while blue (415 nm), green (540 nm) light inhibits proliferation in human adipose-derived stem cells. *Sci. Rep.* **7**, 1–10 (2017).
12. Fernandes, K. P. S. *et al.* Photobiomodulation with 660-nm and 780-nm laser on activated J774 macrophage-like cells: Effect on M1 inflammatory markers. *J. Photochem. Photobiol. B Biol.* **153**, 344–351 (2015).
13. Lima, P. L. V. *et al.* Photobiomodulation enhancement of cell proliferation at 660 nm does not require cytochrome c oxidase. *J. Photochem. Photobiol. B Biol.* **194**, 71–75 (2019).
14. Hamblin, M. R., Huang, Y. Y., Sharma, S. K. & Carroll, J. Biphasic dose response in low level light therapy - an update. *Dose-Response* **9**, 602–618 (2011).
15. Huang, Y. Y., Chen, A. C. H., Carroll, J. D. & Hamblin, M. R. Biphasic dose response in low level lightherapy. *Dose-Response* **7**, 358–383 (2009).
16. Kamiński, M. M. *et al.* T cell Activation Is Driven by an ADP-Dependent Glucokinase Linking Enhanced Glycolysis with Mitochondrial Reactive Oxygen Species Generation. *Cell Rep.* **2**, 1300–1315 (2012).
17. Sena, L. A. *et al.* Mitochondria Are Required for Antigen-Specific T Cell Activation through Reactive Oxygen Species Signaling. *Immunity* **38**, 225–236 (2013).

18. Kimizuka, Y. *et al.* Brief Exposure of Skin to Near-Infrared Laser Modulates Mast Cell Function and Augments the Immune Response. *J. Immunol.* ji1701687 (2018) doi:10.4049/jimmunol.1701687.
19. Katagiri, W. *et al.* Real-Time Imaging of Vaccine Biodistribution Using Zwitterionic NIR Nanoparticles. *Adv. Healthc. Mater.* **8**, e1900035 (2019).

Chapter 2

Immunobiology, vaccines and photobiomodulation by laser

Immunity is a host defence mechanism that resists invasions of foreign pathogens, viruses, toxins or malignant tumour cells that potentially lead to life-threatening diseases. The complexity of the immune system is highly regulated; however, many diseases and unexpected symptoms, such as allergies and rheumatoid arthritis, are caused by immunological disorders. Furthermore, although many studies are seeking to understand the complexity of immunity, a whole picture of the immune system has yet to be revealed, since the immune system is dynamically and intricately orchestrated.

This chapter, at first, briefly explains different actors of the immune system, such as immunoglobulin, T cells, B cells and APCs. Both innate and adaptive immunity are explained. Second, the chapter focuses on vaccinations, which have been contributing to the safeguarding of human health for more than two centuries. Finally, essential molecular mechanisms behind the immune system are noted.

2.1 Host defence immunity

2.1.1 Immunoglobulins

Immunoglobulins (Igs) are secreted by B cells. Human immunoglobulins are categorised into five groups: IgG (IgG1, IgG2, IgG3, IgG4), IgA, IgM, IgD and IgE.[1] The IgG isotype comprises the majority of human immunoglobulin, occupying 75% of the total volume of immunoglobulin in healthy human adult serum.[2] The typical molecular weight (MW) is 150,000 Dalton (Da). IgG, having a strong affinity with antigens, plays a role as a major defence against viral particles (Figure 2.1a). IgA is the second major immunoglobulin and is mainly secreted in mucus. IgA occupies 15% of the total volume of human immunoglobin. In mucosal tissue, IgA, together with IgG, protects against common viral infectious diseases, such as influenza[3] or hepatitis.[4] IgM is the third major immunoglobulin and has the largest MW: 985,000 Da[5] (Figure 2.1b). It plays a role in the immediate reaction against microbial infections, such as by pneumococcus,[6] staphylococcus aureus,[7] pseudomonas aeruginosa[8] or salmonella,[9] by cooperating with IgG and IgA. The fourth major immunoglobulin superfamily is IgD, which occupies approximately 0.2% of total human immunoglobulin.[10] Although IgD was discovered more than 50 years ago, its role is not well understood.[10] A recent study revealed that IgD is secreted by B cells that migrate in upper respiratory mucosa and show strong binding activity to lipopolysaccharide (LPS), capsular polysaccharide (CPS), Moraxella catarrhalis, and influenza type a and b.[11] The remaining portion of human immunoglobin is occupied by IgE, which is associated with allergic reactions. IgE is recognised by various APCs and mast cells, which store and release histamine, inducing acute inflammatory reactions.[12]

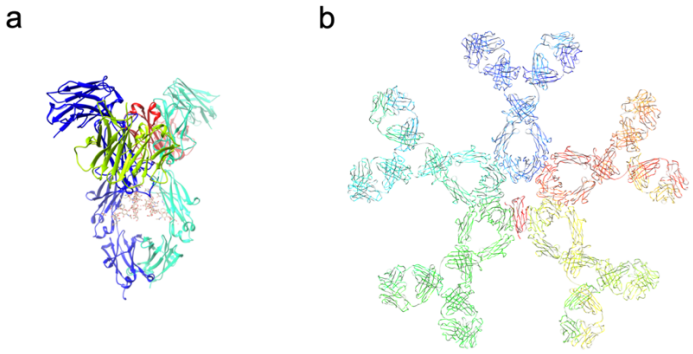

Figure 2.1 Molecular structure of (a) human IgG1 and (b) human IgM. The shown crystal structure of IgG1 reacts against HIV-1 virus[13]. PDB: (a) 1HZH, (b) 2RCJ. The images were depicted using UCSF Chimera version 1.11.2 (University of California, USA).

2.1.2 Antigen presentation

To deal with foreign pathogens, the human body has two host defence systems: innate and adaptive immunity. Antigen presentation is one of the most important activities in the adaptive immune system and is carried out by APCs. Notably, DCs, macrophages and B cells are classified as professional APCs.[14] These professional APCs are highly populated in skin dermis and epidermis in order to recognise pathogens and initiate an immune response against invasion.[15] The APCs have a unique peptide – major histocompatibility complex class II (MHC class II or MHC-II) – which is presented to T cell receptors (TCRs) on $CD4^+$ T cells and naive T cells. Once the professional APCs recognise an exogenous antigen, such as parasites, bacteria or toxins, the antigen is taken up by endocytosis into the APCs' cytosol. The antigen proteins are then degraded into small peptides by hydrolases in lysosomes and then loaded onto MHC-II molecules, which are assembled in the endoplasmic reticulum (ER). The peptide-loaded MHC-II molecules are then displayed on the cell surface.[16]

Especially among APCs, DCs are the only subset that can communicate with naive T cells, and they therefore play a significant role. Figure 2.2 shows the main actors of DC subsets. In skin, a large number of migratory dendritic cells (migDCs) are enriched. The moment they recognise foreign pathogens, they migrate into secondary lymphoid tissues, typically lymph nodes (LNs), through lymphatic vessels driven by chemokines, such as CCL19 and CCL21.[17,18] The migDCs are able to present the peptides to $CD4^+$ T cells in the LNs, which leads to the activation of the adaptive immune system.[19,20]

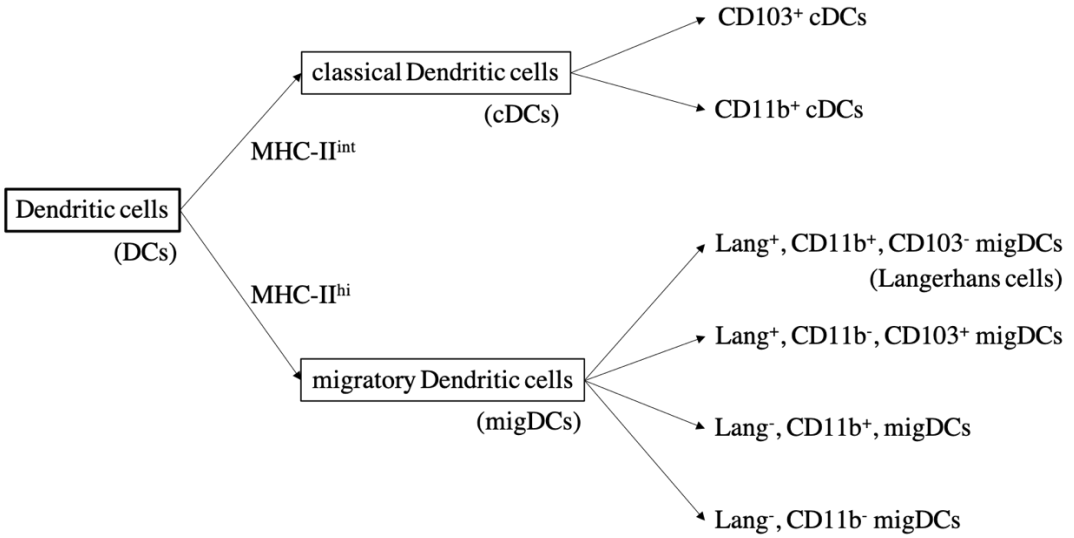

Figure 2.2 Classification of dendritic cell subsets based on their surface markers.

2.2 Vaccine

2.2.1 History of vaccine development

Thanks to modern medical advancements, beginning with the invention of the first vaccine (against smallpox) in 1796 by Dr. Edward Jenner in England, humanity has been armed with the ability to combat infectious diseases. Smallpox was at one time the most dreadful infectious disease confronting humankind, with an overall fatality rate of 30%.[21] Two hundred years after the invention of the smallpox vaccine, however, humanity has defeated the virus, with the World Health Organization (WHO) declaring its eradication in 1980. Various other vaccines have been developed, including vaccines against cholera (in 1896), tuberculosis (1921), diphtheria toxoid (1923), yellow fever (1935), influenza (1936), polio (injectable: 1955, oral: 1962), measles (1963), mumps (1967), rubella (1969), rabies (1980), hepatitis B (1981), typhoid (1989), hepatitis A (1996), rotavirus (1999), HPV (2006), malaria and dengue fever (2015).[22] Although smallpox is thus far the only infectious disease among humans that the WHO has declared to be eradicated, many other diseases have been brought under control. For example, more than 206,000 cases of diphtheria toxoid, which has a 7% mortality rate, were confirmed in the US in 1921, but no cases were reported in 2016.[23,24]

The administration route for a vaccine varies depending on the molecules involved. A few vaccines (polio, BCG and rabies vaccines) are administrated orally or intradermally. Most modern vaccines are administrated subcutaneously or intramuscularly. Arakane *et al*. reported that intradermal administration of the influenza vaccine had higher efficacy; however, the problem of precise injection remains.[25,26] Therefore, even though the modern vaccine has been contributing to human health, its efficacy is not fully understood, and its administration route has yet to be optimised.

2.2.2 Vaccine adjuvants and the potential risk of adverse events

Many antigens currently under investigation do not alone increase inherent immunity efficiently enough. In order to improve the efficacy of vaccines, many have been mixed with chemical compounds called adjuvants (from the Latin, *adjuvare*: to help) since the 1920s.[27] Together with vaccine molecules, adjuvants induce a higher antibody titre for a longer period, which indicates that adjuvants culminate in sustained immune responses.[27] Besides their efficacy, there have been concerns about the safety of adjuvants with respect to their

enhancement of immunologic reactions because the whole picture of adjuvant kinetics is not yet fully understood. Therefore, currently, the US Food and Drug Administration (FDA) has approved only five chemical adjuvants (Table 1), mainly because of concerns over their negative effects.

AS03 (GlaxoSmithKline, GSK, United Kingdom) is an immunologic adjuvant used with the H1N1 influenza A vaccine (Pandemrix®, GSK) that was approved in 2009 to assist European countries and the US, which were struggling with a flu pandemic.[28] Regarding the pandemic, the US Centers for Disease Control and Prevention (CDC) estimated 60.8 million cases and 12,469 deaths in the US alone.[29] The vaccine was therefore widely used all over the world; however, hundreds of narcolepsy cases were subsequently reported in European countries that were linked to the use of AS03.[30,31]

Another example of adjuvants is AS04, which is mixed with the HPV vaccine. In 2009, the Japanese government introduced Cervarix (GSK) and Gardasil (Merck & Co., US) and established a guideline that recommended that women over 10 years old take the vaccine. After severe side effects, such as syncope, complex regional pain syndrome and impaired mobility, were widely reported in 2013, the government suspended the campaign.[32,33]

Even though the association between adjuvants and reported adverse events is still controversial, the safety of adjuvants remains the most important factor for clinical usage. In fact, many side effects have been reported with adjuvant candidates under development.[34] Therefore, providing efficient and safe vaccine adjuvants is highly desired.

Table 1. Adjuvant compounds used in humans[35–38]

Name	Company	Compound	Target/Induction
AS03	GSK	Oil, emulsion, squalene	CXCL10
AS04	GSK	Monophosphoryl lipid A	TLR4
Alum	varies	Aluminum salt	ITAM
MF59	Novartis	Oil, emulsion, squalene	CXCL10
CpG 1018	Dynavax	Cytosine phosphoguanine	TLR9

2.2.3 Development of laser adjuvant technology

Recent studies have revealed the potential application of continuous wave (CW) NIR laser light as a vaccine adjuvant.[28,39–41] In these studies, the effect of vaccine adjuvants was evaluated with respect to the amount of cytokine in skin tissue, IgG in mice serum, DC migration and the fertility rate of mice after influenza infection; this type of evaluation is called a challenge study. A 5.0-W/cm^2, 1064-nm CW laser irradiation of a 0.2-cm^2 spot of mice skin for 1 min immediately after vaccination with an inactivated influenza H1N1 vaccine demonstrated the adjuvant effect with no adverse effects.[39] The adverse effect of the laser vaccine adjuvant was evaluated for skin damage via histological examination by hematoxylin-eosin stain (H&E stain) and the infiltration of polymorphonuclear leukocytes (PMN) in the dermic layer.[39,41] Hyperthermia was another concern with invisible laser irradiation. However, it was shown that major dermal and epidermal cells, keratinocytes, could tolerate laser irradiation at 47.0˚C for 1 min. Other parameters, such as 1061-nm, 1258-nm and 1301-nm wavelengths, have also yielded positive effects.[41]

Although there are high expectations for laser vaccine adjuvant technology in clinic, the detail mechanism of action remains under investigation. The latest studies have pointed out the relationship between anti-viral immune response and DC migration from the skin into secondary lymphoid tissues, as well as ROS generation by laser irradiation.[42,43] However, since the molecular pathways are so complex, discovering the whole picture is challenging.

To date, photobiomodulation by NIR light has been discussed and applied in clinic as low-level laser therapy (LLLT). Typically, 1 mW/cm^2 to 5 W/cm^2 of NIR light shows diverse biological effects, including wound healing, pain relief, suppression of inflammation and regeneration of tissue.[44–46] The use of NIR light has been explored for a wide array of therapeutic purposes during recent decades. Even though the detail mechanisms of LLLT have not been revealed, the mitochondrial electron transport chain (ETC) is thought to play an important role in photobiomodulation and may be linked to ROS generation.[47,48] In the next section, more details about molecular dynamics in cells are discussed.

2.3 Cellular molecular biology

2.3.1 Mitochondrial function

Mitochondria in the cell cytosol generate an energy unit called adenosine triphosphate (ATP) using oxygen and are therefore referred to as an energy factory. ATP is produced by two major pathways: glycolysis and the tricarboxylic acid (TCA) cycle. Under aerobic respiration conditions, glycolysis is the dominant system for generating ATP, whereas the ETC dominates under anaerobic respiration.[49]

Glycolysis is a metabolic pathway that is common to almost all organisms, and its reaction takes place in the cytoplasm. The glycolysis process breaks down glucose into organic acids, such as pyruvate, and converts the high binding energy contained in glucose into a form that is easy for organisms to use. It generates two ATP molecules and two nicotinamide adenine dinucleotide (NADH) molecules out of one glucose molecule. Since the NADH is used in the ETC, glycolysis is considered to have important roles in both aerobic and anaerobic conditions. The pyruvate is transformed into acetyl CoA, which is also metabolised in the TCA cycle.[49]

The TCA cycle is the most important biochemical cycle for aerobic metabolism and can be found in all organisms that breathe oxygen. Whole reactions are carried out in the mitochondrial matrix. Acetyl CoA, which is produced by glycolysis and beta-oxidation of fatty acids, is incorporated into this cycle and is oxidised to produce NADH. Then, NADH is used in the ETC, which also generates ATP. Five transmembrane complexes, I to V, in the inner mitochondrial membrane are involved in the ETC (Figure 2.3).[50]

Notably, complex IV is called cytochrome c oxidase (COX) and has attracted attention as a key molecule in the context of photobiomodulation (Figure 2.4). COX in the ETC in the mitochondria has been regarded as the primary source of mitochondrial ROS across organisms,[51] while ROS can be generated across complexes I to IV in the ETC and other components in the mitochondria.[44,52–55]

Recent studies have revealed that many immune-related reactions, including diseases and the aging process, are highly dependent on the mitochondrial function. Even the therapeutic outcomes of cancer immunotherapy are affected by T cell mitochondria.[56–59] Therefore, it is essential to observe the mitochondrial condition in order to depict the immunologic reaction induced by medicines or therapies.

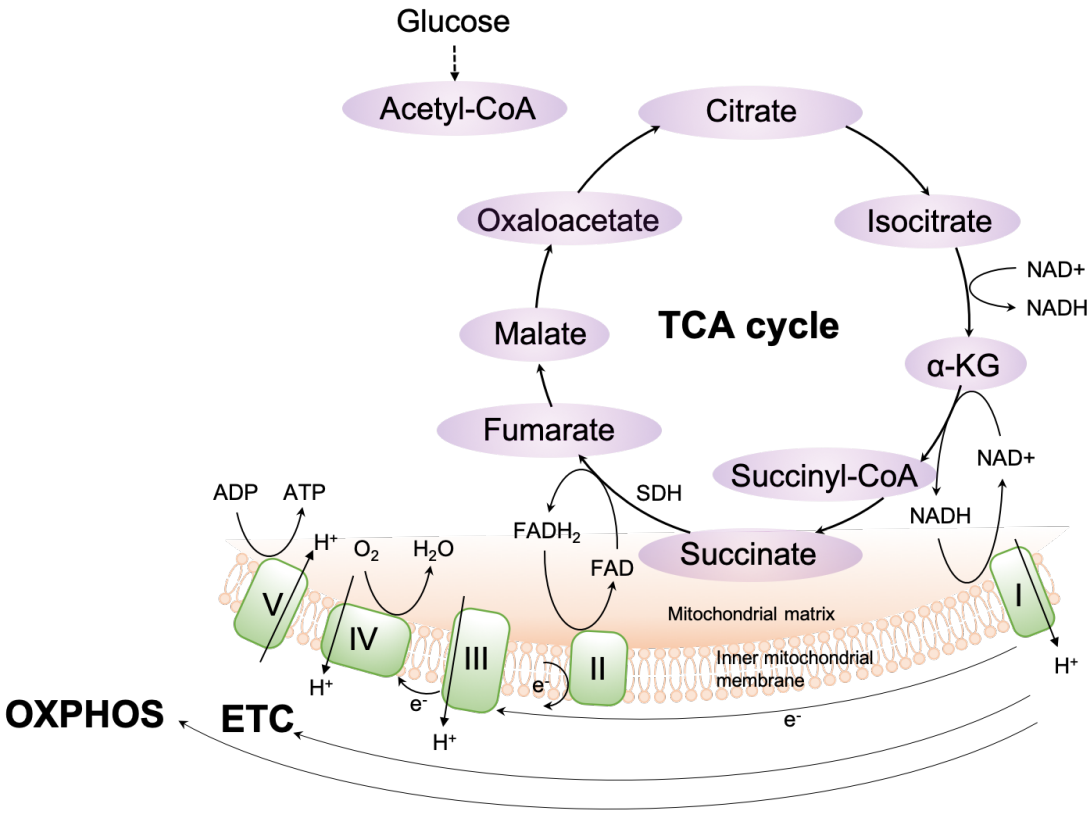

Figure 2.3 Correlation of TCA cycle and ETC reaction in the mitochondrial matrix and the inner membrane.[50,56] An Acetyl CoA is taken into the TCA cycle. The cycle produces 1 ATP, 3 NADH, 1 $FADH_2$, 2 CO_2 and 3 H^+. NADH and $FADH_2$ are required to transfer electrons in the ETC, which generates an electrochemical gradient across the inner mitochondrial membrane. The whole metabolic pathway, which is linked to the ETC and generates ATP, is called oxidative phosphorylation (OXPHOS)[56].

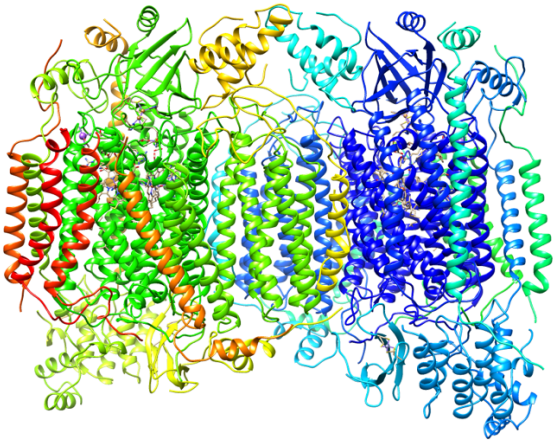

Figure 2.4 Molecular structure of cytochrome c oxidase (COX). PDB: 5X1F.

2.3.2 Calcium ion and reactive oxygen species

ROS, mainly generated in the mitochondrial respiratory chains of animal cells, are fundamental signals for cells that regulate cell differentiation, autophagy, apoptosis, etc.[60–63] ROS are also considered as a cause of oxidative stress and damage. The main actors are hydroxyl radicals, hydrogen peroxide and superoxide radicals (Figure 2.5).[64] In normal cells, the balance between the generation and degradation of ROS is maintained at a certain level by enzymes such as superoxide dismutase (SOD).[65]

Calcium (Ca^{2+}) also has multiple important roles in regulating cellular functions, including survival, death, locomotion, secretion, metabolism and gene expression.[66] Extracellular space is enriched with 1-2 mM Ca^{2+}. Cells transport the Ca^{2+} via several channels, such as voltage-activated channels and purinergic ionotropic receptors with both selective and non-selective features.[67] Ca^{2+} is taken up into the cell and stored in the ER. The Ca^{2+} concentration in the ER is maintained at 300 µM-1 mM. On the other hand, the Ca^{2+} concentration in the cytosol is as low as 50–100 nM.[67]

Many studies have reported that the dysfunction of mitochondria or disturbances of Ca^{2+} and ROS homeostasis are associated with different diseases, such as Alzheimer's disease, Parkinson's disease, arteriosclerosis, hypertension or cancer.[68–73] In the meantime, it has also been indicated that mitochondria-targeted drugs can be applied to treat these critical diseases or disorders.[74,75]

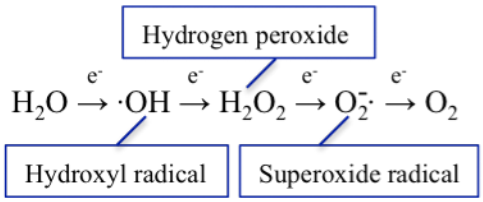

Figure 2.5 Reactive oxygen species (ROS).[64]

2.4 Lasers in history

A laser is an electronic device that emits coherent and directional light. Although the word *laser* is widely recognised, it is actually an acronym for 'light amplification by stimulated emission of radiation'.[1]

Laser light is produced from a difference in energy levels. When atoms or molecules absorb energy from the outside, they move from a lower energy state to a higher energy state. This higher energy state is called the excited state. The excited state is unstable and soon returns to a lower energy state. This is called transition. When transition happens, light corresponding to the energy difference is emitted from the atoms or molecules. This phenomenon is called spontaneous emission. The emitted light collides with other atoms in a similarly excited state, triggering a similar transition. This induced emitted light is called induced emission or stimulated emission.

The concept of induced emission was postulated by Albert Einstein in 1916. In 1954, Charles Townes invented an ammonium-gas-based stimulated emission system of microwaves. The system was named *maser*, which stands for 'microwave amplification by stimulated emission of radiation'. He and his colleagues received the Nobel Prize in Physics for the development of the maser in 1964. The first laser was invented by Theodore Maiman in 1960. Maiman's laser used a solid ruby crystal. In the 1960s, other lasers were developed using a variety of light sources, including CO_2 gas and neodymium-doped yttrium-aluminum-garnet (Nd:YAG).

Concerning medical applications, the CO_2 laser was the first light source applied in clinic. The CO_2 laser generates 10,600 nm of infrared light, which penetrates 0.03 mm of skin.[76] The energy of this light is directly transformed into heat because of the absorption by water. In 1966, Thomas Polanyi and Geza Jako successfully removed a glioma using a CW CO_2 laser light as a scalpel to minimise patients' blood loss.[77] Since then, many aspects of lasers have been developed. For instance, CW 1064-nm Nd:YAG lasers have been used for endoscopic treatments, whereas pulsed wave (PW) lasers are used for ablation.[78] Different lasers have dominated in different areas, such as ophthalmology, dermatology, oncology and cardiology.[78] A century after Einstein unveiled the concept of induced emission, lasers are now being put to use in medical practice.[79–81]

2.5 Introduction of low-level laser therapy

Laser devices produce a high-power, monochromatic, coherent and collimated light beam. Various types of lasers have been put into practice to contribute to practical medicine.[82] Particularly these days, low-level lasers, less than 1 W/cm^2, have attracted attention for their utility in medical device applications, such as LLLT with visible-infrared (IR) lasers,[82] infrared neural stimulation (INS) with NIR lasers[83,84] and photodynamic therapy (PDT) with visible lasers.[85]

The history of light therapy, or phototherapy, began in ancient Egypt. Since as early as 2000 B.C., the Egyptians believed in a Sun god, which they called "Ra". At the same time, they also believed in a sort of connection between the Sun and their health. Evidence of the use of sunbaths to treat ancient Egyptian people have been documented.[86] In ancient Greece, around 400 B.C., legendary historians such as Herodotus and Hippocrates also recommended the use of sunbaths,[87] although no one could explain their scientific mechanisms. Surprisingly, the use of sunlight for medicine has been extensively studied in the 21st century with the expectation of developing a wide range of clinical applications.[88]

In the past half century, the development of innovative light sources has accelerated our understanding of phototherapy. The applications of LLLT for wound healing and for the reduction of acute inflammation have been reported since the 1960s.[89–91] In these studies, a variety of lasers and wavelengths were investigated, and their effectiveness was demonstrated; these include, for example, Helium-Neon (HeNe) lasers (632.8 nm), ruby lasers (694 nm), argon lasers (488 nm, 514 nm), krypton lasers (521 nm, 530 nm, 568 nm, 647 nm), diode lasers (660 nm, 810 nm, 980 nm) and Nd:YAG lasers (1064 nm).[91,92] In addition, various irradiances (W/cm^2), times and radiant exposures (J/cm^2) were also investigated.[93] Chow *et al*. summarised 16 randomised trials with a total of 820 patients to test the effect of LLLT on acute neck pain patients.[94] They concluded that LLLT reduces pain immediately after laser treatment, and that the effect continues for up to 22 weeks after the treatment. No severe adverse events were reported. Brosseau *et al*. performed randomised controlled trials with a total of 222 rheumatoid arthritis patients. The outcome also indicated the therapeutic effect of LLLT.[95] Interestingly, these studies suggested that the effects of LLLT are wavelength-dependent.[94,95]

Although different wavelengths of lasers have been investigated for therapeutic purposes, NIR light (650 to 1700 nm) has been used in medical procedures due to its unique physical properties: low scattering and high penetration depth in biological tissue, reduced

autofluorescence, a high signal-to-noise ratio for the imaging system compared with other wavelengths, and low absorption by melanin.[96–99] In addition, NIR light has shown minimum genotoxicity regarding ER stress.[100] Low-level NIR light, typically between 1 mW/cm^2 to 5 W/cm^2, also shows diverse biological effects, including pain reduction, suppression of inflammation and tissue regeneration.[44,46,52,101,102] These effects in the biological context are defined as photobiomodulation by LLLT.

Although many studies have been attempting to reveal the mechanisms of photobiomodulation by NIR LLLT, they are as of yet not fully understood. Notably, there are difficulties in finding photoreceptors. The most basic photoreceptors are located in the retina. However, human eyes are not able to recognise NIR or IR light, indicating the difficulty of discovering NIR photoreceptors and understanding the subsequent series of reactions. In the next section, an overview of intracellular molecular dynamics associated with NIR photobiomodulation is introduced.

2.6 Dynamics of intracellular molecules in low-level laser therapy

The beneficial effects of NIR light with regard to photobiomodulation are mediated by mitochondrial retrograde signalling, including ROS.[44,46,51,52,93,101–105] Even though it has not been proven that proteins in the ETC in the mitochondria are initial photoreceptors, COX has been regarded as the primary source of mitochondrial ROS across organisms,[51] while ROS can be generated across complexes I–IV in the ETC and other compartments in the mitochondria.[44,52–55] NIR light has been shown to alter cell metabolism, resulting in the generation of ROS[51,105] and in the activation of ROS-mediated retrograde signalling via the forkhead box O family (FOXOs), nuclear factor-kappa B (NF-κB), activator protein 1 (AP-1) and Myc.[51] Thus, mitochondrial ETC is regarded as a primary photoreceptor for NIR light.[105,106] Many other molecules, including guanosine 3',5' -cyclic monophosphate (CGMP), 1,2-diacylglycerol (DAG), inositol triphosphate (IP3), Ca^{2+}, nitric oxide (NO) and carbon monoxide (CO) are considered as secondary messengers initiated by LLLT.[107] It has also been reported that broadband NIR light (760–1440 nm) induces the formation of mitochondria-derived ROS and the subsequent increase in the redox potential in cultured human dermal fibroblasts.[107] Furthermore, 1064 nm of NIR light has been shown to modify the function of COX and to improve tissue oxygenation in humans.[108] NIR light generally increases the

generation of ROS, and 950 nm of NIR light has been reported to decrease mitochondrial membrane potential and ROS production,[109] suggesting that photobiomodulation could be dependent on the types of cells, the activation status of cells and laser parameters, including wavelengths, irradiances, treatment times and pulsations. However, few studies have investigated the interactions of NIR light at 1000–1400 nm with mitochondrial retrograde signalling to advance our understanding of the mode of action of this particular range of NIR light.

The effects of NIR light are also reported to be mediated by calcium signalling, which consists of a significant part of mitochondrial retrograde signalling.[44,46,51,52,101–105,107] Calcium plays multiple important roles in regulating the cellular function, including survival, death, locomotion, secretion, metabolism and gene expression.[66] NIR light at 633–980 nm has been largely reported to increase intracellular calcium,[110,111] while 810 nm of NIR light could normalise (decrease) the excessively high level of intracellular calcium in a pathological condition,[112] and 632.8[113] or 780 nm[113] of NIR light was reported to inhibit calcium uptake by the mitochondria depending on irradiance. Although the precise molecular mechanisms of action for this effect remain unclear, heat- or light-sensitive ion channels have been suggested to be involved in the modulation of calcium signalling in photobiomodulation.[111] In particular, ultraviolet (UV)-IR light was reported to modulate the function of transient receptor potential (TRP) channels, including TRPV1, TRPV2 and TRPV4.[111,114–116]

2.7 Photobiomodulation in T cells

T cells, which are essential lymphocytes in animals, are generated in the thymus and bone marrow and circulate through the blood flow and the lymphatic flow. The most important role of T cells is to recognise and eliminate foreign enemies and cancer cells in the blood flow and in other tissues. T cells express a unique marker on the cell surface, CD3. Their major subclasses express CD4 or CD8. $CD3^+$ $CD4^+$ T cells are called helper T cells, while $CD3^+$ $CD8^+$ T cells are called cytotoxic T cells.[16]

Accordingly, photobiomodulation on immune cells, including macrophages[117] and dendritic cells,[118] has been reported. Photobiomodulation in T cells has also attracted attention, since LLLT induces the proliferation of T cells.[119] Importantly, recent studies have consistently shown that ROS plays a critical role in regulating T cell functions, including T cell receptor (TCR) signalling, T cell proliferation, effector functions and resolution of effector functions

(death).[120,121] ROS are constantly generated in mitochondrial oxidative phosphorylation (OXPHOS) via electron leaks from the ETC in the T cells.[122] In particular, mitochondrial ROS have been shown to act on NF-κB and to stimulate the production of IL-2 and other pro-proliferative genes to combat exogenous pathogens or endogenous tumors.[120] On the other hand, it has been shown that ROS can upregulate FasL and induce T cell death,[123] and that prolonged ROS signalling can suppress T cell responses.[124] Thus, the maintenance of the adequate level of ROS with antioxidant systems within the cell is critical for preserving the integrity of T cell immunity. Similarly, cytosolic and organellar calcium concentrations are well known to control the effector functions of T cells. Calcium influx is mediated through a diverse array of receptor- or voltage-activated calcium channels in T cells.[103,125,126] Intracellular organelles, such as the ER, mitochondria and lysosomes, also express specific channels and transporters that contribute to calcium increase in the cytosol and uptake into these organelles.[67,127,128] The strength and duration of calcium signalling have been shown to activate different transcription programmes in a T cell subset-dependent manner and to determine unique functions, such as metabolism, proliferation, death, differentiation, cytokine secretion and cytotoxicity, of each subset of T cells.[67] Calcium and ROS signalling are tightly interconnected in T cells. For example, upon T cell activation, calcium enters the mitochondria and activates enzymes in the TCA cycle, increasing their production of ROS.[129] Calcium signalling-induced ROS generation has also been shown to play a role in IL-2 production in activated T cells.

In short, as described above, ROS and calcium signalling is critical for both T cell biology and mitochondrial retrograde signalling activated upon photobiomodulation. To investigate the consecutive reaction in T cells initiated by LLLT, it is essential to observe the dynamics of intracellular ROS and calcium signals.

2.8 Laser vaccine adjuvant

2.8.1 Mechanisms of laser adjuvant effect

Since the 1960s, LLLT has been explored for its potential application as a therapeutic device for pain relief or for the reduction of inflammation, among other conditions. Later, in the 2000s, the immunostimulatory effect of laser light, which is also called the adjuvant effect, was reported by a Russian team using a copper vapour laser, and by a US team using the second harmonic of an Nd:YAG laser (532 nm).[130] A US study reported the migratory facility of APCs,

revealed the contribution of the Nd:YAG laser to the acquired immune system, and confirmed the adjuvant effect at a laser irradiance of 0.78 mW/cm^2 and an irradiation time of 2 min, indicating minimally invasive and more practical conditions.[130] The visible light laser adjuvant has been reported as a promising technology, but it has the disadvantage that melanin and haemoglobin absorb light and convert it into heat in the skin of living tissues in a wavelength region shorter than 600 nm in visible light. For clinical application, it is desirable that the light used for the laser adjuvant be at least 600 nm, since it is a prerequisite that it can be used regardless of race. On the other hand, at wavelengths above 1400 nm, absorption by water in biological tissues is dominant, and light energy is converted into heat. Therefore, it is best to apply this method to NIR light in the range of 600 nm to 1400 nm.

Kashiwagi *et al*. proposed a new laser adjuvant system that uses a 1064-nm neodymium-doped yttrium orthovanadate ($Nd:YVO_4$) laser.[39] They confirmed the adjuvant effect of the combination of the laser and the inactivated H1N1 influenza vaccine. In a mouse model, various immune responses were observed in mice skin when the influenza vaccine was administered intradermally immediately after 5 W/cm^2 laser irradiation for 1 min. Particularly, the increased density of $CD11c^+$ dendritic cells in the epidermis and dermis 6 h after laser irradiation, the increased expression of proinflammatory cytokines in the skin, the increased anti-influenza antibodies (IgG, IgG1, IgG2c) in serum at 4 days after the mice were infected with the influenza virus, and the increased survival of mice at 15 days after the start of the challenge study were observed as hallmarks of the adjuvant effect. These results demonstrated the adjuvant effect of the 1064-nm NIR laser. In addition, subsequent studies have revealed several important molecular mechanisms that induce the NIR laser adjuvant effect. First, NIR laser irradiation enhances the expression of ROS in the mast cells and promotes cytokine release in the skin tissue.[42] In particular, CCL21 greatly influences the migration of APCs into skin tissues and lymphatic vessels. Laser light increases the concentration of CCL21 in skin tissues and promotes the migration of $CD103^+$ migDCs and $Lang^-CD11b^-$ migDCs into the lymphatic vessels, ultimately activating the antigen presentation response in the LNs.[43]

In addition to the NIR lasers at 1064 nm, similar adjuvant effects have been observed in semiconductor laser devices oscillating at 1258 nm and 1301 nm at an irradiance of 0.5-5 W/cm^2, conferring protection.[41] Semiconductor lasers are inexpensive (approximately $3000), small, lightweight and easy to operate. In addition, unlike conventional vaccines, there is no need for refrigerated storage, which is an advantage over existing vaccines in terms of production and transportation. Therefore, semiconductor lasers can be used around the world, regardless of region or climate.

2.8.2 Adverse effect of laser adjuvant

The laser adjuvant reaction proposed by Kashiwagi *et al*. utilises NIR at 1064 nm, and although it fits within the optical window, its irradiance is 2–5 W, which is a higher dose than the irradiance conditions assessed in previous studies in which the effect of LLLT was confirmed. One concern is the thermal side effects of irradiation, i.e. the burn caused by the prolonged exposure of the laser beam to the skin. In their report, in addition to the observation of the skin surface in a mouse model, the presence of inflammation and the infiltration of neutrophils into the dermis and epidermis were observed by H&E staining of the skin after laser irradiation, and the presence of heat damage was evaluated. Neutrophils are widely used in the evaluation of burn injuries because they are known to be induced by cytokines such as IL-1 and IL-8, which are released from heat-exposed cells and infiltrate skin tissue from blood vessels.[39,41,42,131] From these results, it was confirmed that no burn or inflammation occurred at least up to 96 h after laser irradiation.

Heat damage generated from laser light is also one of the major concerns for patients. It is not easy to determine the safety threshold regarding heat *in vivo*; however, Katagiri *et al*. proposed an acute heat damage threshold by using cultured keratinocytes *in vitro* (Figure 2.6).[132] A short duration, less than 5 sec, is tolerable if the temperature is lower than 50–54˚C. On the other hand, the temperature should be lower than 47˚C when irradiation continues for 1 min. These findings could be useful to determining the best condition of laser illumination.

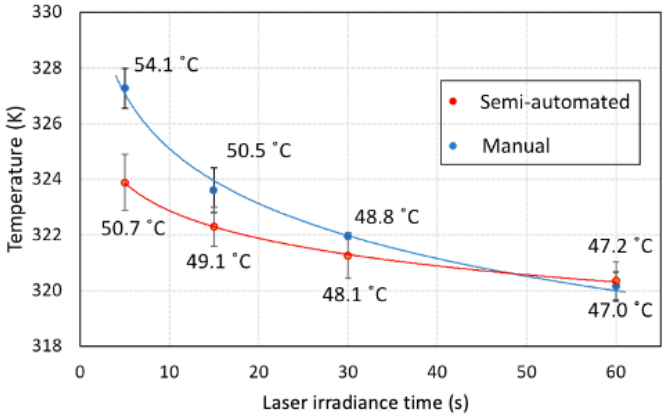

Figure 2.6 Heat damage threshold determined by cell death of keratinocytes. Cell death was observed 2 h after laser irradiation. The heat gradation was generated by a Gaussian-profiled NIR laser beam. Cell death was observed under a fluorescent microscope with double staining of hoechst33342 and propidium iodide. Image analysis was performed with both a semi-automated and a manual method.

2.9 Challenges of laser adjuvant

Various benefits of LLLT have been reported for decades; however, the mechanism of the laser adjuvant is not yet fully understood. Therefore, it is essential to determine the best irradiation conditions, including wavelength, single- or multispectral, irradiance and exposure duration. For instance, a CW laser has an adjuvant effect in animal models, whereas a 10-kHz PW laser does not, indicating that CW and PW light may result in different molecular reactions, even if the total energy is the same.[39]

Not only intracellular molecular reactions but also the dynamics of cellular levels have not been sufficiently revealed; this is due to a lack of necessary materials to track immune cells, including APCs, with no toxicity or tissue interaction. In order to understand the kinetics of laser adjuvants, a new modality is required to observe the biodistribution of vaccines and APCs. Discovering NIR photoreceptors associated with photobiomodulation is also a big challenge.

2.10 Near infrared fluorophores

Fluorescence is one of the categories of luminous phenomena emitted by fluorescent molecules. In particular, it refers to the emissions produced by the irradiation of high-energy, short-wavelength light as an excitation source. The shift of the wavelength from higher energy to lower energy is called the Stokes shift. Since a longer wavelength with lower energy than the excitation light is emitted as fluorescence, only the fluorescent molecules can be imaged by using filters that distinguish the excitation light from the emission light. Fluorescence imaging technology is expected to have a wide range of applications, from differentiation and development in basic biology to drug discovery, cancer diagnosis and treatment in medicine, and thus fluorescence imaging research and development are rapidly progressing.[133–137]

A countless number of fluorophores, from the UV to the NIR range, have been invented. Especially, NIR fluorophores are usable and applicable for biological imaging, possessing unique characteristics such as low scattering and high penetration depth in biological tissue, reduced autofluorescence and a high signal-to-noise ratio, and low absorption by melanin.[96–99] NIR fluorophore derivatives are synthesised based on several base structures: cyanine, phthalocyanine, xanthene, benzoheterocycle, porphyrin and squaraine.[138] The physical, chemical and physiological characteristics of NIR fluorophores vary greatly depending on the structure. The following section introduces four conventional NIR fluorophores: indocyanine

green (ICG), methylene blue (MB), cyanine 5 (Cy5) and cyanine 7 (Cy7). ICG, Cy5 and Cy7 are classified in cyanine dye, while MB is classified in phenothiazinium dye.[139,140] In the following sections, the current status of the development of fluorescence imaging technology is briefly introduced. Importantly, a novel fluorophore, zwitterionic fluorophore 800-1C (ZW800-1C), which has a high signal-to-noise ratio, is expected to be applied in clinic. Different properties of other fluorophores, such as ICG, MB, Cy5 and Cy7, are compared.

2.10.1 Indocyanine green, methylene blue, cyanine 5 and 7

ICG and MB are the only two NIR fluorophores that have been approved for humans by the FDA, and both are widely used in medical practice.[138] ICG was initially approved in 1959 for hepatic function diagnostics, and was later expanded for ophthalmology and cardiology in fluorescence-guided surgery.[141] In addition, ICG is the only NIR fluorophore that has excitation and emission wavelengths above 800 nm (Table 2). Recent studies have applied ICG and the fluorescence imaging system for visualising LNs in order to resect metastatic tumour cells in various tissues, including the oesophagus, the stomach, the colon, the bladder, the prostate, the cervix and the ovarium. Not only LNs but also tumours can be imaged intraoperatively. The structure of ICG is shown in Figure 2.7. The base structure is also called heptamethine, since heptane-like C-C bonding occurs in the middle, meaning its fluorescence wavelength is around 800 nm.[142]

MB (Figure 2.8) is another clinically used NIR fluorophore that has shorter excitation and emission wavelengths than ICG: 665 nm and 688 nm, respectively (Table 2). MB and the fluorescence imaging system are approved for LN mapping and several types of cancer imaging. Similar to ICG, MB has been developed for future clinical applications to visualise malignant cancers, such as pancreatic tumours, insulinomas and solitary fibrous tumors.[139,143] These two dyes, ICG and MB, are used for both open and laparoscopic surgeries for the purpose of enhancing visibility for surgeons in human clinical practice.[144,145]

Another fluorophore, approved by the European Medicine Agency (EMA), is 5-aminolevulinic acid (5-ALA), but it is mainly used as a photosensitiser, which is irradiated by a certain laser wavelength and generates ROS. Once the dye is taken into the cytosol, the chemical structure is converted into protoporphyrin-IX (PpIX), which is sensitive to light.[146] Because of this unique characteristic, 5-ALA is applied for PDT, especially for glioblastoma.[147]

Both Cy5 and Cy7 (Figures 2.9 and 2.10) have yet to be used in clinical practice; however, they are broadly used for basic research purposes all over the world. The wavelengths

of Cy5 and Cy7 for excitation are 655 nm and 775 nm, while those for emission are 675 nm and 795 nm, respectively (Table 2). The advantage of these dyes is their brightness.[148] Although their wavelengths are shorter than those for ICG, their high quantum yields indicate a high brightness that can penetrate biological tissue (Table 2). The disadvantage of Cy5 and Cy7 compared with other NIR fluorophores is that they possess a non-selective stickiness against tissue, resulting in difficulty for non-invasive NIR imaging in the long term.[149]

The benefit of these chemicals is their capability to be conjugated. Recent studies have sought to visualise specific organs or tissues, or even only lesion sites, by using NIR fluorophores conjugated with other chemical drugs, proteins, antibodies, hyaluronic acid and engineered nanoparticles.[150–153] Even though these trials are still in the preclinical stage, it is greatly expected that these chemicals will help visualise specific tissue regions with good visibility so that surgeons can recognise them in high resolution.[154]

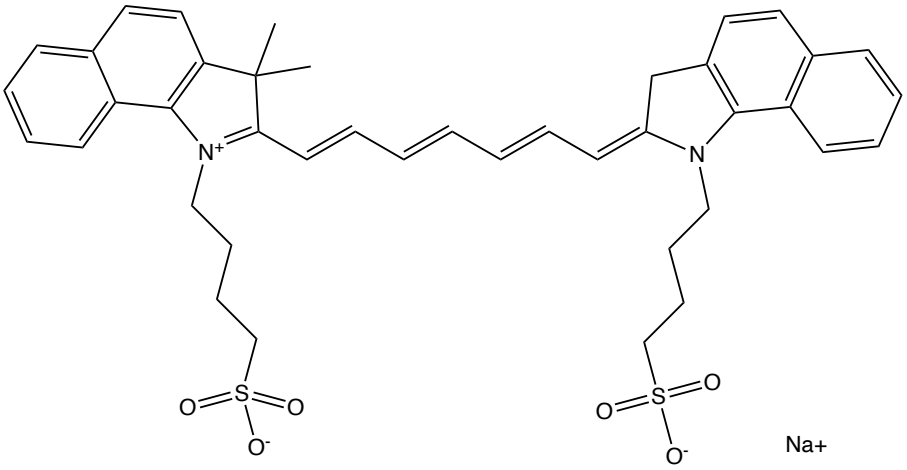

Figure 2.7 Structure of indocyanine green (ICG).

MW: 723.92

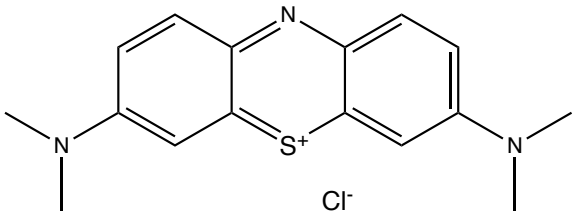

Figure 2.8 Structure of methylene blue (MB).

MW: 284.40

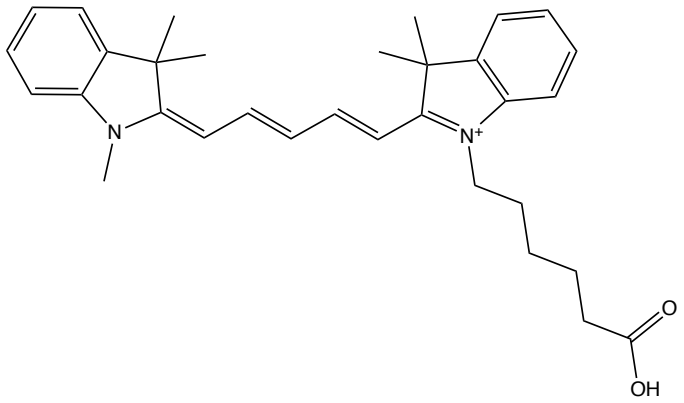

Figure 2.9 Structure of Cyanine 5 (Cy5).

MW: 483.68

This base structure is called pentamethine, since it has a pentane-like C-C bonding structure.

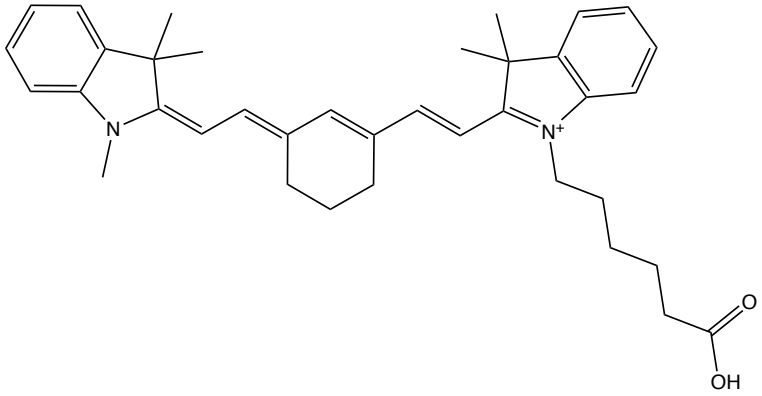

Figure 2.10 Structure of Cyanine 7 (Cy7).

MW: 549.78

Figures 2.7-2.10 are depicted by using ChemDraw version 18.1 (PerkinElmer, US).

Table 2. NIR fluorophores[144,146,149,153,155,156].

The values of quantum yield were acquired in pH 7.0 solvent or fatal bovine serum.

Name	Excitation (nm)	Emission (nm)	Base structure	Quantum Yield (QY, %)	Status
Indocyanine Green (ICG)	807	822	Cyanine	9.3	Clinical
Methylene Blue (MB)	665	688	Phenothiazinium	9.6	Clinical
5-Aminolevulinic acid (5-ALA)	380-440	620	Porphyrin	N/A	Clinical
Cyanine 5 (Cy5)	655	675	Cyanine	30	Pre-clinical
Cyanine 7 (Cy7)	775	795	Cyanine	27	Pre-clinical
ZW700-1C	646	663	Zwitterionic	19.5	Pre-clinical
ZW800-1C	753	772	Zwitterionic	23.9	Pre-clinical

2.10.2 Zwitterionic fluorophore 800-1C

NIR fluorescence has great potential to be used intraoperatively, in what is called image-guided surgery, because of the following four key points. First, NIR light between 650 nm and 900 nm travels deep in skin tissue. Second, the longer the wavelength is, the less light scatters. Third, tissue autofluorescence is lower in NIR light than in visible light. And fourth, NIR light is invisible to surgeons and therefore the surgical field is not affected by NIR fluorophores.[156] As described in the previous section, ICG has been contributing in clinic; however, it has some shortcomings: non-selective attachment to biological tissues, uptake in the liver, which may result in hepatotoxicity, and contamination of the gastrointestinal tract.[157] Even though it has been confirmed that the stickiness of ICG has no severe adverse events, it does lead to a high background fluorescence in NIR images. In order to overcome this issue, we have been developing brand new fluorophores: ZW700-1C (Figure 2.11) and ZW800-1C (Figure 2.12).[156,158] ZW700-1C and ZW800-1C are zwitterionic fluorophores, a fluorescent dye that has a polarity from a positive and negative charge in one molecule, which results in the dye possessing both hydrophobic and hydrophilic characteristics. This in turn results in a long retention time in target tissue, a low background and clearance from the kidneys.[159] This renal clearance reduces hepatotoxicity and ensures the safety of patients. The excitation wavelengths of ZW700-1C and ZW800-1C are 646 nm and 753 nm, and the emission wavelengths are 663 nm and 772 nm, respectively (Table 2). These big Stokes shifts allow us to easily distinguish excitation light from emission light using certain filters. The synthesis method of ZW700-1C and ZW800-1C has already been established at the laboratory scale.[158,160]

Another important value of these molecules is their partial coefficient, LogD, at pH 7.4. LogD is a dimensionless number that indicates the hydrophobicity and migration of a chemical substance. The concentration ratio of each phase or its common logarithm occurs when the substance of interest is in equilibrium in a system where two phases are in contact.[161] The LogD numbers of ICG and ZW800-1C are 7.88 and -2.80, respectively.[157,158] ICG's LogD value indicates high hydrophobicity, which leads to high uptake in the liver, while the small negative value of ZW800-1C indicates its neutrality regarding hydrophobicity and hydrophilicity.

Many applications using ZW800-1C have been proposed. One example is an imaging system of iatrogenic and traumatic ureteral injury models. Ahn *et al*. introduced an imaging modality of urinary catheters.[162] The renal cleanability of ZW800-1C allows for the imaging of kidneys, urinary catheters and bladders. In one experiment, 25 nmol of ZW800-1C were injected intravenously into model mice during a lateral laparotomy. The urinary catheters

showed a bright NIR signal within 5 min, which could help surgeons to investigate occlusion and leakage.

The significance of the applicability of ZW700-1C and ZW800-1C is attributable to the involvement of N-hydroxysuccinimide esters which provides easy and affordable conjugation with the fluorophores and amines.[163] Therefore, for conjugation, N-hydroxysuccinimide esters have been used in various preclinical applications because of good compatibility with proteins.

Toll-like receptor 4 (TLR4) is a protein that expresses in tumour-associated macrophages (TAMs). TAMs are key regulators of the tumour microenvironment and of inflammatory reactions.[164] Ji *et al*. performed real-time NIR imaging of hepatocellular carcinoma using a specific targetability of anti-TLR4 antibodies and TAMs.[165] Anti-TLR4 antibodies were conjugated with ZW800-1C at a conjugation ratio of 1:2.5. The conjugated molecules were injected into mice intravenously in 5% bovine serum albumin (BSA) in saline. The NIR fluorescence signal was observed up to 48 h post injection.

The enhanced permeability and retention (EPR) effect is an essential characteristic of the tumour microenvironment (TME) for drug delivery and therapy.[166] The TME has higher retention than other surrounding tissues lacking the exclusion route, represented by lymphatic vessels. The EPR effect is highly dependent on features of molecules, such as size, polarity and surface property.[167] Kang *et al*. introduced NIR-conjugated polyethylene glycols (PEGs).[168] The molecular size of PEGs can be easily modified by changing the formulation reaction time. Kang *et al*. conjugated ZW800-1C to different-sized PEGs – from 1 kDa to 60 kDa – and investigated the fluorescence retention in cervical cancer cells (HeLa cells) in a nude mouse model. The NIR signal from the tumour was observed at 24 h post injection. 20-kDa PEG-ZW800-1C showed the best tumour-to-background ratio (TBR), with minimal interaction with other tissue.

A nanoparticle drug delivery system using NIR imaging was invented by Kang *et al.*[169] ZW800-1C was conjugated to the terminal amine of cyclodextrin-conjugated poly(ε-lysine) (CDPL) for real-time fluorescence imaging. ZW800-1C-CDPL consists of four domains: backbone poly(ε-lysine), ZW800-1C contrast agent, a cavity for the drug made by beta-cyclodextrin and an anticancer drug. The size of the whole molecule is less than 5.5 nm, which is small enough to permeate from the blood vessels into organs or tissues. For cancer treatment, imatinib, a small molecule anticancer drug that is used to treat chronic myelogenous leukaemia and gastrointestinal stromal tumours (GIST), was loaded on ZW800-1C-CDPL and injected into a GIST mouse model intravenously. The bright signal remained in the tumour for 24 h without being trapped by immune cells, such as macrophages. ZW800-1C-CDPL molecules

that were not taken up by the tumours were excreted by the kidneys within 24 h, ensuring low toxicity. This innovative molecule can be used not only for therapeutic purposes but also for diagnostics. The associated academic field is called theranostics (a portmanteau of *therapy* and *diagnostics*) and has been intensively investigated all over the world.[170]

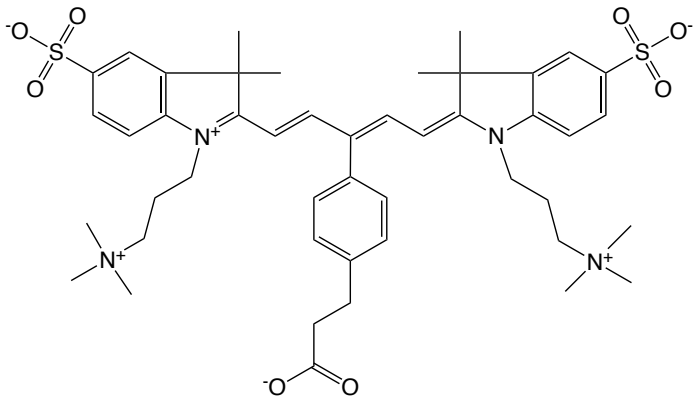

Figure 2.11 Structure of ZW700-1C.

MW: 861.13

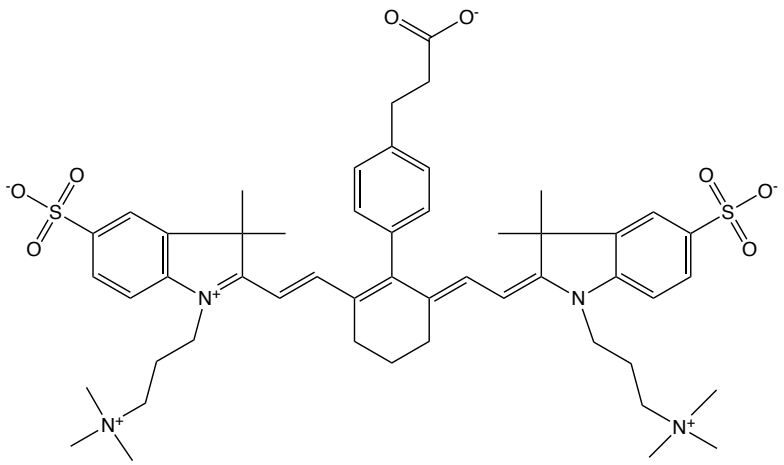

Figure 2.12 Structure of ZW800-1C.

MW: 927.23

Figures 2.11-2.12 are depicted with ChemDraw version 18.1 (PerkinElmer, US).

2.10.3 Near infrared imaging system

Developing a new imaging system is also an important factor for NIR imaging applications. For the purpose of practical use, the imaging system ought to be affordable, small enough to fit in an operation room, and built with an easy user interface. The NIR fluorescence imaging system was initially established for intraoperative open surgery.[171] However, in recent years, laparoscopic surgery has been preferred over open surgery in terms of cost efficiency and clinical effectiveness.[172,173] Hence, it is necessary to establish a new NIR fluorescence imaging modality that can be applied in both open and laparoscopic surgery. Several imaging systems for different purposes are introduced in this section.

SPY Elite, an open-air intraoperative NIR imaging system manufactured by Novadaq, is commercially available and is the most widely used NIR imaging device for visualising ICG intraoperatively.[174–176] The system was approved by the FDA in 2005. As an excitation light source, an 805-nm laser, as well as a CCD sensor for detecting the NIR signal, are used in the system. Additionally, the system features a sufficient field of view (FOV) for operators: 19 × 14 cm^2. For portability, Hamamatsu developed a handheld NIR device called the photo dynamic eye (PDE),[175] which was approved by the FDA in 2012 and later used for sentinel LN mapping with ICG.[175,177] Instead of a laser diode, PDE is equipped with a light-emitting diode so that it can reduce the size and cost of the system. A disadvantage of this system is that it has a 10 × 6.7 cm^2 FOV, which is only one-fourth that of the SPY Elite system. For laparoscopic NIR imaging, Vitom ICG was invented by Karl Storz and approved by the FDA in 2016.[175] Even though only four years have passed since FDA approval, Vitom ICG has already been used in many clinical situations, such as the LN mapping of cancer and in urological surgery, thanks to its minimal invasiveness and clinical benefit.[178–180]

In order to realise a dual imaging modality at 700 nm and 800 nm channels, we have developed our own imaging system called the FLARE system.[181–183] The FLARE system is equipped with 670-nm and 760-nm laser diodes, which enables three-channel imaging simultaneously. Operators can look at one screen and recognise three different colours depicted from 670-nm and 760-nm NIR fluorescence. The latest studies have further developed the FLARE system in order to reduce its size to fit in operation rooms, creating a new system called KFLARE (Figure 2.13). As in the FLARE system, KFLARE utilises two wavelengths of NIR lasers, 660 nm and 760 nm. The lasers are coupled with multimode fibres and connected to a holder that surrounds a CCD camera. The camera system has a prism that divides three

channels: visible light, 660-nm fluorescence and 760-nm fluorescence. To ensure that surgeons can see the surgical field directly, ambient white light can be illuminated from the system.

One shortcoming of NIR intraoperative imaging is the permeability of NIR light. The penetration depth of NIR light is limited to 1 cm. To overcome this limitation, a multimodal system should be developed that combines NIR imaging with other clinical imaging applications, such as ultrasound, positron emission tomography (PET) and computer tomography (CT).[184] Such a device could increase the accuracy of the system and dramatically improve clinical outcomes.

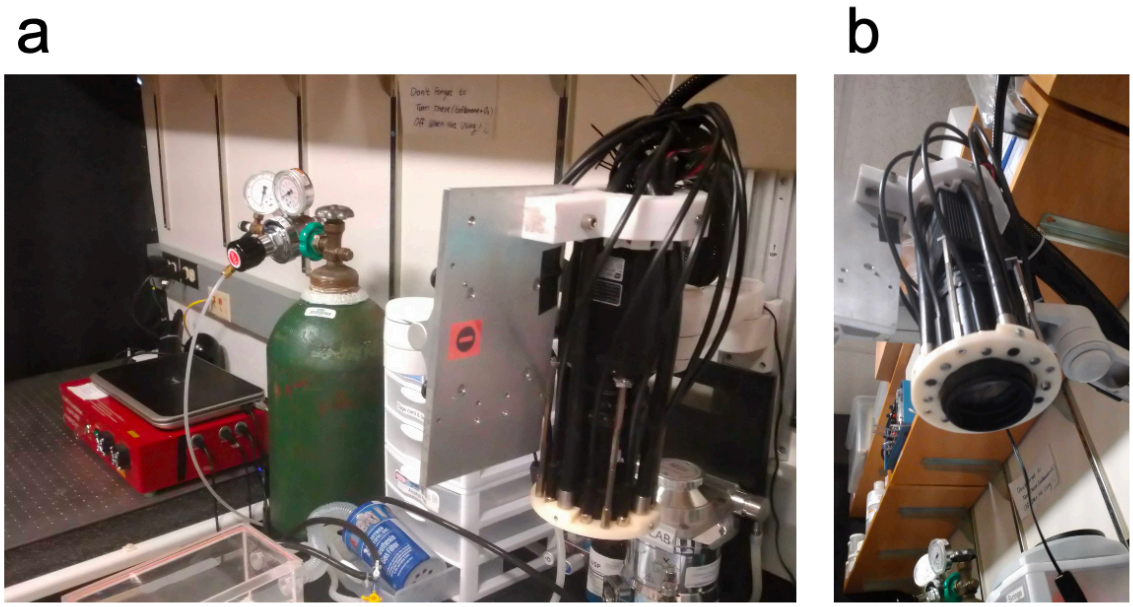

Figure 2.13 KFLARE system.
(a) Laser box (red) and imaging head. (b) Imaging head equipped with multiple optic fibres of 660-nm and 760-nm irradiance.

References

1. Karger, S. Human Immunoglobulins. *Transfus. Med. Hemotherapy* **36**, 449–459 (2009).
2. Hamilton, R. G. Human IgG subclass measurements in the clinical laboratory. *Clin. Chem.* **33**, 1707–1725 (1987).
3. Renegar, K. B., Small, P. A., Boykins, L. G. & Wright, P. F. Role of IgA versus IgG in the Control of Influenza Viral Infection in the Murine Respiratory Tract. *J. Immunol.* **173**, 1978–1986 (2004).
4. Pontisso, P. *et al.* The preS1 domain of hepatitis B virus and IgA cross-react in their binding to the hepatocyte surface. *J. Gen. Virol.* **73**, 2041–2045 (1992).
5. Mukkur, T. K. S. & Froese, A. Isolation and characterization of IgM from bovine colostral whey. *Immunochemistry* **8**, 257–264 (1971).
6. Echeverría de Carlos, A. *et al.* Concentrations of Pneumococcal IgA and IgM are compromised in some individuals with antibody deficiencies. *J. Immunoass. Immunochem.* **38**, 505–513 (2017).
7. INGANÄS, M. Comparison of Mechanisms of Interaction between Protein A from Staphylococcus aureus and Human Monoclonal IgG, IgA and IgM in Relation to the Classical Fcγ and the Alternative F(ab')2γ Protein A Interactions. *Scand. J. Immunol.* **13**, 343–352 (1981).
8. Pollack, M., Koles, N. L., Preston, M. J., Brown, B. J. & Pier, G. B. Functional properties of isotype-switched immunoglobulin M (IgM) and IgG monoclonal antibodies to Pseudomonas aeruginosa lipopolysaccharide. *Infect. Immun.* **63**, 4481–4488 (1995).
9. Saxen, H. Mechanism of the protective action of anti-Salmonella IgM in experimental mouse salmonellosis. *J. Gen. Microbiol.* **130**, 2277–2283 (1984).
10. Rowe, D. S. & Fahey, J. L. A NEW CLASS OF HUMAN IMMUNOGLOBULINS. *J. Exp. Med.* **121**, 171–199 (1965).
11. Chen, K. *et al.* Immunoglobulin D enhances immune surveillance by activating antimicrobial, proinflammatory and B cell-stimulating programs in basophils. *Nat. Immunol.* **10**, 889–898 (2009).
12. Kinet, J.-P. THE HIGH-AFFINITY I g E RECEPTOR (FcεRI): From Physiology to Pathology . *Annu. Rev. Immunol.* **17**, 931–972 (1999).
13. Saphire, E. O. *et al.* Crystal structure of a neutralizing human IgG against HIV-1: A template for vaccine design. *Science (80-.).* **293**, 1155–1159 (2001).
14. Kambayashi, T. & Laufer, T. M. Atypical MHC class II-expressing antigen-presenting cells: Can anything replace a dendritic cell? *Nat. Rev. Immunol.* **14**, 719–730 (2014).
15. Mathers, A. R. & Larregina, A. T. Professional antigen-presenting cells of the skin. *Immunol. Res.* **36**, 127–136 (2006).
16. Lodish, H. *et al.* Chapter 23: Immunology. in *Molecular Cellular Biology* 1059–1114 (2013).
17. Allan, R. S. *et al.* Migratory Dendritic Cells Transfer Antigen to a Lymph Node-Resident Dendritic Cell Population for Efficient CTL Priming. *Immunity* **25**, 153–162 (2006).
18. Ulrike Haessler, Marco Pisano, Mingming Wu & Swartz, M. A. Dendritic cell chemotaxis in 3D under defined chemokine gradients reveals differential response to ligands CCL21 and CCL19. *Proc. Natl. Acad. Sci. U. S. A.* **108**, 5614–5619 (2011).

19. Hughes, C. E., Benson, R. A., Bedaj, M. & Maffia, P. Antigen-presenting cells and antigen presentation in tertiary lymphoid organs. *Front. Immunol.* **7**, (2016).
20. Itano, A. A. & Jenkins, M. K. Antigen presentation to naive CD4 T cells in the lymph node. *Nat. Immunol.* **4**, 733–739 (2003).
21. Smallpox. *U.S. Food and Drug Administration* (2018).
22. Piot, P. *et al.* Immunization: vital progress, unfinished agenda. *Nature* **575**, 119–129 (2019).
23. Diphtheria. *Center for Disease Control and Prevension* (2019).
24. Morbidity and Mortality Weekly Report (MMWR), volume 66. *Centers for Disease Control and Prevention* (2017).
25. Arakane, R. *et al.* Superior immunogenicity profile of the new intradermal influenza vaccine compared to the standard subcutaneous vaccine in subjects 65 years and older: A randomized controlled phase III study. *Vaccine* **33**, 6650–6658 (2015).
26. Arakane, R. *et al.* Immunogenicity and safety of the new intradermal influenza vaccine in adults and elderly: A randomized phase 1/2 clinical trial. *Vaccine* **33**, 6340–6350 (2015).
27. Cox, J. C. & Coulter, A. R. Adjuvants - A classification and review of their modes of action. *Vaccine* **15**, 248–256 (1997).
28. Kashiwagi, S., Brauns, T., Gelfand, J. & Poznansky, M. C. Laser vaccine adjuvants: History, progress, and potential. *Hum. Vaccines Immunother.* **10**, 1892–1907 (2014).
29. 2009 H1N1 Pandemic (H1N1pdm09 virus). *Centers for Disease Control and Prevention* (2019).
30. Miller, E. *et al.* Risk of narcolepsy in children and young people receiving AS03 adjuvanted pandemic A/H1N1 2009 influenza vaccine: Retrospective analysis. *BMJ* **346**, 1–11 (2013).
31. Partinen, M. *et al.* Increased incidence and clinical picture of childhood narcolepsy following the 2009 H1N1 pandemic vaccination campaign in Finland. *PLoS One* **7**, 1–9 (2012).
32. Colafrancesco, S., Perricone, C., Tomljenovic, L. & Shoenfeld, Y. Human Papilloma Virus Vaccine and Primary Ovarian Failure: Another Facet of the Autoimmune/Inflammatory Syndrome Induced by Adjuvants. *Am. J. Reprod. Immunol.* **70**, 309–316 (2013).
33. Morimoto, A. *et al.* Effect on HPV vaccination in Japan resulting from news report of adverse events and suspension of governmental recommendation for HPV vaccination. *Int. J. Clin. Oncol.* **20**, 549–555 (2015).
34. Batista-Duharte, A., Lindblad, E. B. & Oviedo-Orta, E. Progress in understanding adjuvant immunotoxicity mechanisms. *Toxicol. Lett.* **203**, 97–105 (2011).
35. Wilkins, A. L. *et al.* AS03- and MF59-adjuvanted influenza vaccines in children. *Front. Immunol.* **8**, (2017).
36. Kool, M., Fierens, K. & Lambrecht, B. N. Alum adjuvant: Some of the tricks of the oldest adjuvant. *J. Med. Microbiol.* **61**, 927–934 (2012).
37. Novicki, D. L. Chapter 8 - Introduction to Vaccines and Adjuvants. in *Nonclinical Development of Novel Biologics, Biosimilars, Vaccines and Specialty Biologics* 213–224 (2013).
38. Hyer, R. N. & Janssen, R. S. Immunogenicity and safety of a 2-dose hepatitis B vaccine, HBsAg/CpG 1018, in persons with diabetes mellitus aged 60–70 years. *Vaccine* **37**, 5854–5861 (2019).
39. Kashiwagi, S. *et al.* Near-infrared laser adjuvant for influenza vaccine. *PLoS One* **8**, (2013).

40. Kashiwagi, S., Brauns, T. & Poznansky, M. C. Classification of Laser Vaccine Adjuvants. *J. Vaccines* **7**, 1–11 (2016).
41. Kimizuka, Y. *et al.* Semiconductor diode laser device adjuvanting intradermal vaccine. *Vaccine* **35**, 2404–2412 (2017).
42. Kimizuka, Y. *et al.* Brief Exposure of Skin to Near-Infrared Laser Modulates Mast Cell Function and Augments the Immune Response. *J. Immunol.* ji1701687 (2018) doi:10.4049/jimmunol.1701687.
43. Morse, K. *et al.* Near-Infrared 1064 nm Laser Modulates Migratory Dendritic Cells To Augment the Immune Response to Intradermal Influenza Vaccine. *J. Immunol.* ji1601873 (2017) doi:10.4049/jimmunol.1601873.
44. Huang, Y. Y., Chen, A. C. H., Carroll, J. D. & Hamblin, M. R. Biphasic dose response in low level lightherapy. *Dose-Response* **7**, 358–383 (2009).
45. Hamblin, M. R., Huang, Y. Y., Sharma, S. K. & Carroll, J. Biphasic dose response in low level light therapy - an update. *Dose-Response* **9**, 602–618 (2011).
46. Karu, T. I. Mitochondrial signaling in mammalian cells activated by red and near-IR radiation. *Photochem. Photobiol.* **84**, 1091–1099 (2008).
47. Xu, Z. *et al.* Low-Level Laser Irradiation Improves Depression-Like Behaviors in Mice. *Mol. Neurobiol.* **54**, 4551–4559 (2017).
48. Chen, A. C. H. *et al.* Low-Level laser therapy activates NF-kB via generation of reactive oxygen species in mouse embryonic fibroblasts. *PLoS One* **6**, 1–8 (2011).
49. Lodish, H. *et al.* Chapter 12: Cellular Energetics. in *Molecular and Cellular Biology* 517–576 (2013).
50. Corbet, C. & Feron, O. Cancer cell metabolism and mitochondria: Nutrient plasticity for TCA cycle fueling. *Biochim. Biophys. Acta - Rev. Cancer* **1868**, 7–15 (2017).
51. Da Cunha, F. M., Torelli, N. Q. & Kowaltowski, A. J. Mitochondrial Retrograde Signaling: Triggers, Pathways, and Outcomes. *Oxid. Med. Cell. Longev.* **2015**, (2015).
52. Hamblin, M. R., Huang, Y. Y., Sharma, S. K. & Carroll, J. Biphasic dose response in low level light therapy - an update. *Dose-Response* **9**, 602–618 (2011).
53. Zorov, D. B., Juhaszova, M. & Sollott, S. J. Mitochondrial ROS-induced ROS release: An update and review. *Biochim. Biophys. Acta - Bioenerg.* **1757**, 509–517 (2006).
54. Zorov, D. B., Juhaszova, M. & Sollott, S. J. Mitochondrial reactive oxygen species (ROS) and ROS-induced ROS release. *Physiol. Rev.* **94**, 909–950 (2014).
55. Hamblin, M. R. Mechanisms and applications of the anti-inflammatory effects of photobiomodulation. *AIMS Biophys.* **4**, 337–361 (2017).
56. Martínez-Reyes, I. & Chandel, N. S. Mitochondrial TCA cycle metabolites control physiology and disease. *Nat. Commun.* **11**, 102 (2020).
57. Buck, M. D., O'Sullivan, D. & Pearce, E. L. T cell metabolism drives immunity. *J. Exp. Med.* **212**, 1345–1360 (2015).
58. Dakubo, G. D. Mitochondrial reactive oxygen species and cancer. *Handb. Free Radicals Form. Types Eff.* 99–116 (2010) doi:10.1186/2049-3002-2-17.
59. Chamoto, K. *et al.* Mitochondrial activation chemicals synergize with surface receptor PD-1 blockade for T cell-dependent antitumor activity. *Proc. Natl. Acad. Sci.* **114**, E761–E770 (2017).

60. Carr, H. S. & Winge, D. R. Assembly of cytochrome c oxidase within the mitochondrion. *Acc. Chem. Res.* **36**, 309–316 (2003).
61. Sergin, I. & Razani, B. Self-eating in the plaque: What macrophage autophagy reveals about atherosclerosis. *Trends Endocrinol. Metab.* **25**, 225–234 (2014).
62. Tormos, K. V. *et al.* Mitochondrial complex III ROS regulate adipocyte differentiation. *Cell Metab.* **14**, 537–544 (2011).
63. Lee, I., Bender, E. & Kadenbach, B. Control of mitochondrial membrane potential and ROS formation by reversible phosphorylation of cytochrome c oxidase. *Mol. Cell. Biochem.* **234**–**235**, 63–70 (2002).
64. Mailloux, R. J. Teaching the fundamentals of electron transfer reactions in mitochondria and the production and detection of reactive oxygen species. *Redox Biol.* **4**, 381–398 (2015).
65. Bauer, G. Targeting extracellular ROS signaling of tumor cells. *Anticancer Res.* **34**, 1467–1482 (2014).
66. Görlach, A., Bertram, K., Hudecova, S. & Krizanova, O. Calcium and ROS: A mutual interplay. *Redox Biol.* **6**, 260–271 (2015).
67. Trebak, M. & Kinet, J. P. Calcium signalling in T cells. *Nat. Rev. Immunol.* **19**, 154–169 (2019).
68. Marchi, S. *et al.* Mitochondria-Ros Crosstalk in the Control of Cell Death and Aging. *J. Signal Transduct.* **2012**, 1–17 (2012).
69. Tang, D.-W. *et al.* The Disturbances of Endoplasmic Reticulum Calcium Homeostasis Caused by Increased Intracellular Reactive Oxygen Species Contributes to Fragmentation in Aged Porcine Oocytes1. *Biol. Reprod.* **89**, 1–9 (2013).
70. Eckert, A. *et al.* Mitochondrial dysfunction, apoptotic cell death, and Alzheimer's disease. *Biochem. Pharmacol.* **66**, 1627–1634 (2003).
71. Abou-Sleiman, P. M., Muqit, M. M. K. & Wood, N. W. Expanding insights of mitochondrial dysfunction in Parkinson's disease. *Nat. Rev. Neurosci.* **7**, 207–219 (2006).
72. Oliveira, C. F. H. *et al.* Oxidative stress in atherosclerosis-prone mouse is due to low antioxidant capacity of mitochondria. *FASEB J.* **19**, 1–14 (2005).
73. Kizhakekuttu, T. J. & Widlansky, M. E. Natural antioxidants and hypertension: Promise and challenges. *Cardiovasc. Ther.* **28**, 20–32 (2010).
74. Fulda, S., Galluzzi, L. & Kroemer, G. Targeting mitochondria for cancer therapy. *Nat. Rev. Drug Discov.* **9**, 447–464 (2010).
75. Kembro, J. M., Cortassa, S. & Aon, M. A. Mitochondrial reactive oxygen species and arrhythmias. *Syst. Biol. Free Radicals Antioxidants* 1047–1076 (2012) doi:10.1007/978-3-642-30018-9_69.
76. Oh, H. & Kim, J. Clinical Application of CO2 Laser. in *CO2 Laser - Optimisation and Application* 357–378 (2012).
77. Salem, U. *et al.* Neurosurgical applications of MRI guided laser interstitial thermal therapy (LITT). *Cancer Imaging* **19**, 1–13 (2019).
78. Jacobson, B. & Murray, A. *Medical Devices*. *Medical Devices* (Churchill Livingstone, 2007).
79. Einstein, A. & Masters, B. R. Albert Einstein and the Nature of Light. *OPN Opt. Photonics News* **23**, 42–47 (2012).
80. Parker, S. Introduction, history of lasers and laser light production. *Br. Dent. J.* **202**, 21–31 (2007).
81. Hecht, J. A short history of laser development Short history of laser development of Photo-Optical

Instrumentation. *Opt. Eng.* **49**, 99–122 (2010).

82. Mussttaf, R. Assessing the impact of low level laser therapy (LLLT) on biological systems: a review. *Int. J. Radiat. Biol.* **30**, 1145–1154 (2019).
83. Liljemalm, R., Nyberg, T. & Von Holst, H. Heating during infrared neural stimulation. *Lasers Surg. Med.* **45**, 469–481 (2013).
84. Xia, Q. & Nyberg, T. Inhibition of cortical neural networks using infrared laser. *J. Biophotonics* 1–12 (2019) doi:10.1002/jbio.201800403.
85. E.J.G.J. Dolmans, D., Fukumura, D. & K.Jain, R. Cancer revoked: Oncogenes as therapeutic targets. *Nat. Rev. Cancer* **3**, 380–387 (2003).
86. McDonagh, A. F. Phototherapy: From ancient egypt to the new millennium. *J. Perinatol.* **21**, S7–S12 (2001).
87. Martin, K. Modernism and the medicalization of sunlight: D. H. Lawrence, Katherine Mansfield, and the sun cure. *Mod. - Mod.* **23**, 423–441 (2016).
88. Gorman, S., Black, L. J., Feelisch, M., Hart, P. H. & Weller, R. Can skin exposure to sunlight prevent liver inflammation? *Nutrients* **7**, 3219–3239 (2015).
89. J., Michael, C., John W., R. & Charles M., C. Conlan,M.J.1996.Biostimulation of wound healing by low-energy laser irradiation A review.pdf. *J. Clin. Periodontol.* **23**, 492–496 (1996).
90. Posten, W. *et al.* Low-level laser therapy for wound healing: Mechanism and efficacy. *Dermatologic Surg.* **31**, 334–340 (2005).
91. Aimbire, F. *et al.* Low-level laser therapy induces dose-dependent reduction of TNFα levels in acute inflammation. *Photomed. Laser Surg.* **24**, 33–37 (2006).
92. Usumez, A. *et al.* Effects of laser irradiation at different wavelengths (660, 810, 980, and 1,064 nm) on mucositis in an animal model of wound healing. *Lasers Med. Sci.* **29**, 1807–1813 (2014).
93. Bjordal, J. M., Johnson, M. I., Iversen, V., Aimbire, F. & Lopes-Martins, R. A. B. Photoradiation in acute pain: A systematic review of possible mechanisms of action and clinical effects in randomized placebo-controlled trials. *Photomed. Laser Surg.* **24**, 158–168 (2006).
94. Chow, R. T., Johnson, M. I., Lopes-Martins, R. A. & Bjordal, J. M. Efficacy of low-level laser therapy in the management of neck pain: a systematic review and meta-analysis of randomised placebo or active-treatment controlled trials. *Lancet* **374**, 1897–1908 (2009).
95. Brosseau, L. *et al.* Low level laser therapy (Classes I, II and III) for treating rheumatoid arthritis. *Cochrane Database Syst. Rev.* (2005) doi:10.1002/14651858.cd002049.pub2.
96. Owens, E. A., Henary, M., El Fakhri, G. & Choi, H. S. Tissue-Specific Near-Infrared Fluorescence Imaging. *Acc. Chem. Res.* **49**, 1731–1740 (2016).
97. Hu, S. *et al.* Real-Time Imaging of Brain Tumor for Image-Guided Surgery. *Adv. Healthc. Mater.* **7**, 1–15 (2018).
98. Frangioni, J. V. In vivo near-infrared fluorescence imaging. *Curr. Opin. Chem. Biol.* **7**, 626–634 (2003).
99. Lee, J. H., Park, G., Hong, G. H., Choi, J. & Choi, H. S. Design considerations for targeted optical contrast agents. *Quant. Imaging Med. Surg.* **2**, 266–26673 (2012).
100. Khan, I., Tang, E. & Arany, P. Molecular pathway of near-infrared laser phototoxicity involves ATF-4 orchestrated ER stress. *Sci. Rep.* **5**, 1–14 (2015).

101. Karu, T. Is it time to consider photobiomodulation as a drug equivalent? *Photomed. Laser Surg.* **31**, 189–191 (2013).
102. Karu, T. Mitochondrial mechanisms of photobiomodulation in context of new data about multiple roles of ATP. *Photomed. Laser Surg.* **28**, 159–160 (2010).
103. Bohovych, I. & Khalimonchuk, O. Sending out an SOS: Mitochondria as a signaling hub. *Front. Cell Dev. Biol.* **4**, 1–15 (2016).
104. Chandel, N. S. Evolution of Mitochondria as Signaling Organelles. *Cell Metab.* **22**, 204–206 (2015).
105. Karu, T. I. & Kolyakov, S. F. Exact action spectra for cellular responses relevant to phototherapy. *Photomed. Laser Surg.* **23**, 355–361 (2005).
106. Karu, T. Primary and secondary mechanisms of action of visible to near-IR radiation on cells. *J. Photochem. Photobiol. B Biol.* **49**, 1–17 (1999).
107. Evans, D. H. & Abrahamse, H. A review of laboratory-based methods to investigate second messengers in low-level laser therapy (LLLT). *Med. Laser Appl.* **24**, 201–215 (2009).
108. Wang, X., Tian, F., Soni, S. S., Gonzalez-Lima, F. & Liu, H. Interplay between up-regulation of cytochrome-c-oxidase and hemoglobin oxygenation induced by near-infrared laser. *Sci. Rep.* **6**, 1–10 (2016).
109. Sanderson, T. H. *et al.* Inhibitory modulation of cytochrome c oxidase activity with specific near-infrared light wavelengths attenuates brain ischemia/reperfusion injury. *Sci. Rep.* **8**, 1–12 (2018).
110. Sharma, S. K. *et al.* Dose response effects of 810nm laser light on mouse primary cortical neurons. *Lasers Surg. Med.* **43**, 851–859 (2011).
111. Amaroli, A., Ferrando, S. & Benedicenti, S. Photobiomodulation Affects Key Cellular Pathways of all Life-Forms: Considerations on Old and New Laser Light Targets and the Calcium Issue. *Photochem. Photobiol.* **95**, 455–459 (2019).
112. Huang, Y. Y., Nagata, K., Tedford, C. E. & Hamblin, M. R. Low-level laser therapy (810 nm) protects primary cortical neurons against excitotoxicity in vitro. *J. Biophotonics* **7**, 656–664 (2014).
113. Breitbart, H., Levinshal, T., Cohen, N., Friedmann, H. & Lubart, R. Changes in calcium transport in mammalian sperm mitochondria and plasma membrane irradiated at 633 nm (HeNe laser). *J. Photochem. Photobiol. B Biol.* **34**, 117–121 (1996).
114. Wang, L., Zhang, D. & Schwarz, W. TRPV Channels in Mast Cells as a Target for Low-Level-Laser Therapy. *Cells* **3**, 662–673 (2014).
115. Hamblin, M. R. Shining light on the head: Photobiomodulation for brain disorders. *BBA Clin.* **6**, 113–124 (2016).
116. Wang, Y., Huang, Y. Y., Wang, Y., Lyu, P. & Hamblin, M. R. Red (660 nm) or near-infrared (810 nm) photobiomodulation stimulates, while blue (415 nm), green (540 nm) light inhibits proliferation in human adipose-derived stem cells. *Sci. Rep.* **7**, 1–10 (2017).
117. Fernandes, K. P. S. *et al.* Photobiomodulation with 660-nm and 780-nm laser on activated J774 macrophage-like cells: Effect on M1 inflammatory markers. *J. Photochem. Photobiol. B Biol.* **153**, 344–351 (2015).
118. Chen, A. C.-H., Huang, Y.-Y., Sharma, S. K. & Hamblin, M. R. Can dendritic cells see light? *Biophotonics Immune Responses V* **7565**, 756504 (2010).

119. Agaiby, A., Ghali, L. & Dyson, M. Laser Modulation of T-Lymphocyte Proliferation in Vitro. *Laser Therapy* vol. 10 153–158 (1998).
120. Kamiński, M. M. *et al.* T cell Activation Is Driven by an ADP-Dependent Glucokinase Linking Enhanced Glycolysis with Mitochondrial Reactive Oxygen Species Generation. *Cell Rep.* **2**, 1300–1315 (2012).
121. Sena, L. A. *et al.* Mitochondria Are Required for Antigen-Specific T Cell Activation through Reactive Oxygen Species Signaling. *Immunity* **38**, 225–236 (2013).
122. Gnanaprakasam, J. N. R., Wu, R. & Wang, R. Metabolic reprogramming in modulating T cell reactive oxygen species generation and antioxidant capacity. *Front. Immunol.* **9**, (2018).
123. Devadas, S., Zaritskaya, L., Rhee, S. G., Oberley, L. & Williams, M. S. Discrete generation of superoxide and hydrogen peroxide by T cell receptor stimulation: Selective regulation of mitogen-activated protein kinase activation and Fas ligand expression. *J. Exp. Med.* **195**, 59–70 (2002).
124. Lee, D. H. *et al.* Glutathione peroxidase 1 deficiency attenuates concanavalin a-induced hepatic injury by modulation of t-cell activation. *Cell Death Dis.* **7**, 1–10 (2016).
125. Feske, S., Wulff, H. & Skolnik, E. Y. *Ion Channels in Innate and Adaptive Immunity*. *Annual Review of Immunology* vol. 33 (2015).
126. Wang, H. *et al.* Low-Voltage-Activated CaV3.1 Calcium Channels Shape T Helper Cell Cytokine Profiles. *Immunity* **44**, 782–794 (2016).
127. De Stefani, D., Rizzuto, R. & Pozzan, T. Enjoy the Trip: Calcium in Mitochondria Back and Forth. *Annu. Rev. Biochem.* **85**, 161–192 (2016).
128. Parker, I. & Smith, I. F. Recording single-channel activity of inositol trisphosphate receptors in intact cells with a microscope, not a patch clamp. *J. Gen. Physiol.* **136**, 119–127 (2010).
129. Yarosz, E. L. & Chang, C. H. Role of reactive oxygen species in regulating T cell-mediated immunity and disease. *Immune Netw.* **18**, 1–15 (2018).
130. Chen, X. *et al.* A novel laser vaccine adjuvant increases the motility of antigen presenting cells. *PLoS One* **5**, (2010).
131. Winn, B. Y. H. J., Baldamus, C. A., Jooste, S. V & Russels, P. S. Acute destruction by humoral antibody of rat skin grafted to mice: the role of complement and polymorphonuclear leukocytes. *J. Exp. Med.* **137**, 893–910 (1973).
132. Katagiri, W. Evaluation of skin cell heat damage for the safe usage of laser medical devices. *Master thesis Sch. Eng. Sci. Chem. Biotechnol. Heal. KTH, R. Inst. Technol. Stock. Sweden* (2018).
133. Alander, J. T. *et al.* A Review of indocyanine green fluorescent imaging in surgery. *Int. J. Biomed. Imaging* **2012**, (2012).
134. Ntziachristos, V. Fluorescence Molecular Imaging. *Annu. Rev. Biomed. Eng.* **8**, 1–33 (2006).
135. Rudin, M. & Weissleder, R. Molecular imaging in drug discovery and development. *Nat. Rev. Drug Discov.* **2**, 123–131 (2003).
136. Pajerowski, J. D., Dahl, K. N., Zhong, F. L., Sammak, P. J. & Discher, D. E. Physical plasticity of the nucleus in stem cell differentiation. *Proc. Natl. Acad. Sci. U. S. A.* **104**, 15619–15624 (2007).
137. Park, G. K. *et al.* Rapid and Selective Targeting of Heterogeneous Pancreatic Neuroendocrine Tumors. *ISCIENCE* **23**, 101006 (2020).

138. Gibbs, S. L. Near infrared fluorescence for image-guided surgery. *Quant. Imaging Med. Surg.* **2**, 177–17787 (2012).
139. Nagaya, T., Nakamura, Y. A., Choyke, P. L. & Kobayashi, H. Fluorescence-guided surgery. *Front. Oncol.* **7**, (2017).
140. Yaroslavsky, A. N., Feng, X., Muzikansky, A. & Hamblin, M. R. Fluorescence Polarization of Methylene Blue as a Quantitative Marker of Breast Cancer at the Cellular Level. *Sci. Rep.* **9**, 1–10 (2019).
141. Zhou, J., Yang, F., Jiang, G. & Wang, J. Applications of indocyanine green based near-infrared fluorescence imaging in thoracic surgery. *J. Thorac. Dis.* **8**, S738–S743 (2016).
142. Hyun, H. *et al.* Structure-inherent targeting of near-infrared fluorophores for parathyroid and thyroid gland imaging. *Nat. Med.* **21**, 192–197 (2015).
143. van der Vorst, J. R. Near-infrared fluorescence imaging of a solitary fibrous tumor of the pancreas using methylene blue. *World J. Gastrointest. Surg.* **4**, 180 (2012).
144. Slooter, M. D., Janssen, A., Bemelman, W. A., Tanis, P. J. & Hompes, R. Currently available and experimental dyes for intraoperative near-infrared fluorescence imaging of the ureters: a systematic review. *Tech. Coloproctol.* **23**, 305–313 (2019).
145. Matsui, A. *et al.* Real-time, near-infrared, fluorescence-guided identification of the ureters using methylene blue. *Surgery* **148**, 78–86 (2010).
146. Karu, T. I., Kryukov, P. G., Letokhov, V. S., Matveetz, Y. A. & Semchishen, V. A. High quantum yield of photochemical reactions of protoporphyrin-IX induced by powerful ultrashort laser pulses. *Appl. Phys.* **24**, 245–247 (1981).
147. Montcel, B., Mahieu-Williame, L., Armoiry, X., Meyronet, D. & Guyotat, J. Two-peaked 5-ALA-induced PpIX fluorescence emission spectrum distinguishes glioblastomas from low grade gliomas and infiltrative component of glioblastomas. *Biomed. Opt. Express* **4**, 548 (2013).
148. Berlier, J. E. *et al.* Quantitative Comparison of Long-wavelength Alexa Fluor Dyes to Cy Dyes: Fluorescence of the Dyes and Their Bioconjugates. *J. Histochem. Cytochem.* **51**, 1699–1712 (2003).
149. Katagiri, W. *et al.* Real-Time Imaging of Vaccine Biodistribution Using Zwitterionic NIR Nanoparticles. *Adv. Healthc. Mater.* **8**, e1900035 (2019).
150. Hill, T. K. *et al.* Near infrared fluorescent nanoparticles derived from hyaluronic acid improve tumor contrast for image-guided surgery. *Theranostics* **6**, 2314–2328 (2016).
151. Ogawa, M., Kosaka, N., Choyke, P. L. & Kobayashi, H. In vivo molecular imaging of cancer with a quenching near-infrared fluorescent probe using conjugates of monoclonal antibodies and indocyanine green. *Cancer Res.* **69**, 1268–1272 (2009).
152. Mérian, J., Gravier, J., Navarro, F. & Texier, I. Fluorescent nanoprobes dedicated to in vivo imaging: From preclinical validations to clinical translation. *Molecules* **17**, 5564–5591 (2012).
153. Owens, E. A., Lee, S., Choi, J., Henary, M. & Choi, H. S. NIR fluorescent small molecules for intraoperative imaging. *Wiley Interdiscip. Rev. Nanomedicine Nanobiotechnology* **7**, 828–838 (2015).
154. Haque, A., Faizi, M. S. H., Rather, J. A. & Khan, M. S. Next generation NIR fluorophores for tumor imaging and fluorescence-guided surgery: A review. *Bioorganic Med. Chem.* **25**, 2017–2034 (2017).
155. te Velde, E. A., Veerman, T., Subramaniam, V. & Ruers, T. The use of fluorescent dyes and probes in

surgical oncology. *Eur. J. Surg. Oncol.* **36**, 6–15 (2010).

156. Hyun, H. *et al.* 700-nm Zwitterionic Near-Infrared Fluorophores for Dual-Channel Image-Guided Surgery. *Mol. Imaging Biol.* **18**, 52–61 (2016).
157. Choi, H. S. *et al.* Synthesis and in vivo fate of zwitterionic near-infrared fluorophores. *Angew. Chemie - Int. Ed.* **50**, 6258–6263 (2011).
158. Hyun, H. *et al.* Central C-C bonding increases optical and chemical stability of NIR fluorophores. *RSC Adv.* **4**, 58762–58768 (2014).
159. Choi, H. S. *et al.* Targeted zwitterionic near-infrared fluorophores for improved optical imaging. *Nat. Biotechnol.* **31**, 148–153 (2013).
160. Hyun, H. *et al.* cGMP-Compatible preparative scale synthesis of near-infrared fluorophores. *Contrast Media Mol. Imaging* **7**, 516–524 (2012).
161. Xing, L. & Glen, R. C. Novel methods for the prediction of logP, Pka, and logD. *J. Chem. Inf. Comput. Sci.* **42**, 796–805 (2002).
162. Ahn, C. B. *et al.* Prognostic imaging of iatrogenic and traumatic ureteral injury by near-infrared fluorescence. *Quant. Imaging Med. Surg.* **9**, 1056–1065 (2019).
163. Kalkhof, S. & Sinz, A. Chances and pitfalls of chemical cross-linking with amine-reactive N-hydroxysuccinimide esters. *Anal. Bioanal. Chem.* **392**, 1–8 (2008).
164. Liu, C. Y. *et al.* M2-polarized tumor-associated macrophages promoted epithelial-mesenchymal transition in pancreatic cancer cells, partially through TLR4/IL-10 signaling pathway. *Lab. Investig.* **93**, 844–854 (2013).
165. Ji, Y. *et al.* Targeted molecular imaging of TLR4 in hepatocellular carcinoma using zwitterionic near-infrared fluorophores. *Quant. Imaging Med. Surg.* **9**, 1548–1555 (2019).
166. Li, Y. *et al.* Autophagy impairment mediated by S-nitrosation of ATG4B leads to neurotoxicity in response to hyperglycemia. *Autophagy* **13**, 1145–1160 (2017).
167. Kobayashi, H., Watanabe, R. & Choyke, P. L. Improving conventional enhanced permeability and retention (EPR) effects; What is the appropriate target? *Theranostics* **4**, 81–89 (2014).
168. Kang, H. *et al.* Size-Dependent EPR Effect of Polymeric Nanoparticles on Tumor Targeting. *Adv. Healthc. Mater.* **9**, 8–15 (2020).
169. Kang, H. *et al.* Renal Clearable Organic Nanocarriers for Bioimaging and Drug Delivery. *Adv. Mater.* **28**, 8162–8168 (2016).
170. Kelkar, S. S. & Reineke, T. M. Theranostics: Combining imaging and therapy. *Bioconjug. Chem.* **22**, 1879–1903 (2011).
171. Amano, K., Aihara, Y., Tsuzuki, S., Okada, Y. & Kawamata, T. Application of indocyanine green fluorescence endoscopic system in transsphenoidal surgery for pituitary tumors. *Acta Neurochir. (Wien).* **161**, 695–706 (2019).
172. Gehrman, J., Angenete, E., Björholt, I., Lesén, E. & Haglind, E. Cost-effectiveness analysis of laparoscopic and open surgery in routine Swedish care for colorectal cancer. *Surg. Endosc.* (2019) doi:10.1007/s00464-019-07214-x.
173. Li, P. *et al.* Early unplanned reoperations after gastrectomy for gastric cancer are different between laparoscopic surgery and open surgery. *Surg. Endosc.* **33**, 4133–4142 (2019).

174. Munabi, N. C. O., Olorunnipa, O. B., Goltsman, D., Rohde, C. H. & Ascherman, J. A. The ability of intra-operative perfusion mapping with laser-assisted indocyanine green angiography to predict mastectomy flap necrosis in breast reconstruction: A prospective trial. *J. Plast. Reconstr. Aesthetic Surg.* **67**, 449–455 (2014).

175. Sajedi, S., Sabet, H. & Choi, H. S. Intraoperative biophotonic imaging systems for image-guided interventions. *Nanophotonics* **8**, 99–116 (2018).

176. Zhu, B. & Sevick-Muraca, E. M. A review of performance of near-infrared fluorescence imaging devices used in clinical studies. *Br. J. Radiol.* **88**, (2015).

177. Miwa, M. & Shikayama, T. ICG fluorescence imaging and its medical applications. *2008 Int. Conf. Opt. Instruments Technol. Optoelectron. Meas. Technol. Appl.* **7160**, 71600K (2008).

178. Taşkın, S. *et al.* Laparoscopic near-infrared fluorescent imaging as an alternative option for sentinel lymph node mapping in endometrial cancer: A prospective study. *Int. J. Surg.* **47**, 13–17 (2017).

179. Frykman, P. K. *et al.* Evaluation of a video telescopic operating microscope (VITOM) for pediatric surgery and urology: A preliminary report. *J. Laparoendosc. Adv. Surg. Tech.* **23**, 639–643 (2013).

180. Buda, A. *et al.* Near-Infrared Sentinel Lymph Node Mapping With Indocyanine Green Using the VITOM II ICG Exoscope for Open Surgery for Gynecologic Malignancies. *J. Minim. Invasive Gynecol.* **23**, 628–632 (2016).

181. Mieog, J. S. D. *et al.* Toward optimization of imaging system and lymphatic tracer for near-infrared fluorescent sentinel lymph node mapping in breast cancer. *Ann. Surg. Oncol.* **18**, 2483–2491 (2011).

182. Gioux, S., Choi, H. S. & Frangioni, J. V. Image-guided surgery using invisible near-infrared light: Fundamentals of clinical translation. *Mol. Imaging* **9**, 237–255 (2010).

183. Ashitate, Y., Stockdale, A., Choi, H. S., Laurence, R. G. & Frangioni, J. V. Real-time simultaneous near-infrared fluorescence imaging of bile duct and arterial anatomy. *J. Surg. Res.* **176**, 7–13 (2012).

184. Chi, C. *et al.* Intraoperative imaging-guided cancer surgery: From current fluorescence molecular imaging methods to future multi-modality imaging technology. *Theranostics* **4**, 1072–1084 (2014).

Chapter 3

Vaccine visualisation using zwitterionic fluorophore 800-1C nanoparticles

3.1 Introduction

Immunity is so dynamic that we face many difficulties in fully understanding the kinetics of the cells and molecules involved in the immune system. These difficulties also apply to the depiction of mechanisms in laser adjuvant technology.[1–5] Critical information about the biodistribution and dynamics of vaccine antigens injected through various routes of administration, which would determine the successful delivery of these antigens to secondary lymphoid tissue,[6] is incomplete due to the lack of an optimal imaging tool.[7] The establishment of a reliable and reproducible trafficking method with a quantitative assessment of vaccine antigens is therefore desirable for optimising the formulation of clinical vaccines and revealing the pharmacokinetics and pharmacodynamics of the molecules. However, current methodologies for determining the longitudinal biodistribution of injected vaccine antigens *in vivo* are insufficient, as most studies focus on monitoring only immune cell behaviour.[8]

In addition, the physiochemical properties of vaccines, including size and surface charges, changes the mode of delivery, which in turn strongly influences subsequent adaptive immune responses, especially with skin-resident APCs.[9] For example, fluorescent polystyrene beads ranging from 500 to 2000 nm are mostly associated with migDCs, whereas small

particles ranging from 20 to 200 nm are associated with classical DCs (cDCs) and macrophages in LNs,[10] suggesting that smaller particles are freely drained into the lymphatics. Kang *et al*. further optimised the size of a model vaccine for the induction of CD8+ T cell responses using a series of ovalbumin (OVA) conjugates sized between 10 to 33 nm in hydrodynamic diameter (HD).[11] Considering that the actual size of pathogens ranges from 10 nm to several micrometres in diameter with various physicochemical properties taken into account,[12] a robust model system that faithfully replicates a clinical vaccine is desired.

To leverage this understanding, the current study implemented NIR zwitterionic fluorophores, which have shown great promise and potential in monitoring the *in vitro* behaviour of biomolecules when combined with tissue-specific NIR fluorophores.[13–16] Since NIR light penetrates biological tissues with lower scattering and absorption compared to visible light, it can provide high-resolution images of deep tissue structures.[17–20] ZW700-1C and ZW800-1C in particular have a number of advantages over classical organic dyes, as described in Chapter 2. Because of these advantages, zwitterionic fluorophores could be used to monitor the biodistribution and clearance of chemotherapeutic drugs and cytokines.[21–23]

This chapter reports a new imaging strategy to monitor the fate of model vaccines noninvasively after conjugation with zwitterionic fluorophores under the intraoperative NIR fluorescence imaging system. The study performed image analysis of vaccine trafficking along with a flow cytometry study to validate the quantitative biodistribution of NIR fluorescence images and to assess biological interactions between vaccines and immune cells.

3.2 Methodologies

3.2.1 Dynamic light scattering

Electron microscopes, TEM and scanning electron microscopes (SEMs) are common methods used to observe nanoscale materials and determine their size. Solid and dry materials, such as iron, silicon and polymers, can easily be visualised by TEM and SEM; however, biological molecules cannot be visualised, since these molecules require water to maintain their structure. In recent years, in order to conserve the structural information of biological samples, cryo-electron microscopy (cryo-EM) has been applied.[24,25] However, this technique requires very large experimental equipment. The actual diameter of a molecule, which cannot be measured with SEM or TEM, is called hydrodynamic diameter (HD).

Alternatively, dynamic light scattering (DLS) can be used to determine the size of nanoparticles.[26,27] A schematic image of DLS measurement is shown in Figure 3.1. Small particles suspended in solution are in Brownian motion, which is slower for larger molecules or particles and faster for smaller molecules or particles. When the 633-nm He-Ne laser is irradiated on particles in Brownian motion, the scattered light from these particles shows fluctuations corresponding to the speed of each motion. In the DLS method, laser light is irradiated on particles and the scattered light is observed by a detector (Figure 3.1). These light types interfere with each other, as in Young's light interference model. The intensity distribution due to the interference of scattered light also fluctuates continuously because the particles are constantly moving from their positions due to Brownian motion. For this reason, we can observe Brownian motion as a fluctuation of the scattered light intensity by using a pinhole or fibres.

The intensity of scattered light is described as a function of time (Figure 3.1). The autocorrelation function (ACF) is calculated by the following equations:

$$G(\tau) = \frac{\langle I(t) + I(t+\tau) \rangle}{\langle I(t) \rangle^2} \qquad (1)$$

$$G(\tau) = \alpha \exp(-2\Gamma\tau), \qquad (2)$$

where

$$\Gamma = Dq^2 \qquad (3)$$

$$q = \frac{4\pi n}{\lambda} \sin\left(\frac{\theta}{2}\right). \qquad (4)$$

In the equations, α is a constant number, D is a diffusion coefficient, n is a refractive index of the solution, λ is a wavelength of the light source, and θ is the angle at which the detector is located. Together with (3) and (4), the HD (d) is described in the Stokes-Einstein equation as follows:

$$d = \frac{k_B T}{3\pi\eta D}, \qquad (5)$$

where k_B is the Boltzmann's constant, T is an absolute temperature, and η is the viscosity of the solvent.[28]

To validate this methodology, Hoo *et al*. compared DLS, TEM and atomic force microscopy (AFM) using 20-nm and 100-nm polystyrene nanoparticles.[28] For 100-nm particles, all three microscopes showed similar diameters. For 20-nm particles, AFM showed a smaller size than in DLS and TEM, while DLS and TEM had similar results, indicating the accuracy and validity of DLS for 20-nm and 100-nm particles.

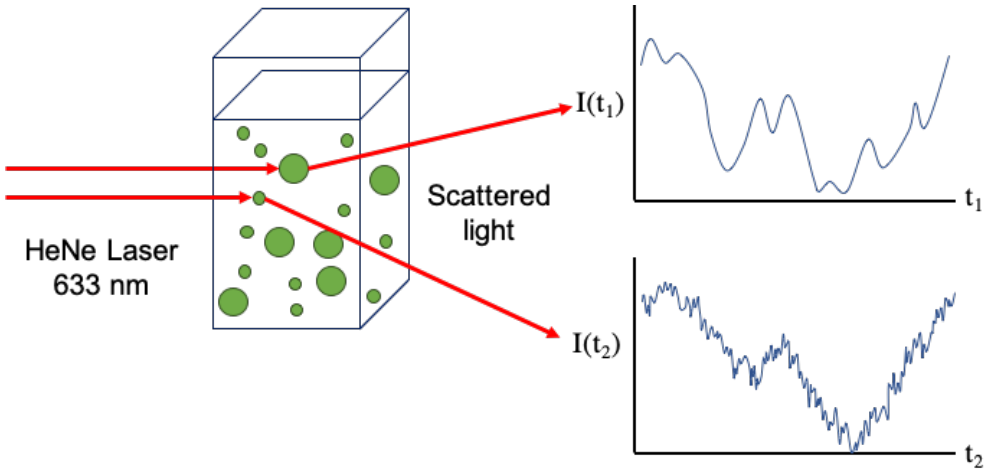

Figure 3.1 Schematic image of dynamic light scattering (DLS) method. A 633-nm He-Ne laser is used as a light source. The intensity of the interfered signal is described as a function of time. The autocorrelation function (ACF) of the intensity followed by the diameter of the particles are calculated by the fluctuation of intensity.

3.2.2 Flow cytometry

For over a half century, flow cytometry has been a powerful tool for sorting and characterising both live and fixed cells based on fluorescence marked on membrane proteins and intracellular molecules. It was invented in the late 1960s by Bonner, Sweet, Hulett and Herzenberg, who called it the fluorescence-activated cell sorter (FACS).[28] Flow cytometry enables high-throughput screening to observe cells in single-cell resolution. Unlike a microscope, a flow cytometer does not show images of cells, but it does have the advantage of being able to automatically and objectively measure various parameters for each cell at a high resolution.[29,30]

An image of the flow cytometry system is depicted in Figure 3.2. The figure is based on the structure of a Fortessa flow cytometer (BD Biosciences, NJ, USA). Briefly, the cytometer is equipped with four different lasers for excitation: 405-nm violet, 488-nm blue, 561-nm green and 640-nm red. First, an operator prepares cell samples labelled by fluorophore-coupled antibodies (Recently, a countless number of antibodies with fluorophores of different colours have become available worldwide). Second, the mixture of cells tagged with fluorescent dyes are loaded in the system. When the cell suspension is running through the cytometer, the four laser lights are illuminated on the cell. Finally, the fluorescence signal is captured by photomultiplier tubes via several filters and mirrors; meanwhile, the forward- and side-scattered light are used in the system to determine the size of cells. By doing so, a specific type of cell from an organ or tissue, both of which include a tremendous number of different cells, can be distinguished.

Since it offers a high signal detection yield of over 10,000 cells per second, flow cytometry is useful for identifying a small number of unique cells within a given tissue or organ. For instance, intertumoral $CD8^+$ T cells drive antitumoral immunity; however, the number of these cells in tumours is often limited.[31–33] To address this, flow cytometry is chosen not only to discover a few unique cells but also to explore the characteristics and activation status of the cells.[34,35]

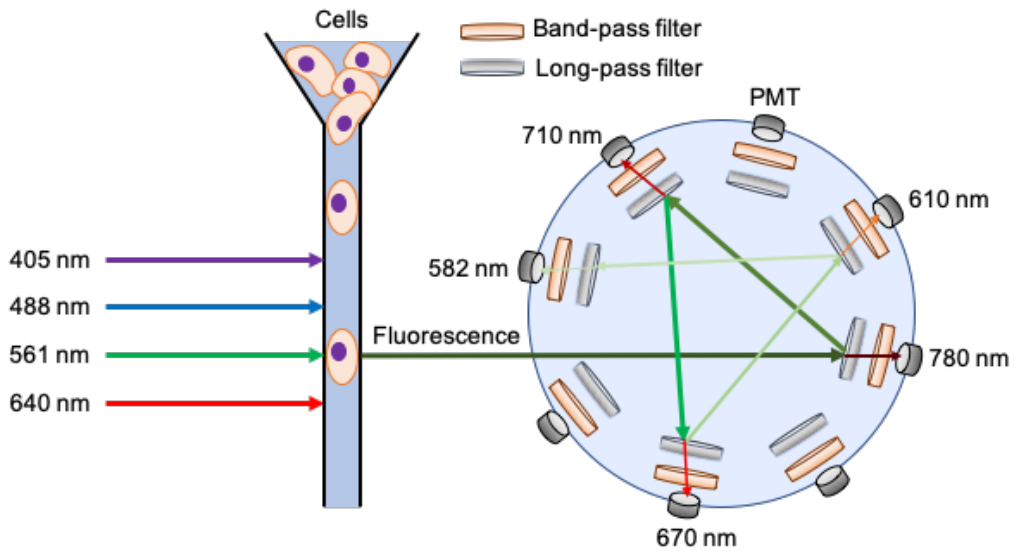

Figure 3.2. Schematic image of Fortessa flow cytometer. Four laser lights are irradiated on the flowing cells. The fluorescent signal travels into a circular filter set. Although this figure shows only one set of detectors for the green channel, it also has different filter sets for violet, blue and red excitation lasers. This feature offers high-throughput data acquisition of over 10,000 cells/s.

3.3 Materials and methods

3.3.1 Bioconjugation of zwitterionic fluorophore 800-1C

The NHS ester form of ZW800-1C (quantum yield (QY): 23.9% at 754 nm)[13,15,36] in dimethyl sulfoxide (DMSO) stock solution was conjugated with chicken egg ovalbumin protein (OVA, PDB: 1OVA, MP Biomedicals, CA) as previously described.[37] Briefly, 400 nmol of ZW800-1C NHS ester was incubated with 20 nmol of OVA in 240 µL of PBS, pH 8.0, with gentle mixing at room temperature (RT) for 3 h. The OVA-ZW800-1C (OVA-ZW) conjugates were purified by using Bio-Gel P-6 columns (Bio-Rad, Hercules, CA) and membrane filtration columns (Sartorius Stedim Lab, UK). Then, the purified OVA-ZW was further conjugated with two different sizes (20 nm and 100 nm) of aminated silica nanoparticles (SiNP, NanoComposix, CA) in the presence of 4-(4,6-dimethoxy-1,3,5-triazin-2-yl)-4-methylmorpholinium chloride (DMTMM, Sigma Aldrich, Saint Luis, MO) at RT in distilled water (DIW). The size of each SiNP, which was determined by electron microscopy by the manufacturer, was 22.6 ± 2.7 and 97.5 ± 5.0 nm, respectively. The average HD before conjugation, as measured by DLS, was 71.1 ± 0.2 or 127.1 ± 1.5 nm. The reaction ratio of OVA-ZW to SiNPs was 10:1 and 360:1 in

molar equivalent for ONP1 and ONP2, respectively. The concentration of DMTMM was adjusted to be the same as that of OVA-ZW. After a gentle reaction for 3 h, non-conjugated OVA-ZW was eliminated by centrifuge. The average HD of ONP1 and ONP2 was measured by DLS (Zetasizer Nano ZS, Malvern, UK) at 633 nm. In addition, in order to measure the actual size of ONP1 and ONP2, freshly prepared ONP1 and ONP2 in ultra-pure water were dropped onto a carbon-coated copper grid (200 mesh, Ted Pella, Redding, CA) and dried in a vacuum chamber overnight. TEM images were obtained using Tecnai G2 Spirit Bio TWIN (FEI Company, OR) at the core electron microscopy facility, at Harvard Medical School.

The labelling ratio of ZW800-1C on SiNPs was calculated with a UV-Vis-NIR spectrophotometer (USB-ISS-UV/VIS, Ocean Optics, FL) using Beer-Lambert's Law to determine the concentration of each compound. The extinction coefficients for OVA, ZW800-1C, 20-nm SiNP and 100-nm SiNP were 30,590 /Mcm, 67,500 /Mcm, 249,700 /Mcm and 188,249,400 /Mcm measured at 280 nm, 753 nm and 350 nm, respectively. For calculating the extinction coefficient of the SiNPs, where the interference from the absorbance of albumin and fluorophores is minimal, 350 nm was chosen. As a reference, the measurement of an unconjugated SiNP solution was performed to determine the amount of conjugated ZW and OVA in SiNPs. The NHS ester form of Cy5 (extinction coefficient: 250,000, QY: 30% at 649 nm, GE Amersham) was conjugated with OVA using the same procedures as those for OVA-ZW.

3.3.2 Animal models and vaccine administration

Six-week-old male C57BL/6J mice (stock #000664) were purchased from Jackson Laboratories (Bar Harbor, ME) and acclimated for at least 2 weeks at Massachusetts General Hospital (MGH). Mouse hair was removed 1 day prior to injection using a commercial depilatory cream (Nair, Church & Dwight Co., Ewing, NJ). For imaging and the flow cytometry study, three different sizes of model vaccines – OVA-ZW, ONP1 and ONP2 – were intradermally (id) injected into the footpads of the mice ($n = 4$). The injection volume was fixed to be 5 μL at a concentration of 20 μM ZW fluorophores. For a control biodistribution study, 100 μL of 20 μM OVA-ZW was injected intravenously (iv) and retro-orbitally into CD-1 mice ($n = 4$). All animal procedures were approved by the MGH IACUC (protocol #2017N000067 and 2009N000103) and performed under the Public Health Service Policy on Humane Care of Laboratory Animals.

3.3.3 Real-time intravital fluorescence imaging

For real-time NIR fluorescence imaging, the multispectral FLARE imaging system was used (Figure 3.3, 3.4).[38,39] Briefly, 660 nm (excitation for Cy5) and 760 nm (for ZW800-1C) multimode laser diodes (RPMC Lasers, O'Fallon, MO) were coupled with a 1 to 4 breakout glass optical fibre (NA = 0.55, Leoni AG, Germany) for an excitation light source. The irradiance at a focal plane was adjusted to be 7 mW/cm^2 over a 10-cm diameter FOV. Mice were anesthetised with isoflurane and laid prone under a prism-based multispectral CCD camera (JAI A/S, Denmark), in which prisms were equipped (Figure 3.4). Colour and NIR images were simultaneously captured by the camera with multiple exposure times between 100 and 2000 ms. The FOV included the injection site and popliteal and sciatic LNs. The images were acquired before and immediately after injection, as well as at 1, 6, 24, 48 and 72 h post-injection. After 72 h, each major organ was dissected, and the fluorescence image was captured.

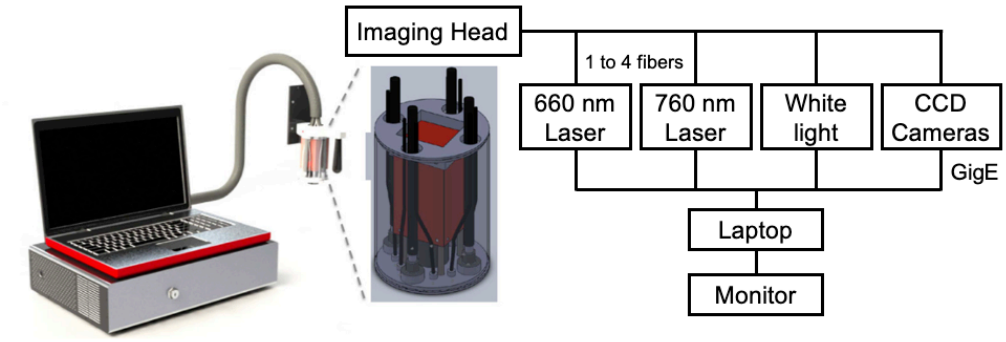

Figure 3.3. KFLARE imaging system. Two lasers, a white light for the illumination source and CCD cameras were controlled by a computer. Gigabit Ethernet (GigE) interface was installed.[40]

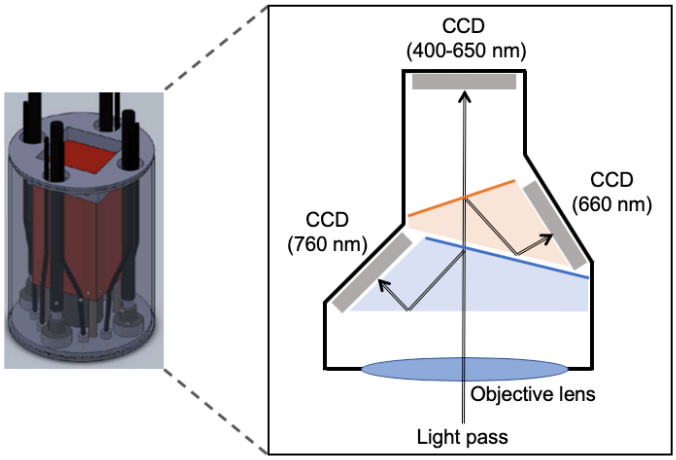

Figure 3.4. Structure of KFLARE imaging head. The imaging head was equipped with three CCD sensors and two dichroic prisms that enabled simultaneous colour and NIR imaging.

3.3.4 Quantitation and statistical analysis

In order to quantify the fluorescent signal, the signal-to-background ratio (SBR) was introduced. Image processing and analysis were carried out using ImageJ software (National Institutes of Health). First, the sensitivity of the KFLARE system to ZW800-1C was assessed. ZW800-1C solutions were adjusted to be 10, 20, 50, 100, 200 and 500 nM, and 1, 2, 5 and 10 M in DMSO. The solutions were then loaded into glass capillaries. The capillaries were placed in the centre of the FOV under the KFLARE camera. The images were taken at 200, 1000 and 2000 ms exposure time. The SBR was calculated based on the intensity of the ZW800-1C solution (I_{ROI}) and DMSO as autofluorescence (I_{Auto}):

$$SBR = \frac{I_{ROI}}{I_{Auto}} \qquad (6)$$

For *in vivo* analysis, approximately 50×50 pixels around the injection site and LNs were cropped from original NIR grayscale images, and noise was removed by a 3×3-pixel median filter. Next, a region of interest (ROI) was defined automatically and quantitatively by means of an iterative selection method, which determined a threshold between the signal and the background on a filtered image (Figure 3.5). The average intensity of the resulting ROI on the

original image yielded the level of the signal. The dye-free skin intensity (auto) was also measured on each image and defined as background. I_{ROI} denotes the average intensity of an ROI, and I_{Auto} represents the intensity of the mouse dye-free skin. The SBR at different time points was normalised based on the initial intensity in the footpad and LNs at $t = 0$. For the analysis of LNs, a series of images with an exposure time of 2000 ms were used, while 100 ms was used for footpad images. All NIR fluorescence images were normalised identically for all conditions of the experiment. Animal results were presented as mean ($n \geq 3$) ± standard errors (SEMs), and curve fitting was performed using Prism version 8 software (GraphPad, San Diego, CA). One-way analysis of variance (ANOVA) followed by a Tukey's test was performed for the statistical analysis. A P value of less than 0.05 was considered significant: *$P < 0.05$, **$P < 0.01$, ***$P < 0.001$, ****$P < 0.0001$.

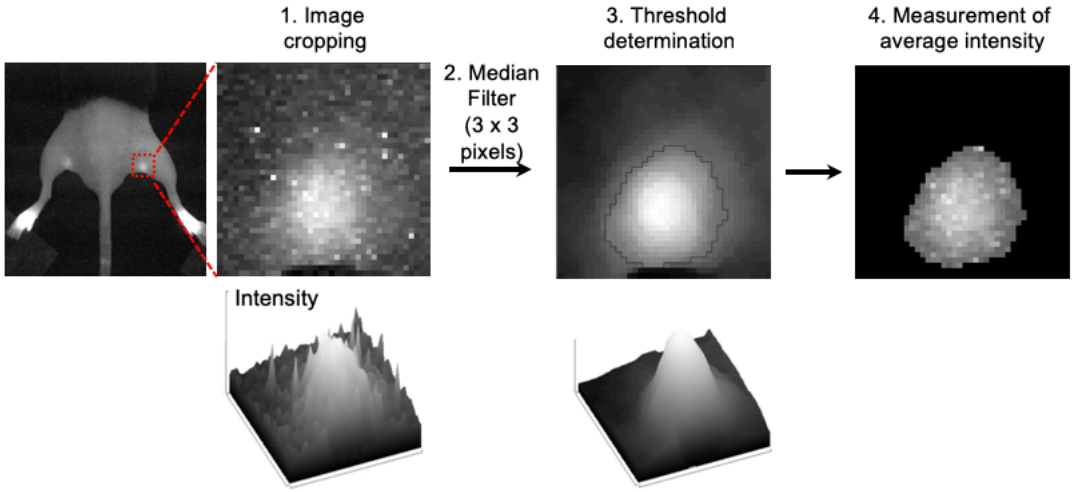

Figure 3.5. Quantitative ROI determination and intensity measurement scheme. All NIR fluorescence images were normalised identically for all conditions of the experiment to determine the ROI quantitatively. First, approximately 50×50 pixels of an image were cropped around the signal region of the LN. Second, a 3×3 median filter was applied to the average noise. Third, an LN signal threshold was identified by an iterative selection method to determine the ROI. Finally, the average intensity of the ROI was measured on the original image.

3.3.5 Stability test of model vaccines

OVA-ZW was dissolved in PBS, pH 7.4, containing 10% serum at a concentration of 0.1 or 1.0 μM ZW800-1C. The OVA-ZW solutions were sealed into glass capillary tubes (Fisher Scientific, Waltham, MA) and then incubated for 0, 1, 6, 24, 48 and 72 h at 37˚C in a 5% CO_2 incubator. After incubation, the fluorescence signal of each sample in a capillary tube was captured using the FLARE imaging system, and the SBR for each capillary tube was calculated as described above.

3.3.6 Flow cytometry analysis of lymph nodes

For the analysis of immune cells by flow cytometry with limited filter sets, ZW700-1C was used in place of ZW800-1C because both fluorophores have identical chemical structures except for the length of the polymethine backbone, thus showing an excitation peak at 643 nm and an emission peak at 663 nm, respectively.[41] The NHS ester form of ZW700-1C was conjugated on the model vaccines using the same conjugation procedures as those for ZW800-1C.[37] Three days after intradermal injection, popliteal LNs were isolated from each mouse. LNs were dissociated with a collagenase D/DNase solution (2.5 mg/mL collagenase and 100 unit/mL1 DNase, Roche, the Netherlands) for 25 min followed by incubation with an ethylenediaminetetraacetic acid (EDTA) solution (10 mM, Invitrogen, CA) for 5 min at 37˚C.[4] The cells were labeled for F4/80 (BM8, BioLegend), I-A/I-E (M5/114.15.2, BioLegend), CD11c (N418, BioLegend), CD103(2E7, BioLegend), CD11b (M1/70, BioLegend), Langerin (4C7, BioLegend), Ly6C (AL-21, BioLegend), Ly6G (1A8, BioLegend), and Live/Dead Fixable Aqua (Life Technologies) to identify specific receptors against APC subsets.[4] The fluorescence data were acquired using a 640-nm excitation laser on a Fortessa flow cytometer (BD Biosciences, Franklin Lakes, NJ) and analysed with FlowJo software version 10 (FlowJo Co., Ashland, OR). The cDCs were identified based on $CD11c^{hi}$ and I-A/I-E intermediate expression, whereas migDCs were classified as CD11c intermediate and I-A/$I\text{-}E^{hi}$ expression groups. For further classification, cDCs were divided into two groups, $CD103^+$ and $CD103^-$, while migDCs were divided into four groups based on the CD11b and Langerin (Lang) expressions: $CD11b^+$ $Lang^+$, $CD11b^+$ $Lang^-$, $CD11b^-$ $Lang^+$ and $CD11b^-$ Lang subsets. Macrophages and monocytes were identified based on $CD11b^+$ I-A/$I\text{-}E^-$ expression. $F4/80^+$

$CD11c^-$ cells were then identified as macrophages, while the $CD11c^-$ $Ly6G^-$ population was further divided into $Ly6C^-$ and $Ly6C^+$ monocyte (inflammatory monocyte) groups.[4] To evaluate the transportation of each model vaccine to the LNs, the number of ZW700-1C-positive cells was measured for each subpopulation, of which signal thresholds were determined by fluorescence minus one control (FMO) group.

3.3.7 Histological analysis of lymph nodes

Mouse LNs were isolated 72 h post-intradermal injection of model vaccines. LNs were fixed with 4% paraformaldehyde (Thermo Scientific, Rockford, IL) and incubated in 30% sucrose solution (Merck, Germany) overnight. Ten-μm-thick frozen sections were cut by a cryostat (Leica, Germany). Images were acquired on a 4-channel NIR fluorescence microscope (TE2000U, Nikon, Japan) and CCD camera (C4742-80-12AG, Hamamatsu Photonics, Japan). All the images were binarized by means of an iterative selection method to define areas positive for fluorescence signals. To analyse the spatial relationship between fluorescent cells and their locations in the LNs, areas within 15 μm of the edge of the LNs were defined as subcapsular sinus (SCS), and the others were considered as the cortex.[42] The portion of areas positive for fluorescence was measured and calculated for each ROI using ImageJ.

3.3.8 Statistical analysis

An ANOVA followed by Tukey's multiple comparison tests or Student's unpaired two-tailed *t* test were performed using Prism 8. The mean ± SEMs were shown for all image analyses on the FLARE system and via fluorescence microscopy. The results of the flow cytometry data analysis were presented in box-and-whisker plots with the median ± 95% confidence interval.

3.4 Results

3.4.1 Conjugation of zwitterionic fluorophore 800-1C on model vaccines

To visualise the biodistribution and trafficking of vaccines, a ZW800-1C was chosen to label on a model vaccine, OVA. ZW800-1C is an NIR fluorophore with an excitation peak at 753 nm and an emission peak at 772 nm, and it features minimal fluorophore–tissue interactions.[43,44] OVA, on the other hand, is a protein widely used as an antigen in immunological studies. These characteristics allow the conjugated vaccine to distribute independently from the fluorophore. As shown in Figure 3.6a, the NHS ester form of ZW800-1C (ZW800-1C NHS) was prepared and conjugated with OVA to yield the bioconjugated OVA-ZW800-1C (OVA-ZW). Next, OVA-ZW was further conjugated on two differently sized silica nanoparticles (SiNP-20 nm and SiNP-100 nm) because it is known that the size of the vaccine is one of the key factors in determining its emigration, via draining, from the skin into the LNs after intradermal injection.[45] After purification using membrane filtration columns, the average HD of SiNP conjugated with OVA-ZW (ONP) was measured by DLS, which was found to be 183.1 ± 2.1 nm and 277.2 ± 1.6 nm for ONP1 and ONP2, respectively (Figure 3.6b-c). The average dye-labelling ratio on each NP was determined to be 4.7 and 205 for ONP1 and ONP2, respectively, calculated by using an UV-Vis spectrophotometer (Figure 3.7a-b).

To determine the dynamic range of fluorescence signals, a serial dilution of OVA-ZW solution was prepared in serum-containing media and imaged under the dual-channel FLARE imaging system.[38,39] A linear relationship was observed between the fluorescence emission of OVA-ZW and its concentrations from 20 nM to 50 μM, indicating that a wide range of vaccine concentrations can be evaluated quantitatively and accurately under the FLARE system (Figure 3.7c). Images of the ONPs captured by TEM also revealed that the ONPs were homogenous in size after the conjugation and evenly distributed in the solution without significant aggregation (Figure 3.7d-e).

Next, the stability of OVA-ZW in a biological setting was assessed. OVA-ZW in PBS containing 10% serum was incubated over 72 h at pH 7.4 and at 37°C. The fluorescence signal was stable over the entire period of incubation with no change in the SBR (Figure 3.6d). This result demonstrates that the conjugated vaccine has stable optical properties in a physiological condition.

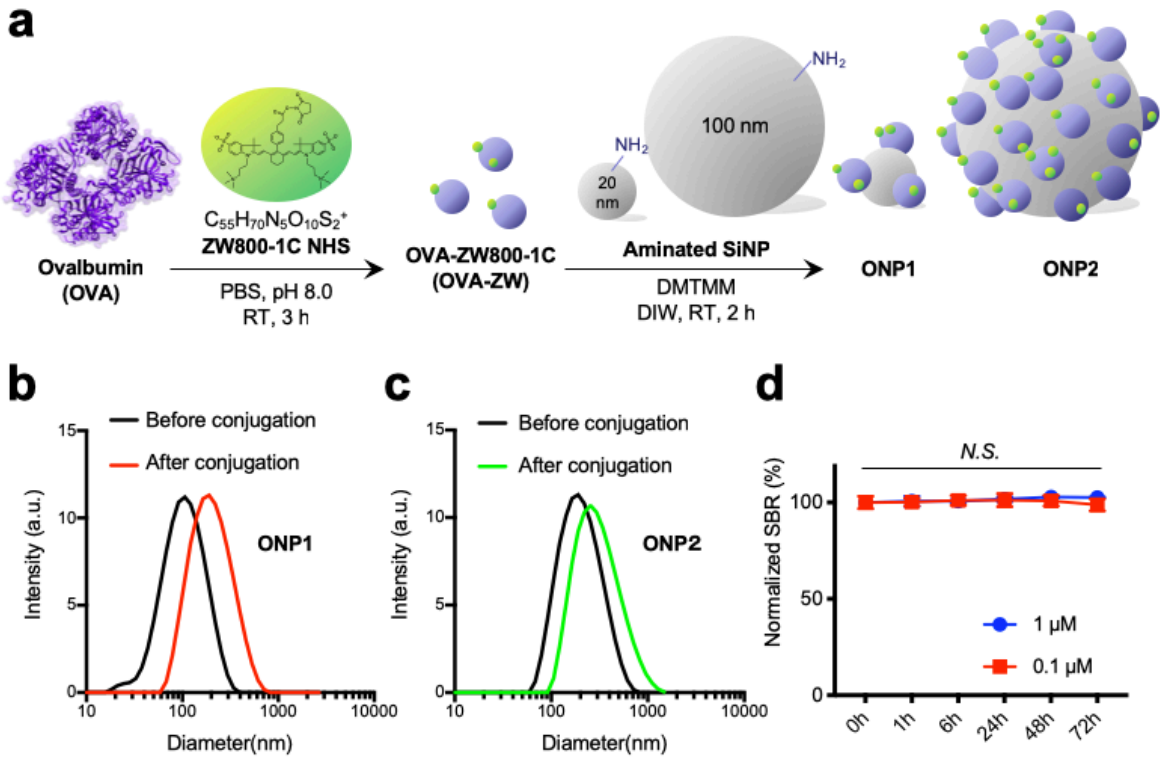

Figure 3.6. Preparation of model vaccines using NIR-fluorescent ZW800-1C. (a) A schematic drawing of bioconjugation. ZW800-1 NHS ester (ZW) was conjugated on OVA (OVA-ZW) in PBS, pH 8.0, followed by further conjugation on SiNPs in DIW. (b), (c) The average HD of each ONP before and after conjugation was measured by DLS. The averages of three independent measurements are shown. (d) Time-course SBR in serum-containing media confirmed the physicochemical and optical stability of ONPs. The fluorescence signal was measured by the FLARE NIR fluorescence imaging system (n = 3, mean ± SEM). A P value of less than 0.05 was considered significant: *N.S.*, not significant by one-way ANOVA.

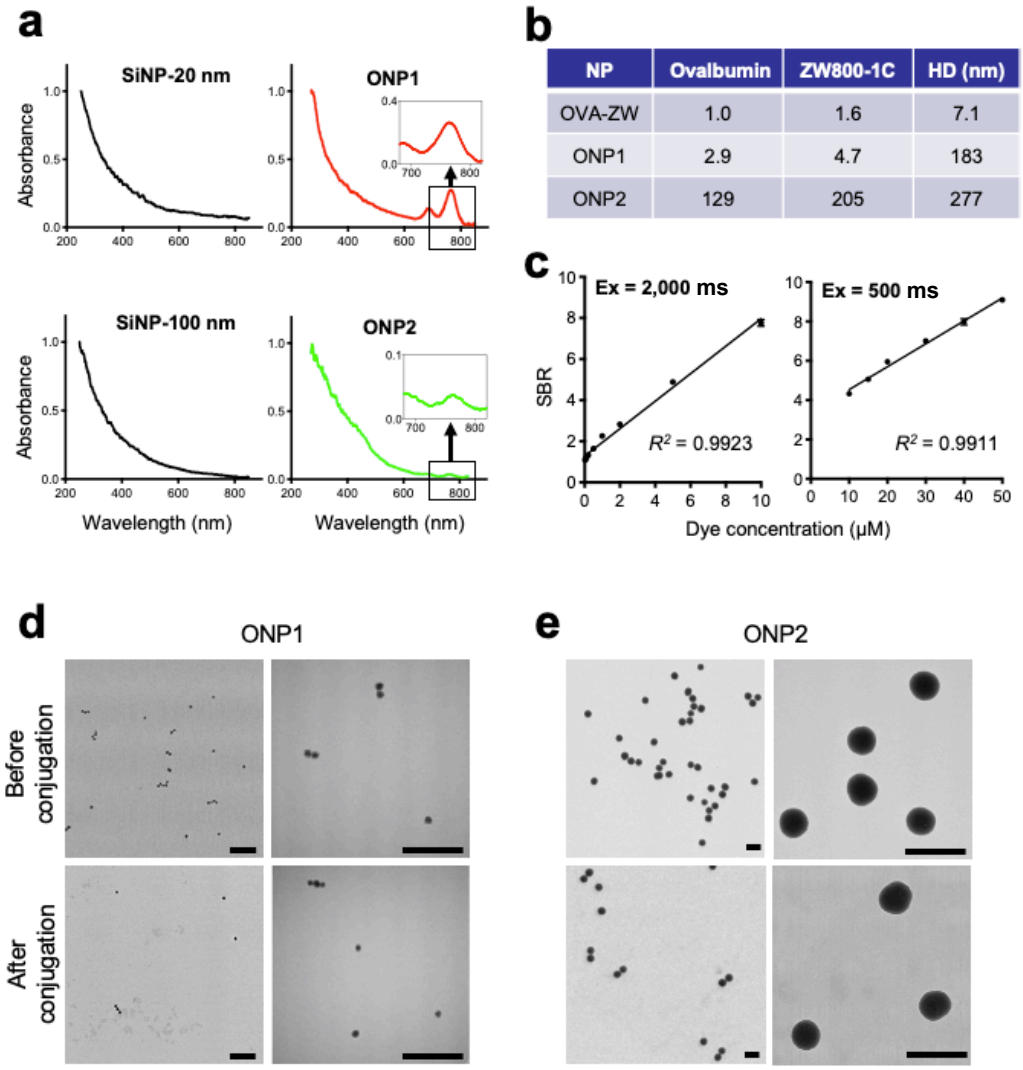

NP	Ovalbumin	ZW800-1C	HD (nm)
OVA-ZW	1.0	1.6	7.1
ONP1	2.9	4.7	183
ONP2	129	205	277

Figure 3.7. Determination of dye labelling ratio on model vaccines. (a) The labelling ratio of each ONP was determined using Beer-Lambert's Law, and the absorbance spectra of each model vaccine was measured with a UV-Vis-NIR spectrophotometer before and after conjugation. (b) Summary of labelling ratio and HD of OVA-ZW, ONP1 and ONP2. (c) Relationship between the concentration of ZW800-1C and its fluorescence signal on the FLARE system at different exposure times (left: 2000 ms vs. right: 500 ms). Note that there is a linear relationship between the signal and the dye concentration (n = 3, mean ± SEM.). (d-e) TEM images of (d) ONP1 and (e) ONP2 dispersed in ultrapure water at different magnifications. Scale bars = 200 nm.

3.4.2 Assessment of KFLARE imaging system

An image of glass capillaries is shown in Figure 3.8. These capillaries contain 10 nM to 2 µM of ZW800-1C in DMSO. A clear fluorescence signal can be observed above 100 nM. In contrast, above 2 µM, only a saturated signal can be observed at 1000 ms and 2000 ms exposure time. On the other hand, it is barely possible for the naked eye to distinguish 10, 20 and 50 nM. Figure 3.9 shows the correlation of the SBR and the concentration of ZW800-1C at different exposure times. By applying the concept of the SBR, a small difference in the fluorescent signal below 50 nM could be distinguished. The linearity, which Figure 3.7c previously showed, was lost in the range of 10 nM to 1 µM (R^2 = 0.8961, 0.6608 for 1000, 2000 ms, respectively.)

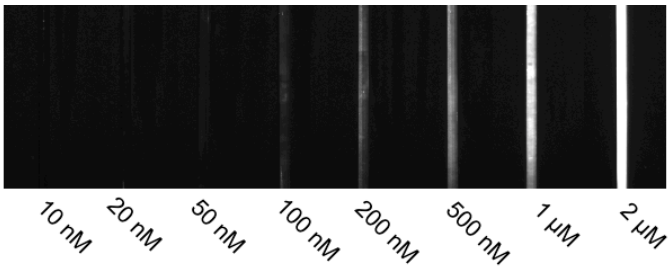

Figure 3.8. Glass capillaries filled with ZW800-1C solution.
5 µM and 10 µM solution shows blight signal, whereas 10-20 nM solutions are not visible.
Exposure time = 1000 ms.

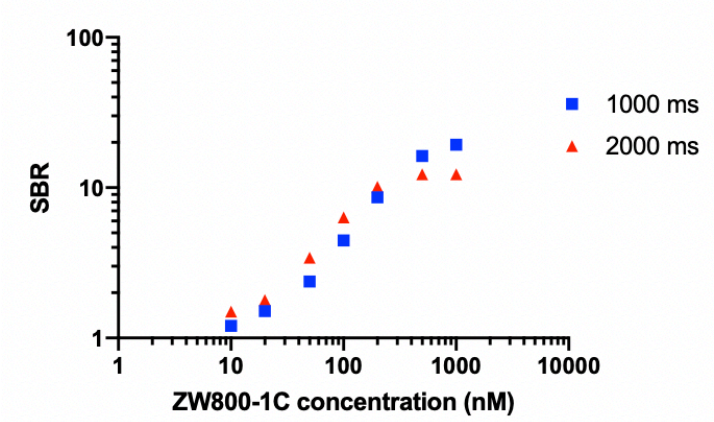

Figure 3.9. The SBR for the 760-nm channel with 1000 and 2000 ms exposure times. Average of 65 pixels.

3.4.3 Size-dependent accumulation of vaccines in lymph nodes

Small vaccine antigens directly enter the lymphatics and drain into the LNs within 30 min, while larger antigens taken up by DCs drain into the LNs slowly over 24 h after intradermal vaccination.[46] It was hypothesised that the accumulation of fluorescence signals would be dependent on the size of the ONPs. An intradermal injection model in the footpad was chosen because the lymphatic flow is well characterised, and this model is suitable for time-course monitoring of vaccine trafficking.[10] To test the hypothesis, the fluorescence signal in real time upon the intradermal injection of different-sized model vaccines on the footpads of mice was measured (Figure 3.10d). The signal in the popliteal LN injected with OVA-ZW showed a rapid increase 1 h post-intradermal injection and retained a high level until 6 h post-injection, followed by a gradual decrease (Figure 3.10). In contrast, ONP1 and ONP2 accumulated draining into the LNs steadily over 72 h post-injection. The fluorescence signal intensity at early time points was significantly higher in the OVA-ZW group compared to ONP1 or ONP2 at 1–6 h post-injection (Figure 3.10a-b, $P < 0.0001$). Since the brightness of each model vaccine was variable despite the same injection dose, the SBR values were converted to concentrations based on the labelling ratio (Figure 3.10c). The concentration of OVA-ZW in the popliteal LN was significantly higher than that of ONP1 or ONP2 over 72 h ($P < 0.01$). The largest ONP2 (277 nm) showed the lowest concentrations in the LNs over the time course, indicating that the concentration in the draining LNs was inversely proportional to the HD of model vaccines after intradermal injection (Figure 3.10c).

The SBR in the LNs and at the injection site were compared because strong residual signals were observed in the footpad even at 72 h post-injection (Figure 3.10d). The SBR in the footpad was significantly higher than that of the LNs in any experimental group (LN vs. the injection site: $P < 0.0001$ for OVA-ZW, $P < 0.0016$ for ONP1, $P < 0.0298$ for NP2 at 72 h), suggesting that a significant fraction of the injected vaccine remained in the injection site regardless of size. Interestingly, the level of the remaining dose at the injection site was significantly lower in the OVA-ZW group compared to the ONP1 or ONP2 groups (OVA-ZW vs. ONP1: $P = 0.0029$; OVA-ZW vs. ONP2: $P = 0.0160$). This result coincides with the finding in the literature that vaccines smaller than 100–200 nm can enter the lymphatics directly and be transported to the draining LNs.[10,45,47] It could be consistently observed that, upon injection, OVA-ZW rapidly showed up in the lymphatics close to the injection site and accumulated into

the popliteal LN shortly thereafter, while minimal to no signals were observed in the lymphatics from ONP2-injected mice 60 min post-injection (Figure 3.10e).

The advantages of the renal clearable ZW800-1C over conventional organic dyes in monitoring the biodistribution of vaccines were observed. Towards this end, the intradermal injection of OVA-ZW or Cy5 was performed on the footpads of mice (Figure 3.11). The signal in the popliteal LN injected with OVA-ZW or Cy5 showed a comparable increase 1 h post-intradermal injection (Figure 3.11b). However, the OVA-Cy5 group gradually lost fluorescence signals with a concomitant increase in the background (Figure 3.11a), resulting in a poor SBR beyond 24 h post-injection (Figure 3.11b). Consistently, higher fluorescence signals were observed across multiple organs but were lower in LNs in the OVA-Cy5 group compared to those in the OVA-ZW group at 72 h (Figure 3.11c-d).

Taken together, these results indicate that the zwitterionic ZW800-1C is a reliable tool for tracing the destination of injected antigens, and that the NIR fluorescence signals derived from ZW800-1C faithfully represent the *in vivo* behaviour of model vaccines under the real-time intraoperative imaging system.

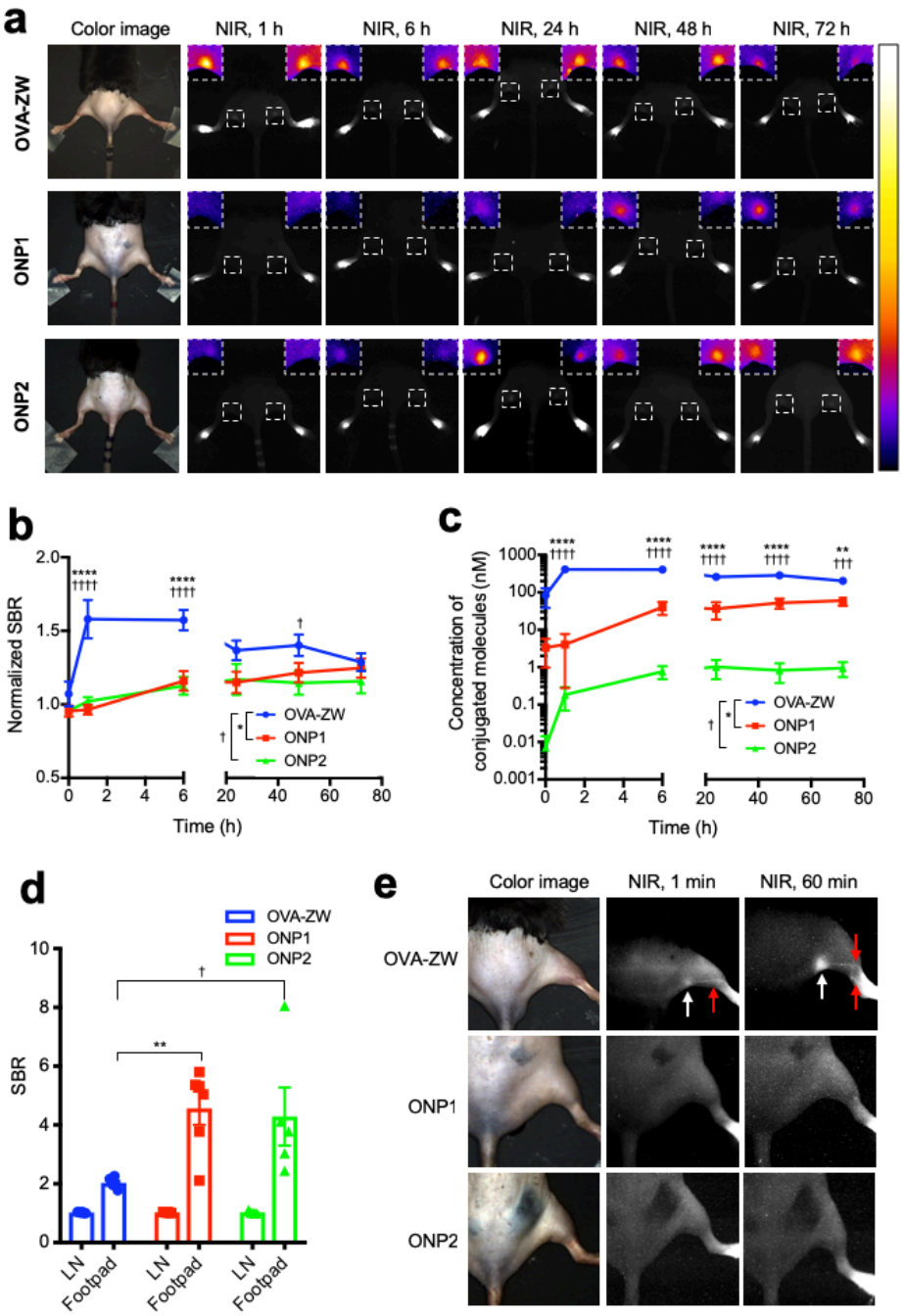

Figure 3.10. Quantitative image analysis of vaccine trafficking in the draining LNs. Trafficking of the model vaccines into draining LNs was monitored on the FLARE system and was evaluated by image analysis. (a) Representative images of mice 0, 1, 6, 24, 48 and 72 h post-injection with model vaccines. Insets show magnified pseudocolour images of popliteal LNs. (b) The SBR of popliteal LNs was calculated by comparison with background skin signals (n = 4, mean ± SEM). (c) Quantitative tissue concentrations of model vaccines in the popliteal LNs. SBRs were converted to concentrations based on the labelling ratio (n = 4, mean ± SEM). (d) The SBR of LNs and the injection site were compared (n = 5-6, mean ± SEM). (e) Representative LN images injected with model vaccines 1 min and 60 min prior to imaging. (b–d) A P value of less than 0.05 was considered significant: *P < 0.05; **P < 0.01; ***P < 0.001; ****P < 0.0001 by one-way ANOVA followed by Tukey's multiple comparisons test.

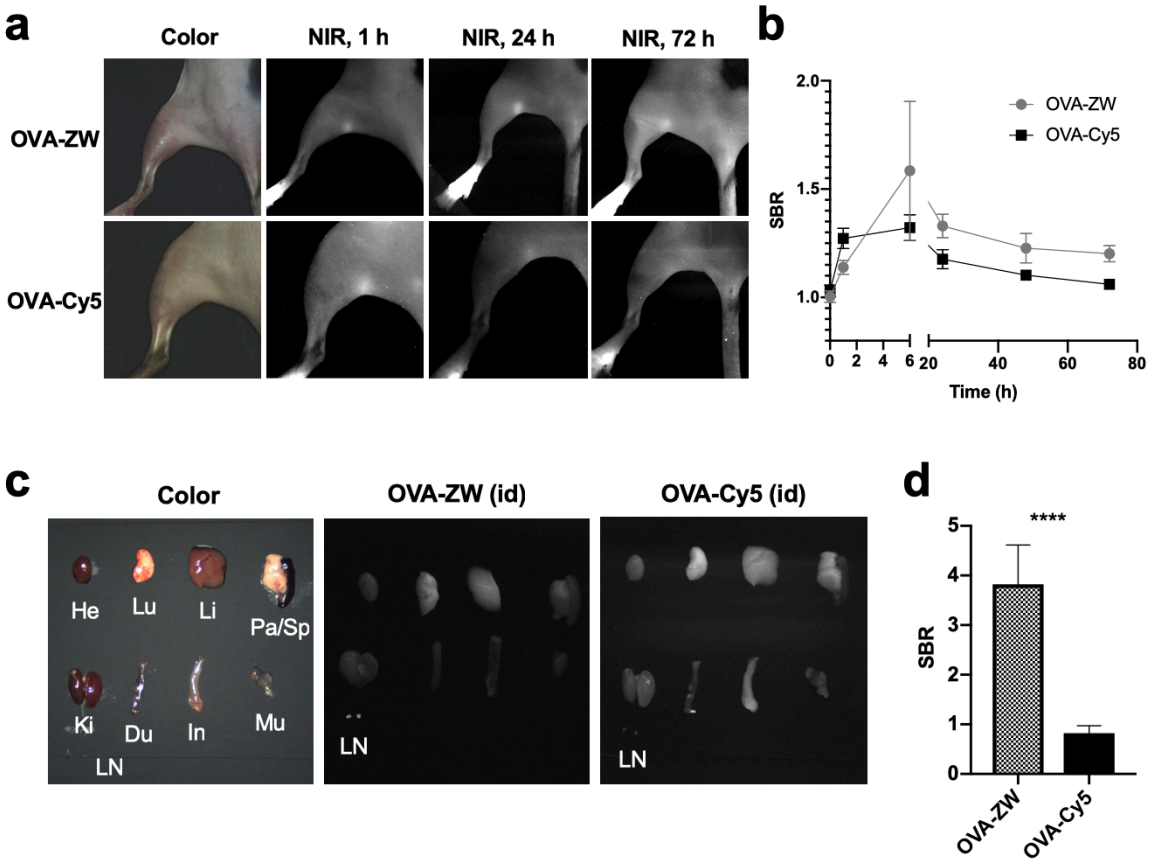

Figure 3.11. Comparison of fluorescence signals from a model vaccine conjugated to ZW800-1C or Cy5 after intradermal injection. (a) Representative images of mice 1, 24 and 72 h post-injection with the conjugated model vaccines. The irradiance of both 660-nm and 760-nm lasers were adjusted to be 1.5 mW/cm2 on the FLARE system. (b) The SBR of popliteal LNs was calculated by comparison with background skin signals (n = 3-4, mean ± SEM). (c) Major organs, including the heart (He), lungs (Lu), liver (Li), pancreas (Pa), spleen (Sp), kidneys (Ki), duodenum (Du), intestine (In), muscles (Mu) and lymph nodes (LNs), were resected and imaged 72 h post-intradermal injection of the conjugated model vaccine. (d) The SBRs of LNs are compared with the fluorescence signals of muscles (n = 4-6, mean ± SEM). (d) A P value of less than 0.05 was considered significant: ****$P < 0.0001$ by Student's t-test.

3.4.4 Biodistribution of model vaccines

To evaluate the biodistribution and clearance of model vaccines, intradermal injection (id) and intravenous injection (iv) were compared in CD-1 mice, which were euthanized 72 h post-injection LN (Figure 3.12). The mice injected with OVA-ZW intravenously through the tail vein showed major fluorescence signals in the liver and spleen, which may indicate hepatotoxicity, while no signal was found in LNs (Figure 3.12a-b). These results are consistent with the literature showing that bloodborne antigens are rapidly scavenged by the liver[48] and spleen.[49] In contrast, the mice injected with model vaccines intradermally showed faint signals in the major organs, including the lungs, liver, pancreas and kidneys, while high fluorescence signals were observed in the popliteal LNs regardless of the size of the model vaccines (Figure 3.12a-b). These results confirm that the fluorescence signal from ZW800-1C represents the biodistribution and clearance of the model vaccine under the NIR fluorescence imaging system.

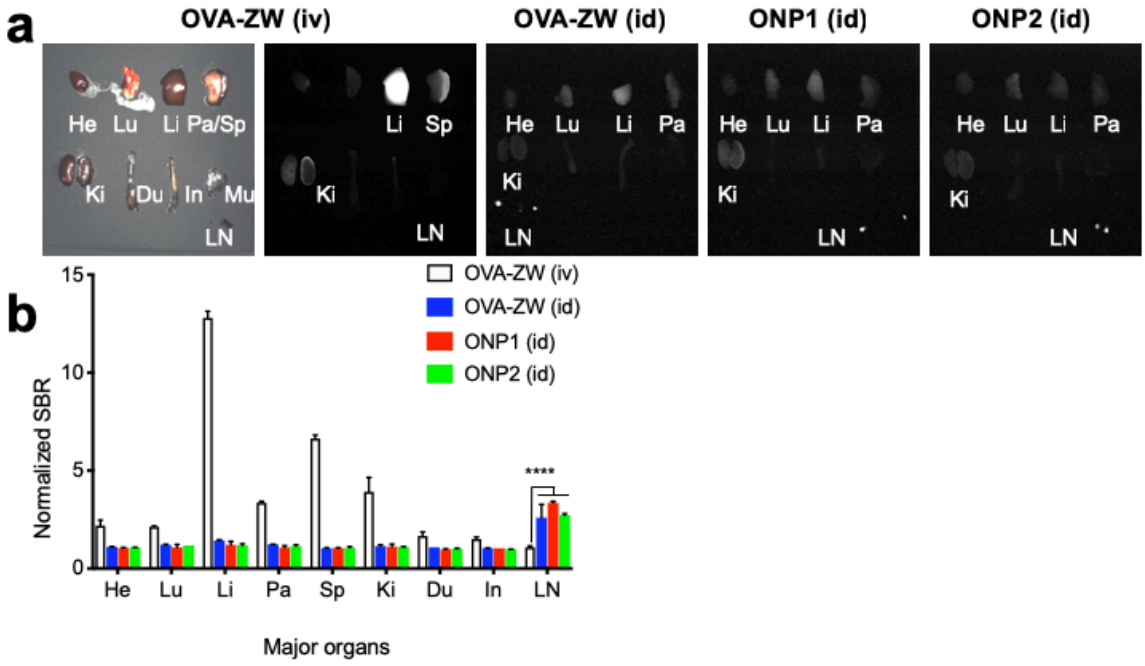

Figure 3.12. Quantitative biodistribution analysis of model vaccines. (a) Major organs, including the heart (He), lungs (Lu), liver (Li), pancreas (Pa), spleen (Sp), kidneys (Ki), duodenum (Du), intestines (In), muscles (Mu) and lymph nodes (LNs), were resected and imaged 72 h post-intradermal injection of the model vaccines. For comparison, a group of mice were injected with 10 nmol of OVA-ZW intravenously (iv) through the tail vein. (b) The SBR of major organs and LNs are compared with the fluorescence signal of muscles and normalised (n = 4, mean ± SEM). A P value of less than 0.05 was considered significant: ****P < 0.0001 by two-way ANOVA followed by Tukey's multiple comparisons test.

3.4.5 Size-dependent uptake of model vaccine by antigen presenting cells

Intradermally injected vaccines are known to be recognised by APCs, including skin-resident migDCs and cDCs within LNs or macrophages.[4,46] Size is one of the key factors affecting the kinetics of vaccine delivery to the secondary lymphoid tissue and its subsequent uptake by subpopulations of APCs.[45,46] To further validate such immunologic events in LNs, the uptake of model vaccines was analysed using flow cytometry by characterising DCs and DC subsets in the skin-draining LNs at 72 h post-injection as described previously.[4] Distinct subsets of DCs, which are identified by surface markers and their anatomical locations, have been known to be responsible for specialised immune functions.[50,51] The migDC and cDC populations were evaluated as defined by their varying MHC class II and CD11c expression and their surface markers, including Langerin, CD11b and CD103, as previously described.[4] The population of migDCs, which are dedicated to transferring antigens into LNs from the peripheral tissues, was defined by MHC class $II^{hi}CD11c^{int}$ expression and further divided into $Langerin^{-}CD11b^{-}$, $Langerin^{-}CD11b^{+}$, $Langerin^{+}CD103^{+}CD11b^{-}$ and $Langerin^{+}CD103^{-}CD11b^{+}$ Langerhans cells.[52,53] The cDCs are a bone-marrow-derived, LN-resident population and are characterised by MHC-$II^{int}CD11c^{hi}$ expression containing $CD11b^{+}$ ($CD8\alpha^{-}$) and $CD103^{+}$ ($CD8\alpha^{+}$) subsets.[2,4] The number of cDCs and their subpopulations positive for the smaller model vaccines (OVA-ZW and ONP1) were larger than those for the larger vaccine (ONP2) (Figure 3.13a–c, cDC: OVA-ZW vs. ONP2, $P = 0.0109$; ONP1 vs. ONP2, $P = 0.0354$; $CD103^{+}$ cDC, OVA-ZW vs. ONP2, $P = 0.0024$; ONP1 vs. ONP2, $P = 0.0439$), which reflects the fact that smaller vaccines directly enter the lymphatics and are taken up by cDCs.[10,45,47,54] On the other hand, the number of migDCs and their subpopulations positive for OVA-ZW and ONP1 showed a statistically marginal increase compared to those for ONP2 (Figure 3.13b,d, Figure 3.14, migDC: OVA-ZW vs. ONP2, $P = 0.0450$; ONP1 vs. ONP2, $P = 0.0182$; $CD11b^{+}Lang^{-}$ migDC: ONP1 vs. ONP2, $P = 0.0654$), which confirms the hypothesis that larger vaccines are mainly carried by migDCs only and are slowly delivered to LNs.[46,55] Interestingly, the number of cDC populations positive for ONP1 at 72 h was larger than that of ONP2 (Figure 3.13b-c), suggesting that vaccines smaller than 200 nm directly enter the lymphatics and subsequently interact with cDCs in the LNs. These results are consistent with the literature showing that smaller particles directly flow into LNs, while nanoparticles larger than 200 nm are transported by cellular mechanisms.[10,45,47,54] The number of macrophages and monocytes positive for the

vaccine at 72 h were not significantly different across the experimental groups (Figure 3.14, 3.15). These results suggest that model vaccines are associated with immune cells depending on size, and that the conjugation of the ZW fluorophores does not significantly alter the behaviour of model vaccines and their immunological events in LNs.

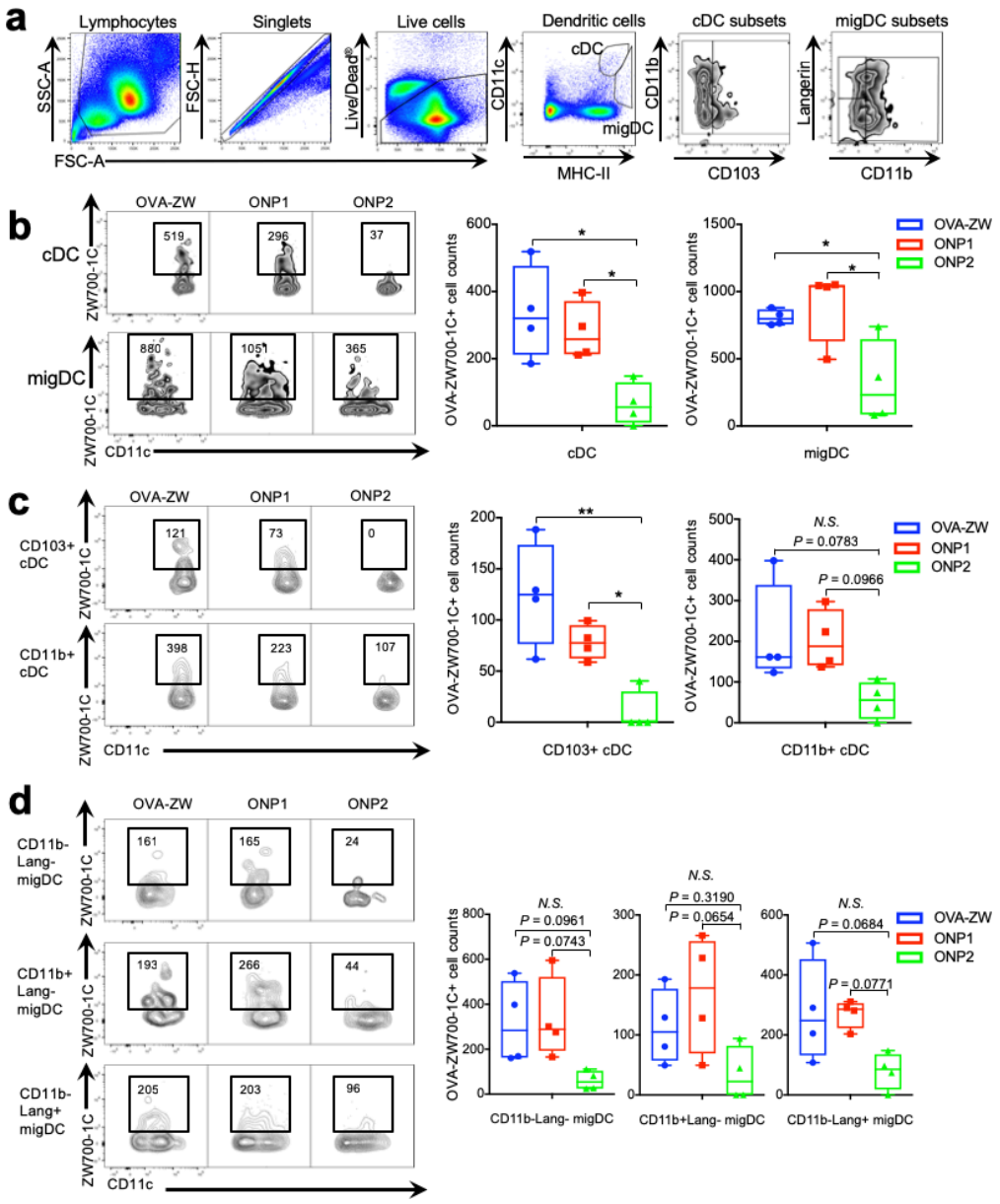

Figure 3.13. Flow cytometry analysis of vaccine uptake by DCs. Uptake of the model vaccines in DCs in the draining LNs was assessed by flow cytometry 72 h post-intradermal injection of model vaccines (n = 4, median ± 95% confidence interval). (a) Gating schematic to identify DC subsets within LNs. (b) Cell counts of OVA-ZW-positive classical LN resident DCs (cDCs) and migratory DCs (migDCs). (c) Cell counts of cDC subsets. (d) migDC subsets in the draining LNs. (b-d) A P value of less than 0.05 was considered significant: *$P < 0.05$; **$P < 0.01$, *N.S.*: not significant by one-way ANOVA followed by Tukey's multiple comparison test.

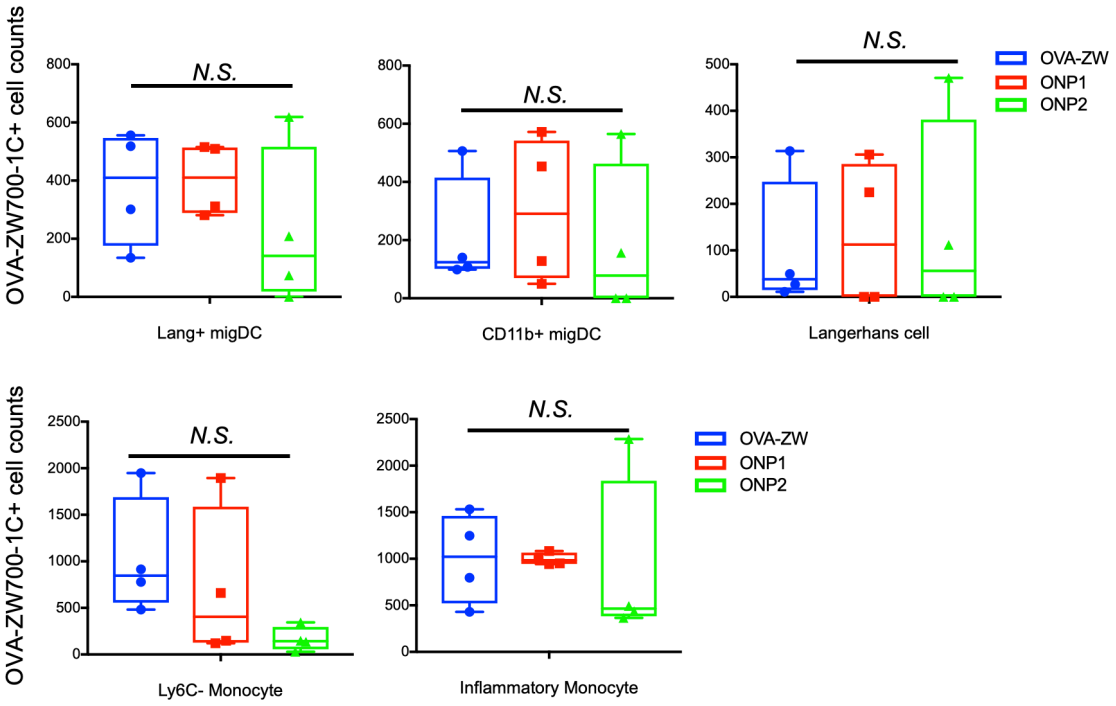

Figure 3.14. Flow cytometry analysis of vaccine uptake by APCs. Uptake of the model vaccines in DC and monocyte populations in the draining LNs was assessed by flow cytometry 72 h post-intradermal injection. Cell counts of OVA-ZW-positive migDC and monocyte subsets (n = 4, median ± 95% confidence interval). A P value of less than 0.05 was considered significant: *N.S.*, not significant by one-way ANOVA.

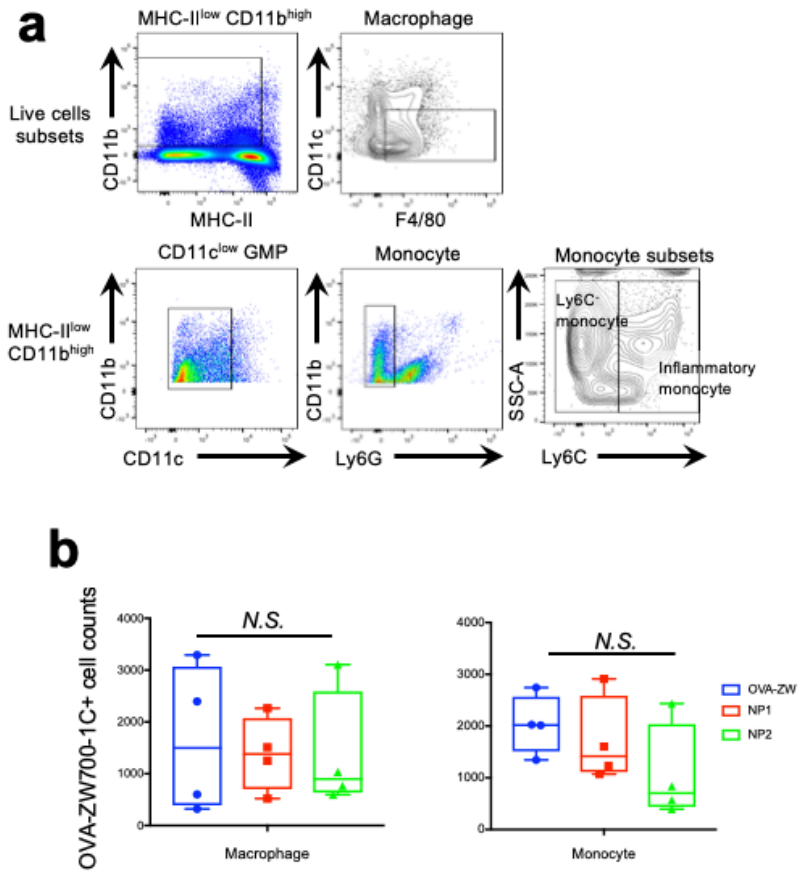

Figure 3.15. Flow cytometry analysis of vaccine uptake by macrophages and monocytes. Uptake of the conjugated vaccine in macrophage and monocyte populations in the draining LNs was assessed by flow cytometry 72 h post-intradermal injection. (a) Gating schematic to identify macrophage and monocyte populations within LNs. (b) Cell counts of OVA-ZW-positive macrophage and monocyte populations within LNs (n = 4, median ± 95% confidence interval). A P value of less than 0.05 was considered significant: *N.S.*, not significant by one-way ANOVA.

3.4.6 Size-dependent distribution of model vaccines in lymph nodes

Since APCs actively interact with the model vaccines depending on their size, histological analysis of LNs was performed to evaluate the spatial distribution of model vaccines. The OVA-ZW fluorescence was associated with cells and was predominantly distributed along the subcapsular sinus in the periphery of popliteal LNs (Figure 3.16a-b, g), which suggests that the small antigen arrived through afferent lymphatic vessels via lymphatic drainage and was captured by APCs along the subcapsular sinus.[10,56] The fluorescence associated with ONP1 was detected in the cells located in both the subcapsular sinus and outer cortex areas, while the signal from ONP2 was detected only in the outer cortex areas (Figure 3.16c–g). This result confirms that larger vaccines (ONP2) are transported by migDCs from the skin, while smaller vaccines (OVA-ZW and ONP1) are associated with both lymphatic drainage and cellular mechanisms. This size-dependent distribution of model vaccines in the draining LNs further confirms that the conjugation of the ZW fluorophore does not significantly alter the interactions between immune cells and vaccines, and that the fluorescence signals from ZW reflect the biodistribution of model vaccines.

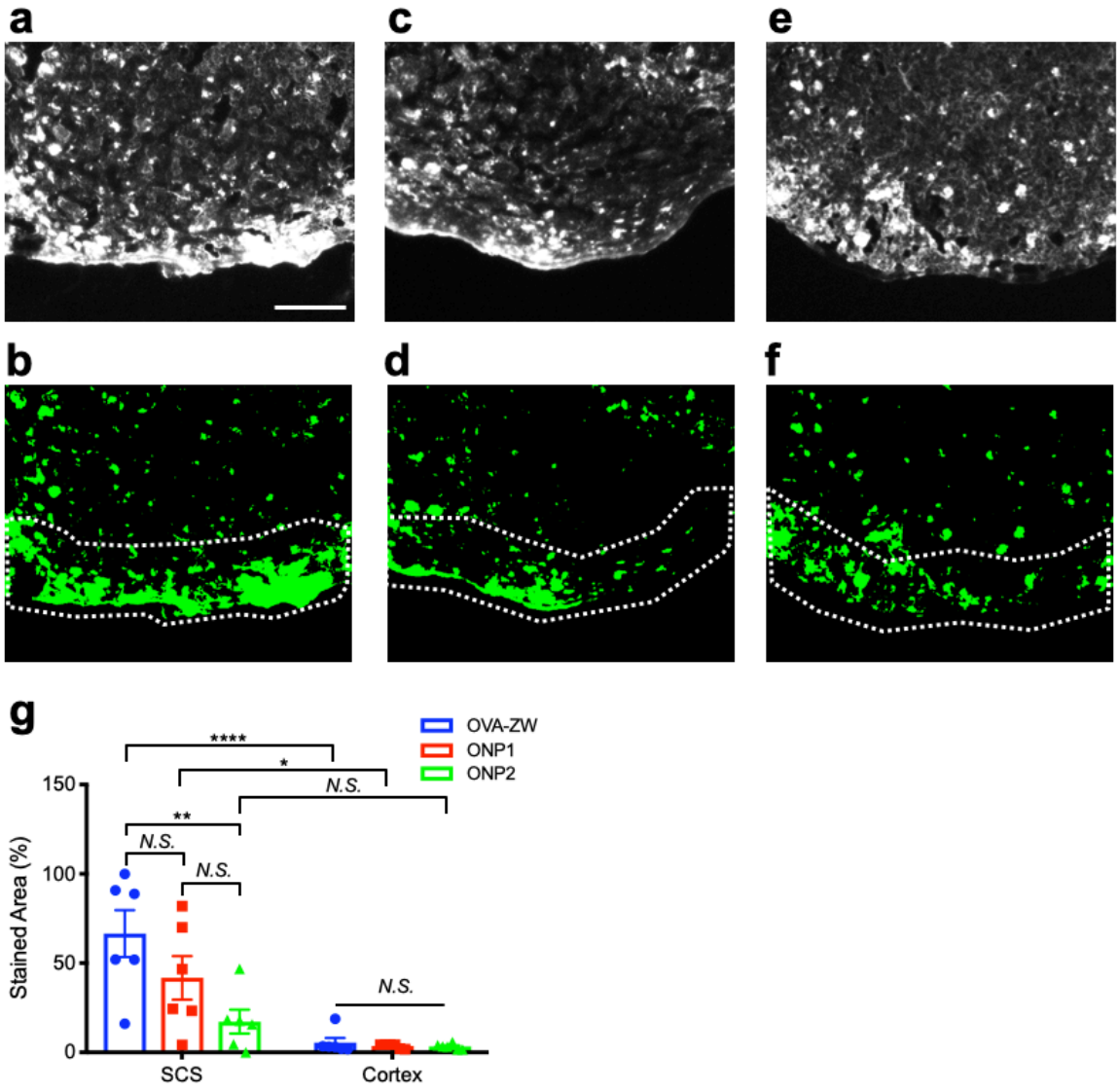

Figure 3.16. Histological analysis of vaccine uptake by APCs in the draining LNs. Uptake of the model vaccines in APCs was assessed by histology 72 h post-intradermal injection. (a–c) Representative fluorescence images. (d–f) Binarized images of LNs: (a,b) OVA-ZW, (c,d) ONP1, (e,f) ONP2. Dotted lines depict capsular and subcapsular sinus (SCS) of LNs. Scale bar = 100 µm. (g) Quantitative analysis of areas positive for fluorescence in the SCS and in the cortex of LNs ($n = 6$, mean ± SEM.). A P value of less than 0.05 was considered significant: *$P < 0.05$; **$P < 0.01$; ****$P < 0.0001$; *N.S.*, not significant by two-way ANOVA followed by Tukey's multiple comparison test.

3.5 Discussion

Although most clinical vaccines are given intramuscularly, evidence suggests that intradermal delivery is more effective for some vaccines,[57–60] as the skin is enriched with immune cells and is thus considered as an attractive site for vaccine administration.[61] However, this vaccination route is not fully explored, and consequently only one clinical intradermal vaccine has been licensed to date.[62] The main modes of action proposed for trafficking intradermally administered vaccine antigens are as follows: (1) the injected vaccine antigen is recognised and transported by immune cells, including APCs, followed by migration from the injection site to LNs.[63,64] (2) Alternatively, lymphatics in the skin are able to transport the intradermally injected vaccine antigen into skin-draining LNs.[45,46] Thus, the difficulty in understanding the pharmacokinetics of vaccines is mainly attributable to the complex interactions among these factors.

To understand the immunomodulation of cells, metabolic glycoengineering has been applied to label DC cell membranes with chemical probes.[65–67] Wang *et al*. established a DC labelling material that is capable of subsequent tracking of the destination and observed $CD8^+$ T cell responses.[68] This methodology provides a powerful tool to observe the destination of APCs; however, it allows for analysis at only one time point, since it is invasive.

This study has, for the first time, successfully established a reliable platform for the quantitative assessment of biodistribution and kinetics using NIR fluorescence imaging after intradermal injection of model vaccines. The size of fluorescent nanoparticles was assessed by DLS, which is a method as reliable as TEM, SEM and AFM.[28] As for imaging, compared to the conventional methodology of using radioisotopes, optical imaging represents a simple, straightforward and reliable tool for determining the biodistribution of vaccines in real time. The bioconjugation of NIR fluorophores with vaccine proteins can be completed within a few hours by the NHS ester chemistry. This technology can therefore be applied for labelling a wide range of biological molecules without specific requirements for conjugation. In addition, the use of zwitterionic NIR fluorophores offers unique features that improve imaging performance over the conventional visible fluorophores. First, zwitterionic NIR fluorophores show minimal interactions with biological tissues and do not alter the vaccine's interactions with immune cells or other tissues. Second, since zwitterionic NIR fluorophores can achieve an ultralow background with a high SBR, the injection dose needed to visualise conjugated molecules in the body is significantly lower than in other conventional fluorophores. The

conventional organic dyes within the visual wavelength tend to have high background signals due to tissue autofluorescence and nonspecific binding, resulting in a low SBR. Third, the chemical conjugation generally alters the physicochemical property of the bioconjugate because of the size, charges and hydrophobicity of fluorophores, which affects its immunogenicity, functions and biological interactions with surrounding tissues and immune cells.[69–72] For example, it has been well established that fluorescence tagging on antibodies affects the targeting affinity of the antibodies to the specific epitope,[69,71] and that the surface charge of fluorophores impacts the interactions between the labelled protein and the cells.[70] In this study, the size-dependent uptake of model vaccines in migDC and cDC as demonstrated by flow cytometry and histology was consistent with the literature, indicating that the chemical conjugation did not affect antigen recognition of model vaccines by APCs, and that the use of a small amount of ZW800-1C would minimise the confounding impacts of a fluorophore on the function of the biomolecule to be conjugated.

As was shown, the NIR imaging system has great advantages for live imaging; however, there is a limitation regarding signal detection. The detectivity of fluorescent signals is dependent on three factors: (1) the brightness of NIR fluorophores, (2) the property of the imaging sensor, and (3) the signal depth in tissues.

First, brightness is an essential factor of fluorophores. The efficacy of emission is defined as QY. QY is a unique value for a fluorophore, calculated by the number of emitted photons divided by the number of received photons by the fluorophore. ZW800-1C has 23.9% of QY, whereas Cy5 has 30%. This indicates that Cy5 has a brighter signal than ZW800-1C under the same excitation condition. In fact, Cy5 showed a higher SBR in LNs than ZW800-1C at 1 h after intradermal injection (Figure 3.11). After a while, the SBR decreased because Cy5 raised the background signal as well, resulting in a lower SBR than in ZW800-1C after 6 h. In addition, the depth of the target organ in tissue is deeply involved in the visibility of fluorescent signals. The penetration depth of the signal from the NIR fluorophore around the 800-nm range is approximately 8 mm[73] because skin reflects, absorbs and scatters both emission and excitation light. Meanwhile, the range between 1000 nm and 1400 nm is called the NIR-II region. This is because light in the NIR-II region has the properties of less reflection (reflectance of 0.12 at 800 nm, 0.07 at 1300 nm), less absorption (absorption coefficient of 0.5 at 800 nm, 0.3 at 1300 nm) and less scattering (scattering coefficient of 2.6 at 800 nm, 1.2 at 1300 nm).[74] Together with these features, novel fluorophores in the NIR-II region are intensively investigated for future intraoperative fluorescence imaging.[75,76]

Second, the signal detectivity of the imaging sensor is critical to the quality of images. The new imaging system can visualise ZW800-1C at a concentration of more than 50 nM (Figure 3.8); however, the signal cannot be seen at a concentration of less than 50 nM. Introducing the SBR was intended to quantify undistinguishable fluorescent signals over time, which helped us to observe signals at less than 50 nM (Figure 3.9). In order to observe fluorescence at a much lower concentration, we could apply a photon-counting camera.[77] Tetrault *et al*. demonstrated that the photon-counting camera (SPC3, Micro Photon. Devices, Italy) improved the sensitivity and maintained the full dynamic range of exposure time compared with a KFLARE system equipped with conventional CCD sensors.[77] As such, the photon-counting camera could be an alternative instrument for observing low signals.

Third, the spatial resolution in the z-axis of the KFLARE system was poor, since the images were captured only from the top of the surgical field, yielding only 2D information. For live imaging, multiple cameras could be placed over the surgical field to compose 3D images. A Da Vinci Vision system (Intuitive Surgical, US) equipped with multiple cameras can realise a real-time, image-guided surgery system with an endoscopic interface. Another solution is to combine NIR imaging with another medical imaging system, such as positron emission tomography (PET). PET has high detectivity in deep tissue; however, its spatial resolution is very limited. By combining NIR imaging with PET imaging, visualising deeper tissue with a clear signal could be achieved. Zhu *et al.* conjugated ^{64}Cu, arginine-glycine-aspartic acid and zwitterionic fluorophores to image a tumour in a mouse model.[78] Considering that the penetration depth of positrons is over one meter, it would be possible to apply such a fluorophore to visualise the detailed structure of deep tissue, which NIR alone could not show. Together with these novel technologies, NIR imaging could be capable of overcoming the current limitations.

3.6 Summary

NIR fluorescence imaging combined with zwitterionic fluorophores represents a feasible and reliable methodology to track the transportation of vaccines by APCs and to determine the biodistribution and kinetics of vaccine *in vivo*. Such a platform would offer a powerful tool for optimising the dose, formulation and injection route of clinical and preclinical vaccines, as well as for investigating mechanisms of novel laser adjuvant technology. Yet, the establishment of microscopic approaches to reveal hidden facets of photobiomodulation is desired. In particular, finding an appropriate photoreceptor is key to achieving a deeper understanding of photobiomodulation.

Reference

1. Kashiwagi, S., Brauns, T., Gelfand, J. & Poznansky, M. C. Laser vaccine adjuvants: History, progress, and potential. *Hum. Vaccines Immunother.* **10**, 1892–1907 (2014).
2. Kimizuka, Y. *et al.* Brief Exposure of Skin to Near-Infrared Laser Modulates Mast Cell Function and Augments the Immune Response. *J. Immunol.* ji1701687 (2018) doi:10.4049/jimmunol.1701687.
3. Kashiwagi, S. *et al.* Near-infrared laser adjuvant for influenza vaccine. *PLoS One* **8**, (2013).
4. Morse, K. *et al.* Near-Infrared 1064 nm Laser Modulates Migratory Dendritic Cells To Augment the Immune Response to Intradermal Influenza Vaccine. *J. Immunol.* ji1601873 (2017) doi:10.4049/jimmunol.1601873.
5. Kimizuka, Y. *et al.* Semiconductor diode laser device adjuvanting intradermal vaccine. *Vaccine* **35**, 2404–2412 (2017).
6. Johansen, P., Mohanan, D., Martínez-Gómez, J. M., Kündig, T. M. & Gander, B. Lympho-geographical concepts in vaccine delivery. *J. Control. Release* **148**, 56–62 (2010).
7. d'Onofrio, A., Manfredi, P. & Salinelli, E. Vaccinating behaviour, information, and the dynamics of SIR vaccine preventable diseases. *Theor. Popul. Biol.* **71**, 301–317 (2007).
8. Arakane, R. *et al.* Superior immunogenicity profile of the new intradermal influenza vaccine compared to the standard subcutaneous vaccine in subjects 65 years and older: A randomized controlled phase III study. *Vaccine* **33**, 6650–6658 (2015).
9. Ma, G.-H. *et al.* Surface charge affects cellular uptake and intracellular trafficking of chitosan-based nanoparticles. *Biomacromolecules* **12**, 2440–2446 (2011).
10. Manolova, V. *et al.* Nanoparticles target distinct dendritic cell populations according to their size. *Eur. J. Immunol.* **38**, 1404–1413 (2008).
11. Kang, S. *et al.* Effects of gold nanoparticle-based vaccine size on lymph node delivery and cytotoxic T-lymphocyte responses. *J. Control. Release* **256**, 56–67 (2017).
12. Bachmann, M. F. & Jennings, G. T. Vaccine delivery: A matter of size, geometry, kinetics and molecular patterns. *Nat. Rev. Immunol.* **10**, 787–796 (2010).
13. Hyun, H. *et al.* Central C-C bonding increases optical and chemical stability of NIR fluorophores. *RSC Adv.* **4**, 58762–58768 (2014).
14. Hyun, H. *et al.* Structure-inherent targeting of near-infrared fluorophores for parathyroid and thyroid gland imaging. *Nat. Med.* **21**, 192–197 (2015).
15. Hyun, H. *et al.* Cartilage-Specific Near-Infrared Fluorophores for Biomedical Imaging. *Angew. Chemie - Int. Ed.* **54**, 8648–8652 (2015).
16. Park, M. H. *et al.* Prototype nerve-specific near-infrared fluorophores. *Theranostics* **4**, 823–833 (2014).
17. Lee, J. H., Park, G., Hong, G. H., Choi, J. & Choi, H. S. Design considerations for targeted optical contrast agents. *Quant. Imaging Med. Surg.* **2**, 266–73 (2012).
18. Owens, E. A. *et al.* Near-Infrared Illumination of Native Tissues for Image-Guided Surgery. *J. Med. Chem.* **59**, 5311–5323 (2016).
19. Owens, E. A., Henary, M., El Fakhri, G. & Choi, H. S. Tissue-Specific Near-Infrared Fluorescence

Imaging. *Acc. Chem. Res.* **49**, 1731–1740 (2016).

20. Hu, S. *et al.* Real-Time Imaging of Brain Tumor for Image-Guided Surgery. *Adv. Healthc. Mater.* **1800066**, 1–15 (2018).
21. Kang, H. *et al.* Renal Clearable Organic Nanocarriers for Bioimaging and Drug Delivery. *Adv. Mater.* 8162–8168 (2016) doi:10.1002/adma.201601101.
22. Kim, K. S. *et al.* Bioimaging of hyaluronate-interferon α conjugates using a non-interfering zwitterionic fluorophore. *Biomacromolecules* **16**, 3054–3061 (2015).
23. Chung, J. E. *et al.* Self-assembled micellar nanocomplexes comprising green tea catechin derivatives and protein drugs for cancer therapy. *Nat. Nanotechnol.* **9**, 907–912 (2014).
24. Henderson, R. The Potential and Limitations of Neutrons, Electrons and X-Rays for Atomic Resolution Microscopy of Unstained Biological Molecules. *Q. Rev. Biophys.* **28**, 171–193 (1995).
25. Malhotra, A. *et al.* Escherichia coli 70 S ribosome at 15 Å resolution by cryo-electron microscopy: Localization of fMet-tRNA(f)(Met) and fitting of L1 protein. *J. Mol. Biol.* **280**, 103–116 (1998).
26. Jans, H., Liu, X., Austin, L., Maes, G. & Huo, Q. Dynamic light scattering as a powerful tool for gold nanoparticle bioconjugation and biomolecular binding studies. *Anal. Chem.* **81**, 9425–9432 (2009).
27. Jitkang, L., Pin, Y. S., Xin, C. H. & Chun, L. S. Characterization of magnetic nanoparticle by dynamic light scattering. *Nanoscale Res. Lett.* **8**, 308–381 (2013).
28. Hoo, C. M., Starostin, N., West, P. & Mecartney, M. L. A comparison of atomic force microscopy (AFM) and dynamic light scattering (DLS) methods to characterize nanoparticle size distributions. *J. Nanoparticle Res.* **10**, 89–96 (2008).
29. Shapiro, H. M. Multistation multiparameter flow cytometry: A critical review and rationale. *Cytometry* **3**, 227–243 (1983).
30. Herzenberg, L. A. *et al.* The history and future of the Fluorescence Activated Cell Sorter and flow cytometry: A view from Stanford. *Clin. Chem.* **48**, 1819–1827 (2002).
31. Nakano, O. *et al.* Proliferative activity of intratumoral CD8+ T-lymphocytes as a prognostic factor in human renal cell carcinoma: Clinicopathologic demonstration of antitumor immunity. *Cancer Res.* **61**, 5132–5136 (2001).
32. Gabrielson, A. *et al.* Intratumoral CD3 and CD8 T-cell densities associated with relapse-free survival in HCC. *Cancer Immunol. Res.* **4**, 419–430 (2016).
33. Sharma, P. *et al.* CD8 tumor-infiltrating lymphocytes are predictive of survival in muscle-invasive urothelial carcinoma. *Proc. Natl. Acad. Sci. U. S. A.* **104**, 3967–3972 (2007).
34. Van Der Sluis, T. C. *et al.* Therapeutic peptide vaccine-induced CD8 T cells strongly modulate intratumoral macrophages required for tumor regression. *Cancer Immunol. Res.* **3**, 1042–1051 (2015).
35. Ruffell, B. *et al.* Macrophage IL-10 Blocks CD8+ T Cell-Dependent Responses to Chemotherapy by Suppressing IL-12 Expression in Intratumoral Dendritic Cells. *Cancer Cell* **26**, 623–637 (2014).
36. Kang, H. *et al.* Renal Clearable Organic Nanocarriers for Bioimaging and Drug Delivery. *Adv. Mater.* **28**, 8162–8168 (2016).
37. Choi, H. S. *et al.* Targeted zwitterionic near-infrared fluorophores for improved optical imaging. *Nat. Biotechnol.* **31**, 148–153 (2013).
38. Hutteman, M. *et al.* Clinical translation of ex vivo sentinel lymph node mapping for colorectal cancer

using invisible near-infrared fluorescence light. *Ann. Surg. Oncol.* **18**, 1006–1014 (2011).

39. Tanaka, E., Choi, H. S., Fujii, H., Bawendi, M. G. & Frangioni, J. V. Image-guided oncologic surgery using invisible light: Completed pre-clinical development for sentinel lymph node mapping. *Ann. Surg. Oncol.* **13**, 1671–1681 (2006).
40. Yang, A. W., Cho, S. U., Jeong, M. Y. & Choi, H. S. NIR Fluorescence Imaging Systems with Optical Packaging Technology. *J. Microelectron. Packag. Soc.* **21**, 25–31 (2014).
41. Hyun, H. *et al.* 700-nm Zwitterionic Near-Infrared Fluorophores for Dual-Channel Image-Guided Surgery. *Mol. Imaging Biol.* **18**, 52–61 (2016).
42. Turner, V. M. & Mabbott, N. A. Structural and functional changes to lymph nodes in ageing mice. *Immunology* **151**, 239–247 (2017).
43. Choi, H. S. *et al.* Synthesis and in vivo fate of zwitterionic near-infrared fluorophores. *Angew. Chemie - Int. Ed.* **50**, 6258–6263 (2011).
44. Choi, H. S. *et al.* Targeted zwitterionic near-infrared fluorophores for improved optical imaging. *Nat. Biotechnol.* **31**, 148–153 (2013).
45. Moyer, T. J., Zmolek, A. C. & Irvine, D. J. Beyond antigens and adjuvants: Formulating future vaccines. *J. Clin. Invest.* **126**, 799–808 (2016).
46. Tozuka, M. *et al.* Efficient antigen delivery to the draining lymph nodes is a key component in the immunogenic pathway of the intradermal vaccine. *J. Dermatol. Sci.* **82**, 38–45 (2016).
47. Reddy, S. T., Rehor, A., Schmoekel, H. G., Hubbell, J. A. & Swartz, M. A. In vivo targeting of dendritic cells in lymph nodes with poly(propylene sulfide) nanoparticles. *J. Control. Release* **112**, 26–34 (2006).
48. Schurich, A. *et al.* Distinct kinetics and dynamics of cross-presentation in liver sinusoidal endothelial cells compared to dendritic cells. *Hepatology* **50**, 909–919 (2009).
49. Pooley, J. L., Heath, W. R. & Shortman, K. Cutting Edge: Intravenous Soluble Antigen Is Presented to CD4 T Cells by CD8 − Dendritic Cells, but Cross-Presented to CD8 T Cells by CD8 + Dendritic Cells . *J. Immunol.* **166**, 5327–5330 (2001).
50. Schlitzer, A., McGovern, N. & Ginhoux, F. Dendritic cells and monocyte-derived cells: Two complementary and integrated functional systems. *Semin. Cell Dev. Biol.* **41**, 9–22 (2015).
51. Merad, M., Sathe, P., Helft, J., Miller, J. & Mortha, A. The Dendritic Cell Lineage: Ontogeny and Function of Dendritic Cells and Their Subsets in the Steady State and the Inflamed Setting. *Annu. Rev. Immunol.* **31**, 563–604 (2013).
52. Malissen, B., Tamoutounour, S. & Henri, S. The origins and functions of dendritic cells and macrophages in the skin. *Nat. Rev. Immunol.* **14**, 417–428 (2014).
53. Henriksen-Lacey, M. *et al.* Liposomal cationic charge and antigen adsorption are important properties for the efficient deposition of antigen at the injection site and ability of the vaccine to induce a CMI response. *J. Control. Release* **145**, 102–108 (2010).
54. Fifis, T. *et al.* Size-Dependent Immunogenicity: Therapeutic and Protective Properties of Nano-Vaccines against Tumors. *J. Immunol.* **173**, 3148–3154 (2004).
55. Itano, A. A. *et al.* Distinct dendritic cell populations sequentially present antigen to CD4 T cells and stimulate different aspects of cell-mediated immunity. *Immunity* **19**, 47–57 (2003).
56. Cubas, R. *et al.* VLP Lymphatic Trafficking and Immune Response. *J. Immunother.* **32**, 118–128

(2010).

57. Teunissen, M. B. M. & Zehrung, D. Cutaneous vaccination - Protective immunization is just a skin-deep step away. *Vaccine* **33**, 4659–4662 (2015).
58. Sticchi, L., Alberti, M., Alicino, C. & Crovari, P. The intradermal vaccination: Past experiences and current perspectives. *J. Prev. Med. Hyg.* **51**, 7–14 (2010).
59. Fehres, C. M., Garcia-Vallejo, J. J., Unger, W. W. J. & van Kooyk, Y. Skin-resident antigen-presenting cells: Instruction manual for vaccine development. *Front. Immunol.* **4**, 1–8 (2013).
60. Lambert, P. H. & Laurent, P. E. Intradermal vaccine delivery: Will new delivery systems transform vaccine administration? *Vaccine* **26**, 3197–3208 (2008).
61. Nestle, F. O., Di Meglio, P., Qin, J. Z. & Nickoloff, B. J. Skin immune sentinels in health and disease. *Nat. Rev. Immunol.* **9**, 679–691 (2009).
62. Ansaldi, F., de Florentiis, D., Durando, P. & Icardi, G. Fluzone(R) Intradermal vaccine: a promising new chance to increase the acceptability of influenza vaccination in adults. *Expert Rev. Vaccines* **11**, 17–25 (2012).
63. Worbs, T., Hammerschmidt, S. I. & Förster, R. Dendritic cell migration in health and disease. *Nat. Rev. Immunol.* **17**, 30–48 (2017).
64. Salomon, B., Cohen, J. L., Masurier, C. & Klatzmann, D. Three populations of mouse lymph node dendritic cells with different origins and dynamics. *J. Immunol.* **160**, 708–17 (1998).
65. Laughlin, S. T. *et al.* Metabolic Labeling of Glycans with Azido Sugars for Visualization and Glycoproteomics. *Methods Enzymol.* **415**, 230–250 (2006).
66. Lauehlin, S. T. & Bertozzi, C. R. Metabolic labeling of glycans with azido sugars and subsequent glycan-profiling and visualization via staudinger ligation. *Nat. Protoc.* **2**, 2930–2944 (2007).
67. Changa, P. V. *et al.* Copper-free click chemistry in living animals. *Proc. Natl. Acad. Sci. U. S. A.* **107**, 1821–1826 (2010).
68. Wang, H. *et al.* Metabolic labeling and targeted modulation of dendritic cells. *Nat. Mater.* doi:10.1038/s41563-020-0680-1.
69. Szabó, Á. *et al.* The Effect of Fluorophore Conjugation on Antibody Affinity and the Photophysical Properties of Dyes. *Biophys. J.* **114**, 688–700 (2018).
70. Yin, L. *et al.* How does fluorescent labeling affect the binding kinetics of proteins with intact cells? *Biosens. Bioelectron.* **66**, 412–416 (2015).
71. Vira, S., Mekhedov, E., Humphrey, G. & Blank, P. S. Fluorescent-labeled antibodies: Balancing functionality and degree of labeling. *Anal. Biochem.* **402**, 146–150 (2010).
72. Hayashi-Takanaka, Y., Stasevich, T. J., Kurumizaka, H., Nozaki, N. & Kimura, H. Evaluation of chemical fluorescent dyes as a protein conjugation partner for live cell imaging. *PLoS One* **9**, (2014).
73. Bordo, M. W. *et al.* Real-time near-infrared fluorescence imaging using cRGD- ZW800-1 for intraoperative visualization of multiple cancer types. **8**, 21054–21066 (2017).
74. Mori, Y. Optical properties. *Powder Technol. Fundam. Part. Powder Beds, Part. Gener.* **2**, 115–124 (2006).
75. Antaris, A. L. *et al.* A small-molecule dye for NIR-II imaging. *Nat. Mater.* **15**, 235–242 (2016).
76. Hong, G. *et al.* Multifunctional in vivo vascular imaging using near-infrared II fluorescence. *Nat. Med.*

18, 1841–1846 (2012).

77. Tetrault, M.-A. *et al.* Path to a real-time, full dynamic range and high sensitivity quantitative optical imaging system for surgery assistance: the photon counting camera. *MGH Clin. Res. Day 16th Annu. Celebr. Clin. Res.* 233 (2018).

78. Zhu, L. *et al.* Dynamic PET and optical imaging and compartment modeling using a Dual-labeled cyclic RGD peptide probe. *Theranostics* **2**, 746–756 (2012).

Chapter 4

Exploring NIR photoreceptors using density functional theory

Many studies have been reporting on photobiomodulation in the context of medicine; however, no study so far has revealed the essential elements of NIR receptor molecules. This chapter describes the theoretical methodology used to explore NIR photoreceptor molecule candidates using DFT, as well as the action of the candidate molecule discovered with DFT.

4.1 Introduction

The primary goal was to reveal the molecular mechanism of the NIR laser adjuvant effect, for which our current knowledge is limited.[1–4] Although some have recognised the effect of photobiomodulation as a medical effect, the consequent mechanisms of light initiated by photoreceptors and the initiation of intracellular signalling are poorly understood, especially the NIR region of light. For example, rhodopsin is a membrane protein family of G protein-coupled receptors (GPCRs) that exists in retina cells and recognises light. Rhodopsin is classified into type 1 and type 2. A recent study in 2019 discovered and specified the structure of another type of rhodopsin called heliorhodopsin.[5] Consequently, many studies have been eager to reveal the molecular mechanisms activated by light. Furthermore, the current study aimed to discover a photoreceptor outside of the eyeballs. Here, a theoretical methodology to calculate an absorbance spectrum of small molecules was performed by using TDDFT to explore the NIR laser adjuvant response.

Hamblin *et al*. summarised the effects of photobiomodulation by NIR.[6–8] These studies focused on the generation of ATP, mitochondrial ROS and the subsequent intracellular molecules. However, considering that the reported wavelengths were limited to between 600 nm and 1000 nm, the mechanism of LLLT is not yet fully understood. Concerning mechanisms, it is widely recognised that the benefit of NIR laser light or LLLT is mediated by mitochondrial signalling, including ROS.[7–16] COX in the ETC in the mitochondria has been considered as the primary source of mitochondrial ROS.[15] The mode of action of ROS generation in response to NIR light involves the modulation of interactions between COX and gaseous monoxide, including carbon monoxide (CO)[15] and nitric oxide (NO),[17] in the ETC. Both CO and NO are able to bind to the oxygen-binding site in competition with oxygen and act as a reversible inhibitor of COX at low concentrations, diverting oxygen into ROS formation.[15,18–20] NIR light has been shown to alter cell metabolism, as it displaces these gas molecules on histidine in COX proteins,[21] resulting in the generation of ROS and the activation of ROS-mediated retrograde signalling via FOXOs, NF-κB, AP-1 and Myc.[15,16] In addition, superoxide dismutase 1 (SOD1) is also associated with mitochondrial ROS reduction.[22,23] Dysfunction of SOD1 leads to many diseases, including neural disorders and cancer.[24–27] Thus, mitochondrial ETC, COX and SOD1 are prime candidates for NIR photoreceptors.[16,28]

4.2 Methodologies

First, in order to understand the DFT method, the difference between function and functional should be clarified. A function is an equation in which the input is a variable. In contrast, the term ‘functional’ refers to an equation in which the input itself is a function. For example,

$$y = f(x) \qquad (1)$$

is a function which has a variable of x. On the other hand,

$$I[f] = \int_a^b f(x)\,dx \qquad (2)$$

is called functional.

DFT has been used in most branches of chemistry for the past 30 years.[29] The theory states that every physical quantity or property of a system is a functional determined by the identity of the electron density of the ground state. The basic theory of DFT is built on the Schrödinger equation:

$$\hat{H}\,\psi(\boldsymbol{r}) \;=\; E\,\psi(\boldsymbol{r}) \qquad (3)$$

$$\hat{H} = -\frac{\hbar}{2m}\,\boldsymbol{\nabla}^2 + \boldsymbol{V}(\boldsymbol{r}), \qquad (4)$$

where

$$\hbar = \frac{h}{2\pi}, \qquad (5)$$

where $\psi(\boldsymbol{r})$ is the three-dimensional wave function, E is the energy, h is Plank's constant, m is the mass of the particle, $\boldsymbol{\nabla}^2$ is the Laplacian operator, and $\boldsymbol{V}(\boldsymbol{r})$ is the potential energy influencing the particle.

The problem in the Schrödinger equation is that the larger the molecular atom of interest, the higher the dimension of the vector $\boldsymbol{r}$ representing the position of the particle. For example, the Schrödinger equation for two electrons in a helium atom is described as:

$$\left[-\frac{1}{2}\,\boldsymbol{\nabla}_{\boldsymbol{1}}^2 \;-\frac{1}{2}\,\boldsymbol{\nabla}_{\boldsymbol{2}}^2 \;-\frac{2}{\boldsymbol{r_1}} \;-\frac{2}{\boldsymbol{r_2}} - \frac{1}{|\boldsymbol{r_1} - \boldsymbol{r_2}|}\right]\psi(\boldsymbol{r_1}, \boldsymbol{r_2}) = \; E\,\psi(\boldsymbol{r_1}, \boldsymbol{r_2}). \qquad (6)$$

Equation (6) includes two different Euclidean distances, resulting in six dimensional variables. In order to simplify the calculation applicable in large molecules, two approximation options apply: the Hartree-Fock method and the Kohn-Sham method.[30,31] The Hartree-Fock method is the idea that the wave function $\psi(\boldsymbol{r})$ of an N electron system consists of an infinite number of combinations of a matrix formula consisting of arbitrary N one-electron orbitals, which is described by

$$\psi(\boldsymbol{r_1}, \boldsymbol{r_2}, \ldots, \boldsymbol{r_N}) \;=\; \|\varphi_1(\boldsymbol{r_1}), \varphi_2(\boldsymbol{r_2}), \ldots, \varphi_N(\boldsymbol{r_N})\,\|. \qquad (7)$$

This matrix formula is called the Slater determinant.

On the other hand, the Kohn-Sham method is based on the Hohenberg-Kohn theorems as follows:

Theory 1. The ground state energy E is uniquely determined by an electron density ρ.

$$\psi(\boldsymbol{r_1}, \boldsymbol{r_2}, \dots, \boldsymbol{r_N}) = \rho(\boldsymbol{r}) \qquad (8)$$

Theory 2. The ground state energy $E_G[\rho]$ gives a minimum value when ρ becomes the true ground state $\rho_0(\boldsymbol{r})$ for the one-electron density $\rho(\boldsymbol{r})$ normalised to the number of electrons N.

$$E_G[\rho] \geq E_G[\rho_0] \qquad (9)$$

$$\int \rho(\boldsymbol{r}) d\boldsymbol{r} = N \qquad (10)$$

Based on the Hohenberg-Kohn theorems and another approximation method called Levy's method, Equation (3) can be described as:

$$\left[-\frac{1}{2}\boldsymbol{\nabla}^2 + \upsilon_{eff}(\boldsymbol{r})\right] \rho_i(\boldsymbol{r}) = \varepsilon_i \rho_i(\boldsymbol{r}) \qquad (11)$$

$$\upsilon_{eff}(\boldsymbol{r}) = \upsilon_{ext}(\boldsymbol{r}) + \upsilon_{Hartree}(\boldsymbol{r}) + \upsilon_{xc}(\boldsymbol{r}), \qquad (12)$$

where ρ_i is the electron density at an individual orbital, ε_i is the energy at an individual orbital, $\upsilon_{ext}(\boldsymbol{r})$ is the kinetic energy, $\upsilon_{Hartree}(\boldsymbol{r})$ is the exchange correlation energy based on classical mechanics, also called Hartree energy, and $\upsilon_{xc}(\boldsymbol{r})$ is the exchange correlation energy based on quantum mechanics. Together with the self-consistent field method,[32,33] the total energy E is described as:

$$E[\rho] = \sum_{i=1}^{N} \varepsilon_i - \frac{1}{2}\int \rho(\boldsymbol{r}) V_{Hartree}(\boldsymbol{r}) d\boldsymbol{r} + \boldsymbol{E_{xc}}[\rho] - \int \rho(\boldsymbol{r}) \upsilon_{xc}(\boldsymbol{r}) d\boldsymbol{r}. \qquad (13)$$

However, since there is no methodology yet to define the functionals of $V_{ext}(\boldsymbol{r})$ and $V_{xc}(\boldsymbol{r})$, it is necessary to apply further approximation methods. The best approximation method remains unknown; therefore, an operator must choose one out of several methods: local density approximation (LDA), local spin density approximation (LSDA), generalised gradient approximation (GGA), meta-GGA, hybrid-GGA, and so on. Three-parameterised Becke-Lee-Yang-Parr (B3LYP) is also an approximation approach used to define the unveiled functionals reported by Axel D. Becke,[34] and it is now the most commonly used method in DFT calculation. B3LYP is capable of accuracy in predicting molecular structures.[35] For DFT calculation, it is important to choose an appropriate set of functionals and basis functions.

4.3 Materials and methods

TDDFT was applied to estimate the absorption spectrum of SOD1 and COX. TDDFT calculations were carried out using the Gaussian 09W programme package.[36] The three-parameterised Becke-Lee-Yang-Parr (B3LYP) hybrid exchange-correction functional was employed,[37–39] and 6-311G** was used as a basis set.[40–42] Solvent effects were not considered in any of the processes.

For SOD1 analysis, a small region around a zinc ion of the SOD1 protein was extracted from the whole SOD1. The zinc ion is surrounded by histidine (His) and aspartic acid (Asp). Since proteins are so large that a supercomputer takes months to complete one TDDFT calculation, the extracted region was submitted for calculation instead. The structure is depicted in Figure 4.1: 3His-Zn-Asp.

On the other hand, for COX, a specific region around a copper ion - nitric oxide - iron ion (Cu-(NO)-Fe) binding with a porphyrin complex and histidine (His) was extracted. The model structure is depicted in Figure 4.2: 3His-Cu-(NO)-Fe($C_{20}N_4H_{12}$)-His (structure 1). On the basis of optimised Structure 1, the TDDFT method was applied to calculate the excited states relevant to NIR absorption.

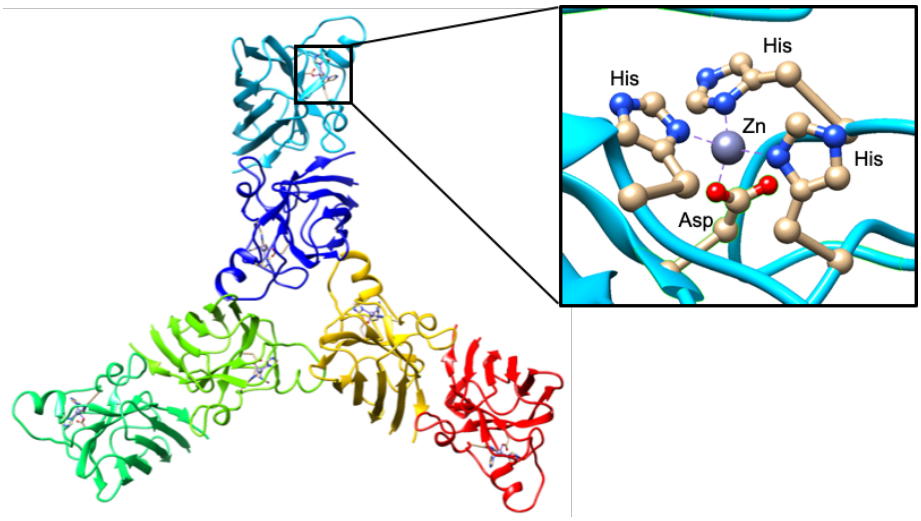

Figure 4.1. Superoxide dismutase 1 (SOD1) and the small region for calculation. SOD1 is an important protein for redox reaction. The zinc ion is surrounded by three histidine and aspheric acid.
PDB: 6FOI

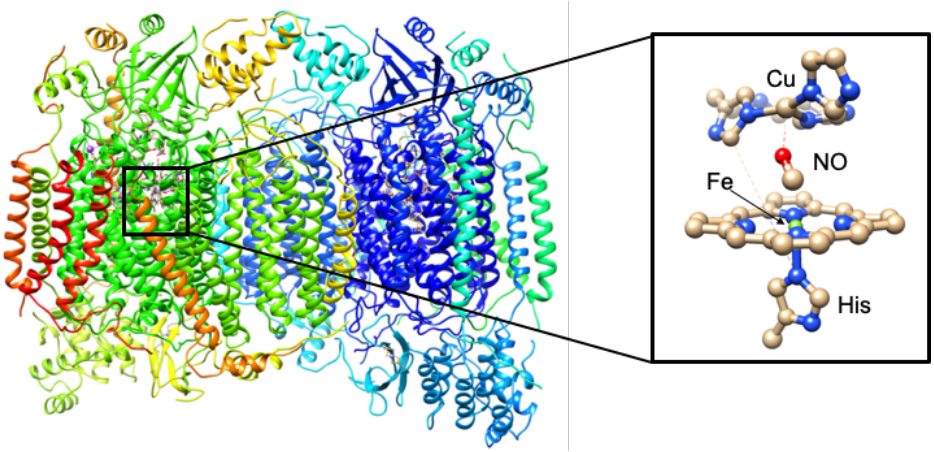

Figure 4.2. Cytochrome C oxidase (COX) and the small region for calculation. A copper ion, nitric oxygen and an iron ion are weakly bonded in COX. The iron ion is surrounded by a ring-shaped structure called porphyrin.
PDB: 5X1F

4.4 Results

4.4.1 Superoxide dismutase 1

In order to dissect the molecular mechanisms of action of photobiomodulation with NIR light beyond 1000 nm, the TDDFT computation was applied with the binding of zinc to SOD1. Table 1 shows the result of the TDDFT analysis, indicating that there is no absorption beyond 280 nm. Absorption below 300 nm is a typical phenomenon in proteins that is caused by tryptophan and histidine (280 nm), tyrosine (275 nm) and phenylalanine (258 nm).[43,44] These reported absorption wavelengths all correspond well to the data in Table 1. It can be concluded that SOD1 is not a NIR photoreceptor in biological tissue.

Table 1. Predicted absorption of the SOD1 model complex in the NIR region by the TDDFT method at the B3LYP/6-311G** level. No absorption was indicated above 278.62 nm.

λ_{calc} [a]/nm	E_{calc} [b]/eV	Oscillator Strength[c]	Configuration	Coefficient
278.62	4.45	0.0047	96→97 96→98 96→99	0.6421 -0.2584 -0.1208
272.01	4.56	0.0135	96→97 96→98 96→99 96→100	0.2386 0.6302 -0.1598 -0.1082
258.11	4.80	0.0015	96→99 96→100	-0.2531 0.6499
…	…	…	…	…

a: Absorption maxima

b: Corresponding transition energy calculated by TDDFT method

c: Oscillator strength calculated by TDDFT method

4.4.2 Cytochrome c oxidase

The TDDFT computation was applied with the binding of NO to an COX molecule (Figure 4.3). The results indicate that, in addition to absorption peaks of the porphyrin structure below 700 nm, which are well known, there are three multispectral absorbance peaks in the NIR range: 961, 1319 and 1372 nm (Table 2). These peaks derive from the electronic transition from molecular orbital (MO) 203 (Highest Occupied Molecular Orbital: HOMO) to low-lying, unoccupied orbitals (MOs 204-209). Figure 4.3(b) displays the molecular orbitals calculated for Structure 1. While the HOMO is centred at the bent Fe–N–O bonds and has the character of back bonding from the Fe d_{xz} orbital to the NO π* orbital, the unoccupied orbitals do not have the bonding interaction character between Fe and NO; MOs 204 and 205 are nearly degenerated *e*(Fe d_{π}–π_{por}*) orbitals, MO 206 is centred at the porphyrin ring, and MO 207 shows the antibonding interaction between Fe and NO. Therefore, the electronic transitions from HOMO caused by NIR light irradiation are expected to weaken the bonding between the Fe centre and the NO ligand.

The oscillator strength corresponds with the susceptibility to light. The calculated absorption peaks in the NIR spectrum at 961, 1319 and 1372 nm indicate that illumination with NIR light could result in NO release in the deep thickness of exposed tissue (e.g. the surface of the epidermis to the deepest layer of the dermis) due to its maximum depth of penetration in biological tissue.[45] Together with our previous studies showing the immunomodulatory effect of NIR light ranging from 1061 to 1301 nm,[1–4] 1064-nm and 1270-nm lasers were chosen in the following studies described in Chapter 5.

Table 2. Predicted absorption of the COX model complex in the NIR region by the TDDFT method at the B3LYP/6-311G** level.

λ_{calc} [a]/nm	E_{calc} [b]/eV	Oscillator Strength[c]	Configuration	Coefficient
1372.32	0.90	0.0001	203→204 203→205	0.574 -0.406
1318.91	0.94	0.0004	203→204 203→205	0.406 0.574
961.32	1.29	0.0002	203→206 203→207 203→209	-0.102 -0.682 0.115
…	…	…	…	…

a: Absorption maxima

b: Corresponding transition energy calculated by TDDFT method

c: Oscillator strength calculated by TDDFT method

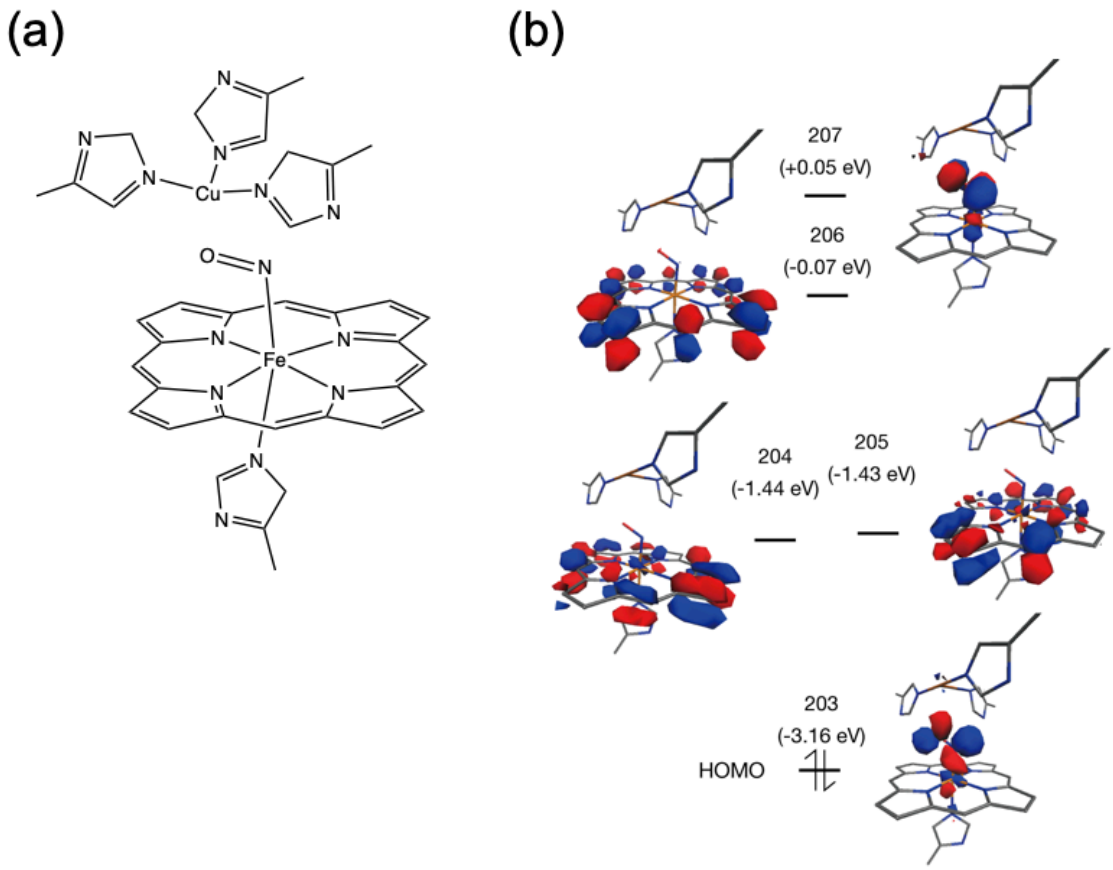

Figure 4.3. TDDFT analysis. (a) A part of the molecular structure of cytochrome c oxidase (COX, PDB: 5X1F) (Structure 1). Approximately, a region in a diameter of 8 angstrom from a nitric oxide molecule was extracted from COX. A copper ion is surrounded by three histidine, whereas nitric oxide binds to an iron ion, which is coupled with a porphyrin structure and a histidine. (b) Calculated molecular orbitals for complex 1 at the B3LYP/6-311G** level and the orbital diagram.

4.5 Discussion

The TDDFT method was applied to simulate the absorption spectrum of SOD1 and COX. The three-parameterised B3LYP hybrid exchange-correction functional[37–39] and the 6-311G** basis set[40–42] were selected. Among other functionals, such as BLYP and O3LYP, B3LYP has been the most widely used functional for over 20 years, due to its accuracy.[35,46] 6-311G** is also a common basis set. It can calculate the basic function of hydrogen (atomic number 1) to krypton (atomic number 36).

Many studies about photobiomodulation refer to a correlation between COX and light below 950 nm. So far, theoretical and *in vitro* studies have shown that there are absorbance peaks of copper in the putative photoreceptor COX in the NIR spectra at 620, 680, 760 and 820 nm, and biological readouts upon photobiomodulation could be the result of the significant effects of one distinct or a combination of several wavelengths of NIR light.[47–49] Although it has not yet been directly proven, NIR irradiation above 950 nm may result in NO release from COX. Considering that the oscillator strength of COX is relatively weak at the NIR range (Table 2), the light reaches deep into tissue, and photobiomodulation is induced in different layers of skin tissue.

The activities of NO have several clinical benefits in the human body. Intracellular NO acts as a signal molecule to promote cell growth and apoptosis.[50] Lukacs-Kornek *et al*. reported that NO mediates T cell activation and proliferation in LNs.[51] NO in blood vessels shows a relaxation of vascular endothelial cells that leads to a decrease of blood pressure.[52] As a result, cell migration of endothelial cells, DCs from blood vessels to tissue, or vice versa, is enhanced.[53,54] Further, the hypothesis that inhalation of NO gas may prevent coronavirus infection (SARS-CoV2) has been tested in recent studies.[55] Currently, 102–240 patients are planned for enrolment in a randomised Phase II clinical study at Massachusetts General Hospital to determine the antiviral effect on NO gas (NCT04306393, NCT04305457, details available at https://clinicaltrials.gov).[29] Although its mechanism and clinical effectiveness remain elusive, NO may have immunological benefits in addition to the well-known cardiovascular effects that could be useful in practice. The homeostasis of NO could be involved in COX activities and intervened by NIR light.

The limitation of TDDFT modelling is that it is not possible to declare the accuracy of the calculation with B3LYP and 6-311G** regarding the absorption wavelength. Different functionals and basis sets result in different results of absorption peak wavelengths.

Guillaumont *et al*. performed both experimental spectroscopy and TDDFT calculation. The results showed that TDDFT occasionally leads to a difference of more than 100 nm between the actual absorbance peak wavelength and the calculated wavelength.[56] Hence, the results may also contain errors compared to the actual absorbance. In order to clarify this point, it would be necessary to perform spectroscopy analysis using a purified COX solution under the presence of NO. A fluorescent probe, diamino fluorescein-FM, could be useful for observing the dissociation of NO from the COX complex in real time.[57]

4.6 Summary

This chapter reported, for the first time, that COX could absorb NIR light at multiple wavelengths – 961 nm, 1319 nm and 1378 nm – with the TDDFT method. Photobiomodulation could increase NO release from COX, resulting in positive reactions in the human immunological system. Although the theoretical method demonstrated the possibility that COX may play a critical role in photobiomodulation, the actual phenomenon in live cells has yet to be revealed. In the following chapter, *in vitro* studies carried out to observe intracellular molecular dynamics are discussed, as well as the provision of a tool that enables the definition of the best irradiance of lasers for clinical application.

Reference

1. Kimizuka, Y. *et al.* Brief Exposure of Skin to Near-Infrared Laser Modulates Mast Cell Function and Augments the Immune Response. *J. Immunol.* ji1701687 (2018) doi:10.4049/jimmunol.1701687.
2. Kashiwagi, S. *et al.* Near-infrared laser adjuvant for influenza vaccine. *PLoS One* **8**, (2013).
3. Kimizuka, Y. *et al.* Semiconductor diode laser device adjuvanting intradermal vaccine. *Vaccine* **35**, 2404–2412 (2017).
4. Morse, K. *et al.* Near-Infrared 1064 nm Laser Modulates Migratory Dendritic Cells To Augment the Immune Response to Intradermal Influenza Vaccine. *J. Immunol.* ji1601873 (2017) doi:10.4049/jimmunol.1601873.
5. Shihoya, W. *et al.* Crystal structure of heliorhodopsin. *Nature* **574**, 132–136 (2019).
6. Hamblin, M. R. Mechanisms and Mitochondrial Redox Signaling in Photobiomodulation. *Photochem. Photobiol.* **94**, 199–212 (2018).
7. Huang, Y. Y., Chen, A. C. H., Carroll, J. D. & Hamblin, M. R. Biphasic dose response in low level lightherapy. *Dose-Response* **7**, 358–383 (2009).
8. Hamblin, M. R., Huang, Y. Y., Sharma, S. K. & Carroll, J. Biphasic dose response in low level light therapy - an update. *Dose-Response* **9**, 602–618 (2011).
9. Huang, Y. Y., Nagata, K., Tedford, C. E. & Hamblin, M. R. Low-level laser therapy (810 nm) protects primary cortical neurons against excitotoxicity in vitro. *J. Biophotonics* **7**, 656–664 (2014).
10. Karu, T. I. Mitochondrial signaling in mammalian cells activated by red and near-IR radiation. *Photochem. Photobiol.* **84**, 1091–1099 (2008).
11. Karu, T. Is it time to consider photobiomodulation as a drug equivalent? *Photomed. Laser Surg.* **31**, 189–191 (2013).
12. Karu, T. Mitochondrial mechanisms of photobiomodulation in context of new data about multiple roles of ATP. *Photomed. Laser Surg.* **28**, 159–160 (2010).
13. Bohovych, I. & Khalimonchuk, O. Sending out an SOS: Mitochondria as a signaling hub. *Front. Cell Dev. Biol.* **4**, 1–15 (2016).
14. Chandel, N. S. Evolution of Mitochondria as Signaling Organelles. *Cell Metab.* **22**, 204–206 (2015).
15. Da Cunha, F. M., Torelli, N. Q. & Kowaltowski, A. J. Mitochondrial Retrograde Signaling: Triggers, Pathways, and Outcomes. *Oxid. Med. Cell. Longev.* **2015**, (2015).
16. Karu, T. I. & Kolyakov, S. F. Exact action spectra for cellular responses relevant to phototherapy. *Photomed. Laser Surg.* **23**, 355–361 (2005).
17. Sarti, P., Forte, E., Mastronicola, D., Giuffrè, A. & Arese, M. Cytochrome c oxidase and nitric oxide in action: Molecular mechanisms and pathophysiological implications. *Biochim. Biophys. Acta - Bioenerg.* **1817**, 610–619 (2012).
18. Borutaite, V., Budriunaite, A. & Brown, G. C. Reversal of nitric oxide-, peroxynitrite- and S-nitrosothiol-induced inhibition of mitochondrial respiration or complex I activity by light and thiols. *Biochim. Biophys. Acta - Bioenerg.* **1459**, 405–412 (2000).
19. Moncada, S. & Bolaños, J. P. Nitric oxide, cell bioenergetics and neurodegeneration. *J. Neurochem.* **97**,

1676–1689 (2006).

20. Boelens, R., Wever, R., Van Gelder, B. F. & Rademaker, H. An EPR study of the photodissociation reactions of oxidised cytochrome c oxidase-nitric oxide complexes. *BBA - Bioenerg.* **724**, 176–183 (1983).
21. Kim, H. P. Lightening up Light Therapy- Activation of Retrograde Signaling Pathway by Photobiomodulation. 491–496 (2014).
22. Galadari, S., Rahman, A., Pallichankandy, S. & Thayyullathil, F. Reactive oxygen species and cancer paradox: To promote or to suppress? *Free Radic. Biol. Med.* **104**, 144–164 (2017).
23. Zorov, D. B., Juhaszova, M. & Sollott, S. J. Mitochondrial reactive oxygen species (ROS) and ROS-induced ROS release. *Physiol. Rev.* **94**, 909–950 (2014).
24. Fulda, S., Galluzzi, L. & Kroemer, G. Targeting mitochondria for cancer therapy. *Nat. Rev. Drug Discov.* **9**, 447–464 (2010).
25. Moges, H. *et al.* Light therapy and supplementary riboflavin in the SOD1 transgenic mouse model of familial amyotrophic lateral sclerosis (FALS). *Lasers Surg. Med.* **41**, 52–59 (2009).
26. Yarosz, E. L. & Chang, C. H. Role of reactive oxygen species in regulating T cell-mediated immunity and disease. *Immune Netw.* **18**, 1–15 (2018).
27. Li, Q. *et al.* A possible cooperation of SOD1 and cytochrome c in mitochondria-dependent apoptosis. *Free Radic. Biol. Med.* **40**, 173–181 (2006).
28. Karu, T. Primary and secondary mechanisms of action of visible to near-IR radiation on cells. *J. Photochem. Photobiol. B Biol.* **49**, 1–17 (1999).
29. Lythgoe, M. P. & Middleton, P. Ongoing Clinical Trials for the Management of the COVID-19 Pandemic. *Trends Pharmacol. Sci.* **41**, 363–382 (2020).
30. Slater, J. C. A simplification of the Hartree-Fock method. *Phys. Rev.* **81**, 385–390 (1951).
31. Politzer, P. & Abu-Awwad, F. A comparative analysis of Hartree-Fock and Kohn-Sham orbital energies. *Theor. Chem. Acc.* **99**, 83–87 (1998).
32. Nakai, H. Energy density analysis with Kohn-Sham orbitals. *Chem. Phys. Lett.* **363**, 73–79 (2002).
33. Görling, A. Density-functional theory beyond the Hohenberg-Kohn theorem. *Phys. Rev. A - At. Mol. Opt. Phys.* **59**, 3359–3374 (1999).
34. Becke, A. D. Perspective: Fifty years of density-functional theory in chemical physics. *J. Chem. Phys.* **140**, 1–18 (2014).
35. Torres, E. & Dilabio, G. A. A (nearly) universally applicable method for modeling noncovalent interactions using B3LYP. *J. Phys. Chem. Lett.* **3**, 1738–1744 (2012).
36. Frisch, M. J. *et al. Gaussian 09*. (2016).
37. Raghavachari, K. Perspective on 'Density functional thermochemistry. III. The role of exact exchange'. *Theor. Chem. Acc.* **103**, 361–363 (2000).
38. Lecklider, T. Maintainng a heathy rhythm. *EE Eval. Eng.* **50**, 36–39 (2011).
39. Kassel, L. S. The limiting high temperature rotational partition function of nonrigid molecules: I. General theory. II. CH4, C2H6, C3H8, CH(CH3)3, C(CH 3)4 and CH3(CH2)2CH 3. III. Benzene and its eleven methyl derivatives. *J. Chem. Phys.* **4**, 276–282 (1936).
40. McLean, A. D. & Chandler, G. S. Contracted Gaussian basis sets for molecular calculations. I. Second

row atoms, Z=11-18. *J. Chem. Phys.* **72**, 5639–5648 (1980).

41. Frisch, M. J. & Pople, J. A. Self-consistent molecular orbital methods 25. Supplementary functions for Gaussian basis sets. *J. Chem. Phys.* **80**, 3265 (1984).
42. Krishnan, R., Binkley, J. S., Seeger, R. & Pople, J. A. Self-consistent molecular orbital methods. XX. A basis set for correlated wave functions. *J. Chem. Phys.* **72**, 650 (1980).
43. Schmid, F.-X. Biological Macromolecules: UV-visible Spectrophotometry. *Encycl. Life Sci.* 1–4 (2001) doi:10.1038/npg.els.0003142.
44. Ding, S., Li, Y. & Zhu, L. Identification of histidine residues at the active site of Megalobatrachus japonicus alkaline phosphatase by chemical modification. *Biochim. Biophys. Acta - Protein Struct. Mol. Enzymol.* **1594**, 100–108 (2002).
45. Kashiwagi, S., Brauns, T., Gelfand, J. & Poznansky, M. C. Laser vaccine adjuvants: History, progress, and potential. *Hum. Vaccines Immunother.* **10**, 1892–1907 (2014).
46. Lu, L., Hu, H., Hou, H. & Wang, B. An improved B3LYP method in the calculation of organic thermochemistry and reactivity. *Comput. Theor. Chem.* **1015**, 64–71 (2013).
47. Marcus, R. A. & Sutin, N. Electron transfers in chemistry and biology. *BBA Rev. Bioenerg.* **811**, 265–322 (1985).
48. Karu, T. I., Pyatibrat, L. V., Kolyakov, S. F. & Afanasyeva, N. I. Absorption measurements of a cell monolayer relevant to phototherapy: Reduction of cytochrome c oxidase under near IR radiation. *J. Photochem. Photobiol. B Biol.* **81**, 98–106 (2005).
49. Karu, T. I. Multiple roles of cytochrome c oxidase in mammalian cells under action of red and IR-A radiation. *IUBMB Life* **62**, 607–610 (2010).
50. Coleman, J. W. Nitric oxide in immunity and inflammation. *Int. Immunopharmacol.* **1**, 1397–1406 (2001).
51. Lukacs-Kornek, V. *et al.* Regulated release of nitric oxide by nonhematopoietic stroma controls expansion of the activated T cell pool in lymph nodes. *Nat. Immunol.* **12**, 1096–1104 (2011).
52. Lowenstein, C. J., Dinerman, J. L. & Snyder, S. H. Nitric oxide: A physiologic messenger. *Ann. Intern. Med.* **120**, 227–237 (1994).
53. Siew, H. W., Santambrogio, L. & Strominger, J. L. Caspases and nitric oxide broadly regulate dendritic cell maturation and surface expression of class II MHC proteins. *Proc. Natl. Acad. Sci. U. S. A.* **101**, 17783–17788 (2004).
54. Noiri, E. *et al.* Permissive role of nitric oxide in endothelin-induced migration of endothelial cells. *J. Biol. Chem.* **272**, 1747–1752 (1997).
55. Martel, J., Ko, Y.-F., Young, J. D. & Ojcius, D. M. Could nitric oxide help to prevent or treat COVID-19? *Microbes Infect.* (2020) doi:10.1016/j.micinf.2020.05.002.
56. Guillaumont, D. & Nakamura, S. Calculation of the absorption wavelength of dyes using time-dependent density-functional theory (TD-DFT). *Dye. Pigment.* **46**, 85–92 (2000).
57. Weinberg, J. B. *et al.* Inhibition of nitric oxide synthase by cobalamins and cobinamides. *Free Radic. Biol. Med.* **46**, 1626–1632 (2009).

Chapter 5

Real-time intracellular signal observation using multispectral laser gradient platform

In the previous chapter, TDDFT indicated that the COX protein absorbs NIR light at three different wavelengths above 950 nm. In order to elucidate the photobiomodulation of immune response induced by NIR light, the reaction of intracellular ROS and a Ca^{2+} ion against NIR light irradiation was investigated.

5.1 Introduction

NIR light (650–1700 nm) has been broadly investigated for application in medical procedures and bioimaging. Especially in LLLT, COX in the ETC in the mitochondria has drawn attention as a photoreceptor that initiates photobiomodulation. COX is the primary source of mitochondrial ROS generation (see Chapter 2).[1] NIR laser-induced ROS mediates the adjuvant effect in skin.[2–4] More specifically, mitochondrial ROS acts on NF-κB and stimulates IL-2 production and other pro-proliferative genes to encounter pathogens or endogenous cancer cells.[5] Recently, it has been demonstrated that defects in mitochondrial complex III cause decreased IL-2 production because ROS regulate the calcineurin-NFAT signalling pathway.[6] As such, because ROS and calcium signalling is important for mitochondrial retrograde signalling activated upon photobiomodulation,[7,8] a cultured T cell system was selected to establish an imaging methodology for the current study to examine the responses of cells to NIR light.

The previous chapter indicated that simultaneous, multiple laser irradiations may enhance the photobiomodulation reaction compared to a single irradiation.[9] To date, different parameters of laser irradiation have been tested for LLLT reaction in many ways; however, the best condition for laser irradiation has been poorly investigated, since the output is limited.[10–15] Furthermore, it is unrealistic to test all the different combinations of irradiance at two specific wavelengths because of the lack of an appropriate methodology.

Here, a high-throughput, single-cell resolution imaging methodology was performed to analyse the effects of multispectral NIR wavelengths at a range of irradiance on intracellular signalling pathways using established fluorescence imaging *in vitro*. A novel optical platform to investigate photobiomodulation in real time was established and validated with 1064-nm and 1270-nm NIR lasers.

5.2 Materials and methods

5.2.1 Optical setup

A schematic of the optical system is described in Figure 5.1. A continuous wave (CW) Nd:YAG laser (λ = 1064 nm, Ventus, Laser Quantum, UK) and indium phosphide (InP) semiconductor diode laser (λ = 1270 nm, spectral width = 8 nm/3dB, 202-000, Veralase LLC, USA) were used as sources of NIR light. To distribute the mode equally, these two optic paths were unified and directed through a multimode optic fibre (Core: 200 μm, NA: 0.22, Thorlabs, USA) and 1200-nm short-pass dichroic mirrors (Thorlabs, USA). Then, the beam shape was adjusted to a square through a square-core fibre (Core: 1000 μm, NA: 0.22, Fiberguide industries, USA) at a focal plane. The squared 1064-nm and 1270-nm laser beams were further divided into two pathways using a dichroic mirror, followed by 2-dimensional (2D) gradation creation through continuously variable neutral-density (ND) filters (OD: 0.04-2.00, Thorlabs, USA). Beam shapes of the laser at a desired plane were determined by a beam profiler (Thorlabs Beam 7.0, Thorlabs, USA).

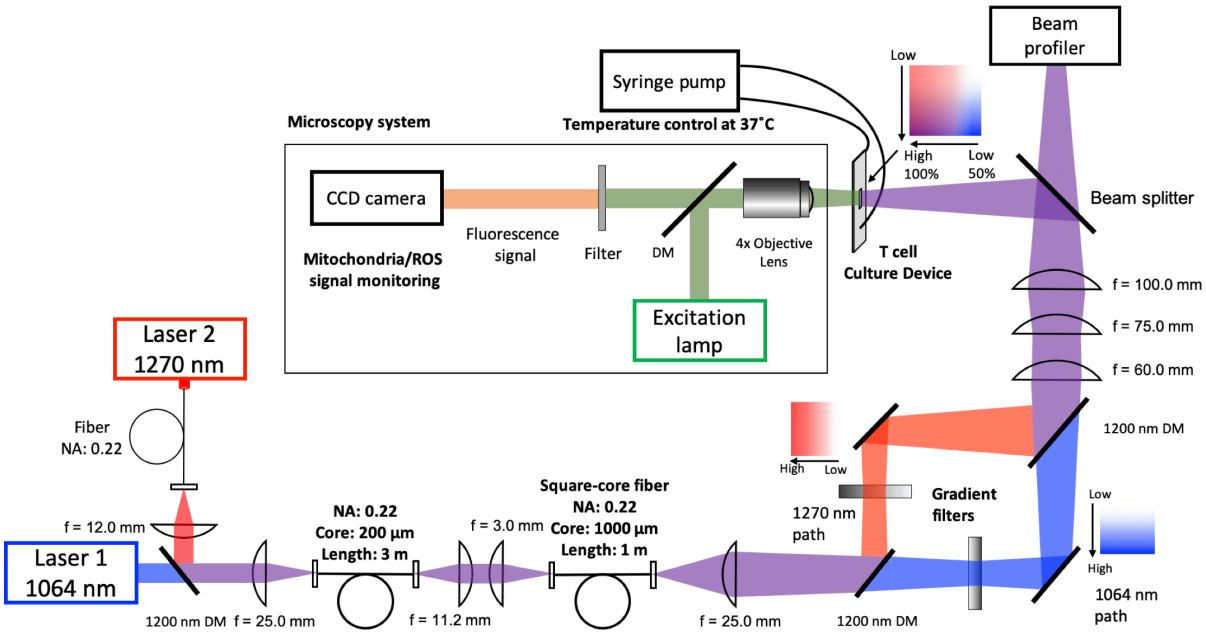

Figure 5.1. A schematic of the real-time, single-cell, live imaging system capable of dual near-infrared (NIR) laser irradiation. The 1064-nm and 127-nm square laser beams were transformed into a gradient square beam profile at a focal plane on a cell culture device. The 1064-nm and 1270-nm laser paths were divided into two through 1200-nm short-pass dichroic mirrors (DM) to create gradient beams in irradiance, then merged into one square beam. To minimise chromatic aberration, achromatic lenses were used as appropriate in the optical paths. For live imaging, a mercury lamp was used for an excitation light source. The fluorescence signal from cultured cells in the culture chamber was captured by a charge-coupled device (CCD) camera on a fluorescence microscope.

5.2.2 Fabrication of cell culture device for laser illumination

The design of the cell culture device is depicted in Figure 5.2 (a-b). To achieve a single-layer cell culture of T cells with no convection at a constant temperature during laser irradiation, a cell culture device was established using conventional soft lithography. The Si master mould was fabricated using two layers of photoresistance. The first layer of photoresistance, SU-8 10 (Microchem, USA), for a cell culture chamber, was spin-coated at 1250–2200 rpm for 40 sec (15–25 μm). The second layer of photoresistance, SU-8 100, for temperature control, was then spin-coated at 1100 rpm for 40 s (250 μm). After development, the resultant wafer was placed in a square dish, after which a polydimethylsiloxane (PDMS) prepolymer (a mixture of 10:1 silicon elastomer and curing agent, Sylgard 184, Dow Corning, USA) was poured into it. Then, the square dish was cured in an oven at 70˚C for 8 h. Prior to use, the device was sterilised by ethylene oxide gas. The water flow channel was connected to a peristatic pump so that pre-warmed water at 37˚C flowed into the channel to minimise temperature change in the cultured cells in the device, as shown in Figure 5.2 (c-d).

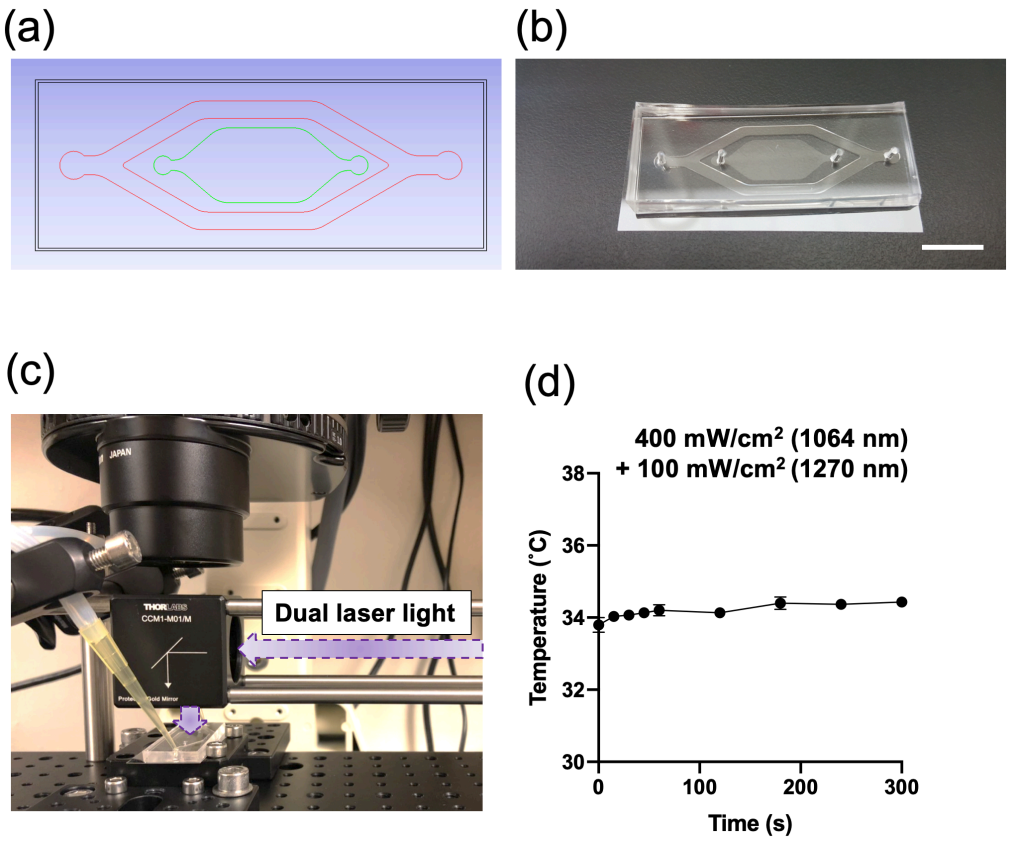

Figure 5.2. The design of a cell culture chamber for laser irradiation. (a) The design of the polydimethylsiloxane (PDMS) device. Red lines denote a water flow channel for temperature control, and green lines show a cell culture channel. T cells were inoculated and cultured in the cell culture channel without flow. (b) A photo of the PDMS device. Bar = 1.0 cm. (c) The PDMS device installed on the imaging system. The photo shows the relative location of the laser beam to the chamber with the water flow channel connected to the water circulation system. (d) Measurements of temperature of the culture chamber during dual laser irradiation (n = 3). The temperature of the chamber was measured using an IR camera.

5.2.3 T cell culture

All animal procedures were approved by the Massachusetts General Hospital (MGH) IACUC (protocol number 2009N000103) and performed under the Public Health Service Policy on Human Care of Laboratory Animals.

Eight-week-old female C57BL/6J mice (stock 000664) were purchased from Jackson Laboratories (USA) and acclimated for at least 2 weeks at MGH. To obtain purified T cells, the spleen was removed, individually dissociated, and passed through 70- μm and 40-μm mesh filters to obtain single-cell suspensions. Erythrocytes were then removed using erythrocyte lysing buffer (eBioscience, USA). Splenocytes were further purified to obtain T cells using magnetic beads (EasySep^{TM} T cell isolation kit, STEMCELL Technologies, Canada). The purified T cells were washed and resuspended at a concentration of 1×10^6 cells/mL and incubated overnight in RPMI1640 (Thermo Fisher Scientific, USA) containing 10% FBS (Thermo Fisher Scientific, USA), 100 unit/mL penicillin/streptomycin (Thermo Fisher Scientific, USA), 0.5% 2-mercaptoethanol (Thermo Fisher Scientific, USA) and 10 mM HEPES buffer (Thermo Fisher Scientific, USA) in a 5% CO_2 incubator at 37˚C.

5.2.4 Laser irradiation on T cells and imaging of intracellular calcium level and reactive oxygen species accumulation

To examine intracellular signalling pathways activated by NIR laser light, well-established fluorophores were used to measure the levels of intracellular calcium and mitochondrial ROS. Purified T cells were loaded with 4 μM Fluo-4 AM (Thermo Fisher Scientific, USA)[16] and 5 μM MitoSOX Red (Thermo Fisher Scientific, USA)[17] for 30 min in RPMI1640. The cells were then washed with HBSS buffer containing 0.5% FBS and 10 mM HEPES. Resuspended cells in 2 μL of culture medium at a concentration of 8×10^5 cells/μL were put into a cell culture channel on the PDMS device.

The cells on the cell culture channel were irradiated with the dual-squared laser beam for 1 min as depicted in Figure 5.2(c). The gradient irradiance of the two lasers was adjusted to 200–400 mW/cm^2 for 1064 nm and 50–100 mW/cm^2 for 1270 nm at the focal plane. The size of the square beam was also adjustable, between 1.2 × 1.2 and 4.0 × 4.0 mm. To keep the temperature in the system constant, a peristatic pump (Cole-Parmer, USA) was used to

circulate water, warmed to 37˚C, into the PDMS device in the water flow channel. The temperature in the cell culture area during dual laser irradiation at an irradiance of 400 mW/cm^2 for 1064 nm and 100 mW/cm^2 for 1270 nm was monitored using an infrared camera (FLIR Systems, USA).

To measure the fluorescence signals, the cells in the PDMS device were illuminated using a Xenon lamp (Nikon, Japan). The signals from Fluo-4 (Excitation/Emission: 494/516 nm) and MitoSOX Red (510/580 nm) were captured using a fluorescence microscopy system (DIAPHOT200, Nikon, Japan). The fluorescence signal passed through a 4× objective lens (NA = 0.13, Nikon, Japan), and cube filters were captured by a CCD digital camera (Hamamatsu, Japan). The exposure time of the camera was set to 1000 ms.

5.2.5 Image analysis

The image analysis scheme is shown in Figure 5.3-5.4. First, captured images were processed using a 3 × 3 Gaussian filter to reduce background noise. Second, a pixel which showed a maximum intensity in the nearest 5 × 5 pixels (approximately 8 × 8 μm) above the empirically determined threshold was recognised as a fluorescence signal. Cells which were stably located at the same position over time were selected for further analysis. A fold change of the fluorescence signal intensity at a desired time point over the signal before the illumination was calculated. The cells' geometric coordinates were converted into irradiances using curve fittings for the dual square beam, as shown in Figure 5.3. The analysis software programme was developed using a programming language, Python 3.6., and OpenCV 2 (Appendix 2, programmes are also available at https://github.com/wkatagiri/CB001).

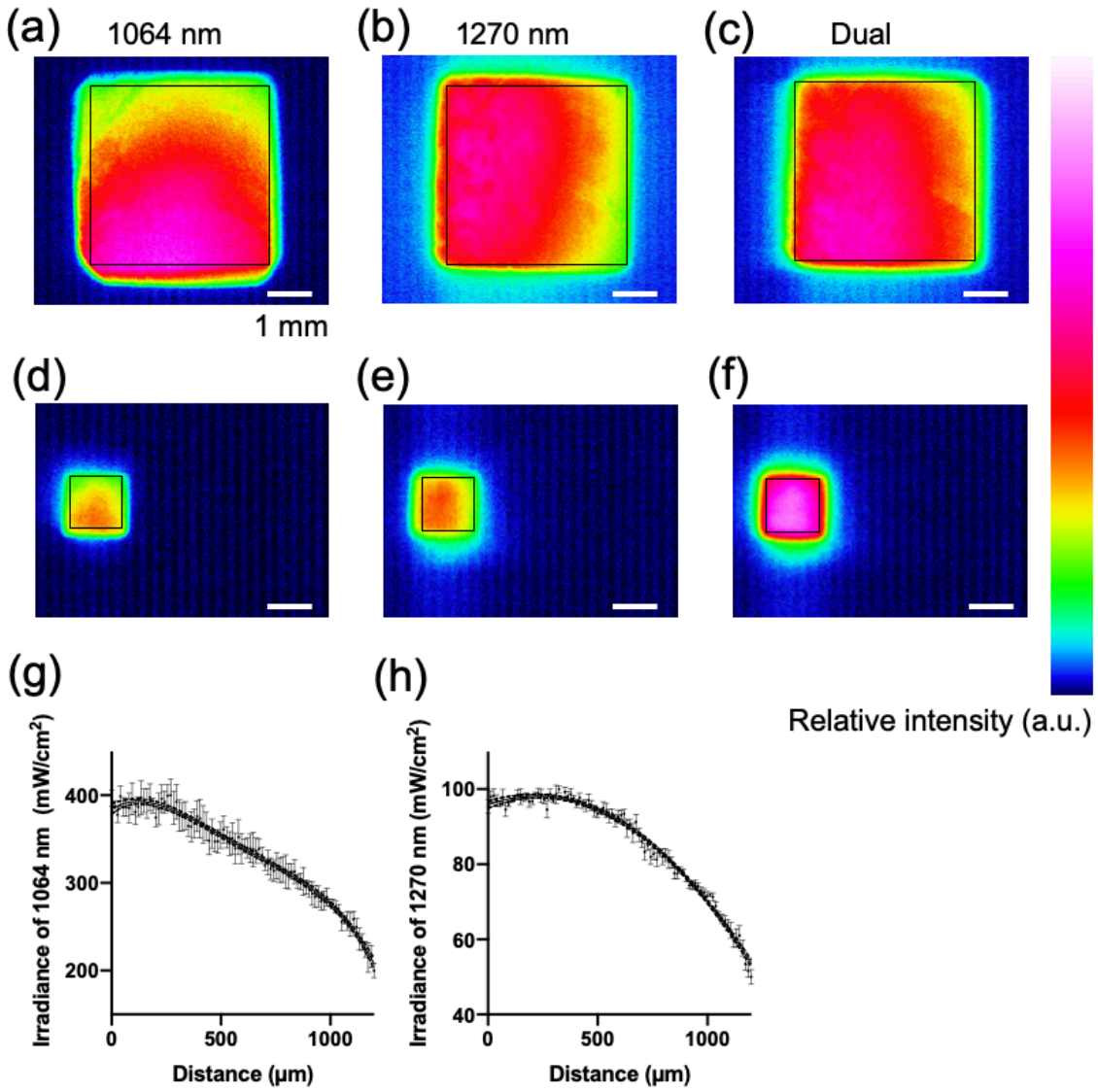

Figure 5.3. Measurements of the density gradient of the dual laser beam. Relative intensities of different sizes of gradient square beams are shown. The sizes of laser beams are shown in black squares. (a)-(c) 4.0 × 4.0 mm; (d)-(f) 1.2 × 1.2 mm; (a, d) 1064-nm and (b, e) 1270-nm gradient beams were merged into one (c, f). The gradients were fitted into non-linear curves: (g) 1064 nm (n = 5, mean ± SEM) and (h) 1270 nm (n = 5, mean ± SEM). The curve fittings were performed using the least square method, with the degrees of the polynomial selected by Akaike's information criterion (AIC). Dash lines show a 95% confidence interval (CI).

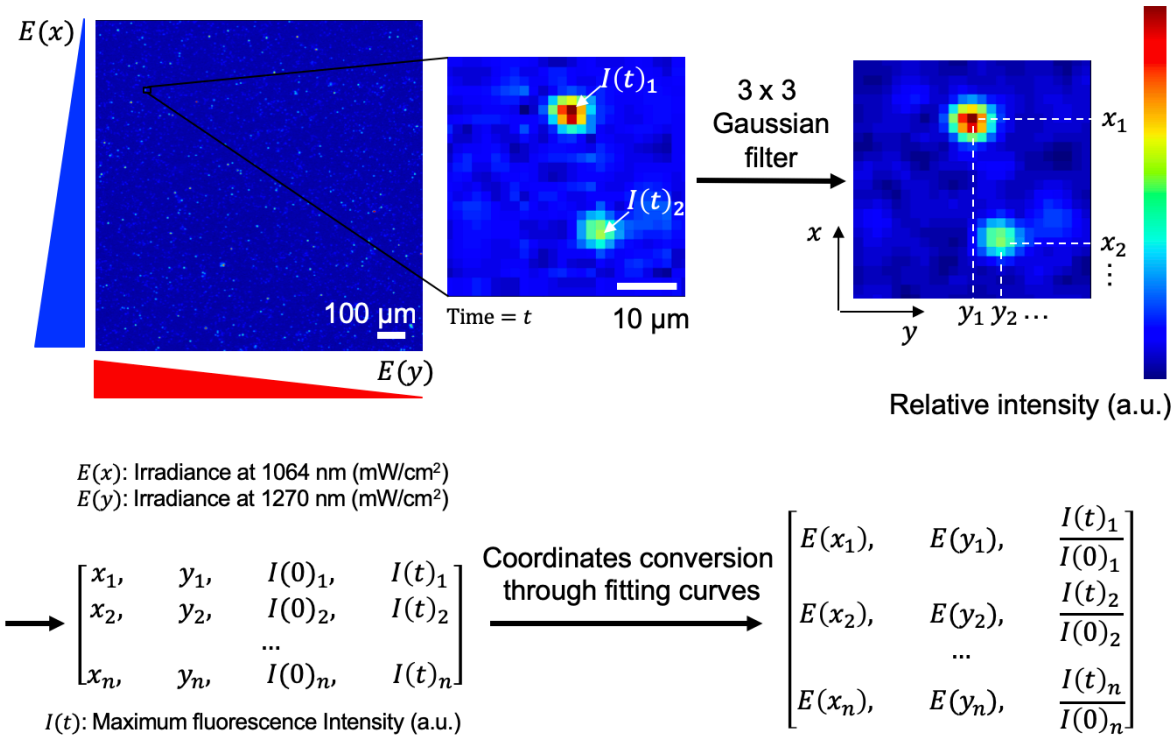

Figure 5.4 Image analysis strategy. Fluorescence images were captured at 0, 1 and 5 min after the conclusion of laser irradiation. First, the images were convolved with a Gaussian filter. The pixel coordinates with the maximum intensity were defined as the location of individual cells, which were further converted into irradiances of both 1064-nm and 1270-nm lasers using the curve fittings shown in Figure 5.3 (g-h). The fluorescence intensity was measured in the pre-filtered images. The fold change of the fluorescence signal at 1 min and 5 min over that before laser irradiation was calculated for each time point.

5.2.6 Statistical analysis

One-way ANOVA followed by Tukey's multiple comparison tests were performed for comparisons of more than two groups using GraphPad Prism version 8. The mean ± SEM was displayed for all figures. A corrected *P* value of less than 0.05 in a multiple comparison test was considered to be significant.

5.3 Results

5.3.1 Development of optical platform equipped with two distinct wavelengths of near infrared lasers

First, a culture chamber for T cells that was amenable for laser illumination was constructed. The device was designed using computer-aided (CAD) software (Figure 5.2(a)) and developed by conventional photolithography and soft lithography (Figure 5.2(b)). The device is 18 × 48 mm in size and consists of two channels: a water flow channel (shown in red) and a cell culture channel (green). The water flow channel was connected to tubes to circulate warmed water while the laser irradiated the middle of the cell culture area, as shown in Figure 5.2(c). The water flow channel was designed to accommodate water flow at a speed of up to 30 mL/min through peristatic pumping. The cell culture channel was surrounded by the water flow channel to achieve homogeneous temperature distribution over the cell culture area. To assess the thermal transfer from the water channel to the cell culture chamber, the temperature distribution in the cell culture area was measured in real time during laser irradiation by an IR camera (Figure 5.2(d)). The temperature was stable, between 33–35˚C, during simultaneous irradiation at 400 mW/cm^2 for the 1064-nm and 100 mW/cm^2 for the 1270-nm laser for up to 5 min. Hence, the effect of heat generation with laser irradiation on cultured cells in the channel was considered negligible in the following analysis, which used lower irradiances of the NIR laser than that used in this measurement.

5.3.2 Dual laser beam shaping

Next, an optical system was constructed in which the system irradiated the cultured cells with the NIR laser and performed bioimaging at the same time. Two different sizes of the square beams were created by adjusting the positions of plano-convex and achromatic lenses between gradient filters and the cell culture device (Figure 5.3(a-f)). The size of the square beam varied from 1.2 × 1.2 to 4.0 × 4.0 mm. The smallest 1.2-mm square beam was adjusted to the FOV through a 4× objective lens (NA = 0.13, Nikon Japan), whereas the largest 4.0-mm square beam was adjusted for a 2.5× objective lens (NA = 0.075, Nikon, Japan). Although both the smallest and largest squares could be applied for illumination sources, intracellular fluorescence signals in T cells could not be clearly recognised by the CCD camera with a 2.5× objective lens (data not shown). Therefore, the following experiments were conducted with the smallest 1.2-mm square using the 4× objective lens.

Curve fittings of the irradiance gradient of 1064 nm and 1270 nm in the field are shown in Figure 5.3 (g-h). The line profiles of irradiance were measured towards the gradient vectors with a beam profiler. The measurement results were plotted, and the curve fittings for each wavelength were then calculated based on the least square method. The gradient of irradiance of 1064 nm was fitted into quartic function $E(x)$ (Eq. 1), whereas that of 1270 nm was fitted into quadratic function $E(y)$ (Eq. 2), as shown below:

$$\mathrm{E}(x) = 384.3 + (0.1546)x - \left(7.934\times10^{-4}\right)x^2 + \left(9.238\times10^{-7}\right)x^3 - \left(3.934\times10^{-10}\right)x^4 \qquad (1)$$

$$\mathrm{E}(y) = 95.82 + \left(2.091\times10^{-2}\right)y - \left(4.679\times10^{-5}\right)y^2 \qquad (2)$$

The degree of each curve-fitting function was determined by AIC. The narrow 95% CI of each curve fitting is shown in Figure 3(g-h) and suggests that the fitting strategy used was satisfactory, and that the irradiance gradient of the two lasers was established successfully with the optical setting.

5.3.3 Calcium and reactive oxygen species responses upon near infrared laser irradiation

Both intracellular calcium and mitochondrial ROS signalling play a critical role in regulating diverse T cell functions.[5,6,18–20] Thereby, this study analysed calcium and mitochondrial ROS responses in T cells induced by NIR laser irradiation using the platform established above.

T cells loaded with either calcium probe Fluo-4 or ROS probe MitoSOX Red in the cell culture channel in the PDMS device were irradiated with the dual-squared laser beam at a gradient irradiance of 200–400 mW/cm^2 for the 1064-nm and 50–100 mW/cm^2 for the 1270-nm laser. The fluorescence images were acquired using a fluorescence microscopy system equipped with a CCD digital camera. A fold change of the fluorescence signal intensity at a desired time point over the signal before the illumination was calculated for individual T cells on the captured images. As shown in Figure 4, the geometric information of each T cell in the imaging field was converted into an irradiance of 1064 nm and 1270 nm using the curve fitting with a non-linear regression method.

Figure 5.5(a) shows the colour map of fold changes in fluorescence intensity at 1 and 5 min after the laser irradiation. The population of T cells were divided into 25 groups based on the irradiance of 1064 nm and 1270 nm exposed on the cells and showed the mean fluorescence intensity of each group. Interestingly, both calcium and mitochondrial ROS signals showed a tendency to decrease (< 1.0) after the laser irradiation (Figure 5.5(a)). The fold changes across combinations of lower irradiances of the 1064 nm and 1270 nm lasers were then compared (Figure 5.5(b-e)). In these comparisons, the fluorescence signals at 1 and 5 min were compared with those at 0 min (before the laser) to consider various factors, including photobleaching and leakage of the fluorophore over time. Notably, there was a clear tendency for combinations of relatively low irradiances at 250–400 mW/cm^2 for the 1064-nm and 55–65 mW/cm^2 for the 1270-nm laser to suppress calcium at 1 min (Figure 5.5(b)). In addition, the calcium signal was significantly decreased with dual irradiation at 300 mW/cm^2 with the 1064-nm and 55 mW/cm^2 with the 1270-nm laser compared with that of the no laser control group (P = 0.0402). The signal returned to the control level 5 min after the laser irradiation (Figure 5.5(c)). Although statistical analysis did not indicate any significant difference, mitochondrial ROS also decreased with irradiances at 250–400 mW/cm^2 for the 1064-nm and 55–65 mW/cm^2 for the 1270-nm laser at 1 min (Figure 5.5(d)). The change in the ROS signal also disappeared 5 min after the laser treatment (Figure 5.5(e)). Together, these results indicate that a specific

combination of low-irradiance 1064-nm and 1270-nm lasers suppresses intracellular calcium and mitochondrial ROS signals in T cells.

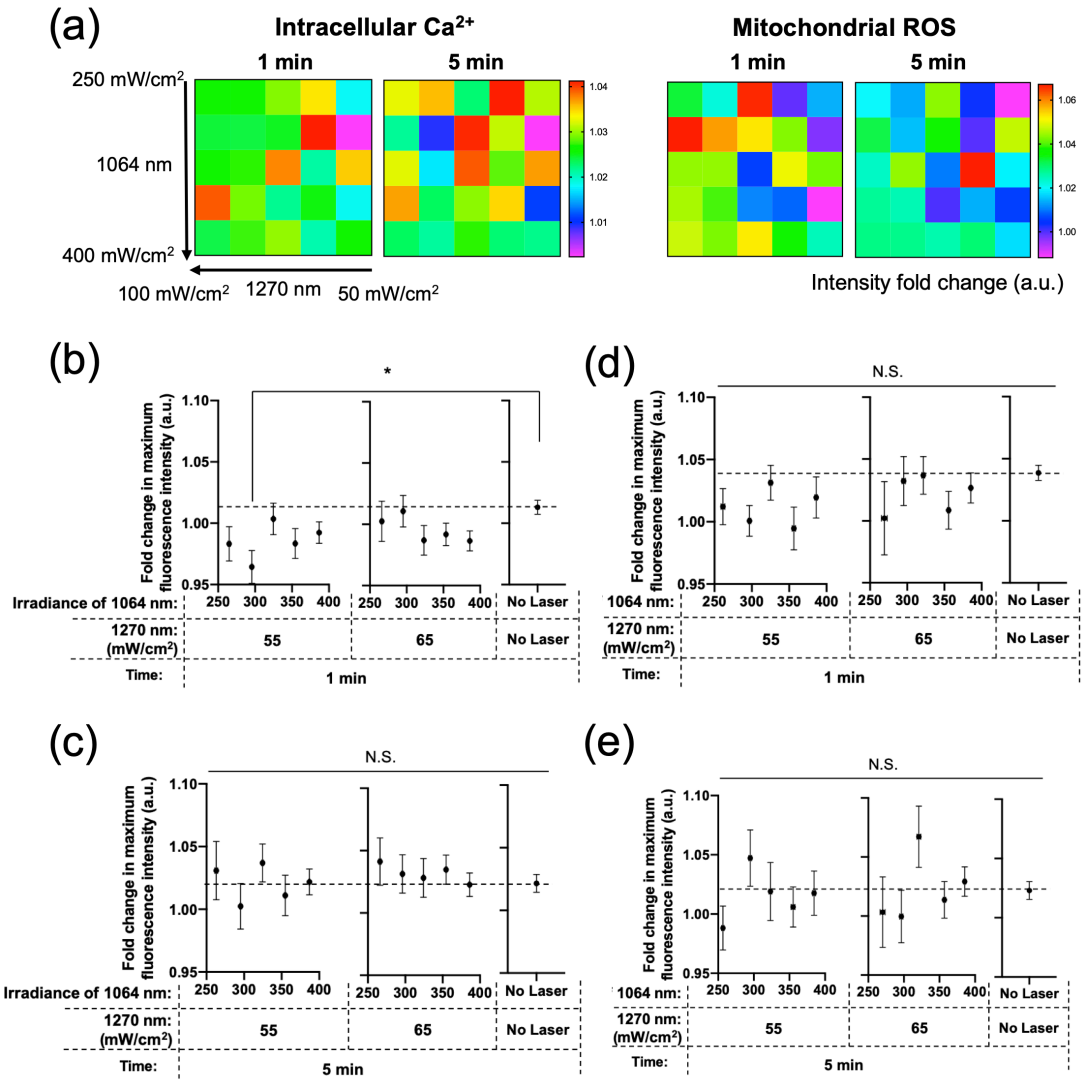

Figure 5.5. The fold change of the fluorescence signals of intracellular calcium and ROS upon dual NIR laser exposures. The fold change of the fluorescence signals at each time point over the signals before the laser irradiation was calculated for individual T cells on the captured images. (a) Colour maps of the fluorescence signal changes 1 and 5 min after the laser irradiation. (b-c) The fold changes of the intracellular calcium signal at (b) 1 min (n = 30–284) and (c) 5 min (n = 20–249). (d-e) The fold changes of the ROS signal at (d) 1 min (n = 9–111) and (e) 5 min (n = 7-92). (a-e) The results under gradient irradiances between 250–400 mW/cm^2 for the 1064-nm and 50–100 mW/cm^2 for the 1270-nm laser are shown. Results were pooled from two independent experiments. Error bars for x and y axes denote the SEM. A P value less than 0.05 was considered significant: * $P < 0.05$; *N.S.*, not significant by one-way ANOVA followed by Tukey's multiple comparison test.

5.4 Discussion

This study established for the first time a high-throughput imaging system at a single-cell resolution to evaluate the responses of intracellular calcium and ROS signalling pathways in order to determine an optimal parameter of the NIR laser for effective photobiomodulation based on an established fluorescence imaging system *in vitro*. Since the effects of NIR light are diverse and the range of the wavelength and irradiance of effective NIR light are wide, finding an optimal parameter for a desirable biological effect is often challenging. This platform is therefore a powerful tool for identifying the best-performing combination of NIR wavelengths and irradiances not only for photobiomodulation but more broadly for other applications in photomedicine, including photodynamic and photo-thermal therapy, thereby contributing to maximising the efficacy and safety of these treatment modalities.

There are two new features in this optical platform. First, an irradiation chamber was newly designed with a PDMS elastomer. PDMS is widely used in biomedical applications owing to its excellent flexibility and transparency in the visible light spectrum.[21] PDMS also shows very little optical insertion loss in the NIR light spectrum, such as in 900–1100 nm and 1250–1350 nm, to the extent of less than 0.03 dB/cm[22]. Therefore, PDMS can be applied for NIR illumination with minimal loss of light intensity and heat generation. Since the temperature during the dual laser irradiation at the large irradiance of 400 mW/cm^2 for the 1064-nm and 100 mW/cm^2 for the 1270-nm laser was measured to be constant for a prolonged period, the effect of heat generation upon laser illumination, which might cause intracellular ROS production[23] and intracellular calcium accumulation,[24] can be disregarded in the current study. Thus, this platform allows for the determination of the photochemical effect of the NIR laser separately from its photothermal effect, which is generated by light absorption. Second, the system using a square beam profile allows for the simultaneous high-throughput measurement of the photochemical effect of the multispectral laser with a wide range of irradiance. Generally, a Gaussian beam profile is used to determine the threshold of the monospectral laser in an *in vitro* setting.[25–27] However, in the current study, a square gradient beam profile was chosen as being appropriate for a dual laser in order to simplify the experimental procedures. A square-core fibre was used to create a square beam profile because using the fibre is easier and more affordable than the phase-gating method[28] or a micromirror device.[29] Such a system is useful for studying the biological effect of NIR light in order to reveal its mechanisms and determine the best parameters.

Exposures to NIR light between 760–1400 nm has been demonstrated to increase ROS generation or accumulation in a wide variety of cells and tissues, including tumour cells,[30–32] keratinocytes,[31] fibroblasts[33] and skin tissue.[34–36] ROS have been postulated to act on mitochondrial COX in the ECT in response to NIR light exposure,[37,38] ultimately resulting in photobiomodulation.[7,39,40] These studies generally used broadband light, which renders the interpretation of the impact of such light on the biological system difficult. Since theoretical[9,41] and *in vitro* studies[42,43] showed that there are absorbance peaks of copper in the putative COX photoreceptor in the NIR spectra at 620, 680, 760 and 820 nm, biological readouts upon photobiomodulation could be the result of significant effects of one distinct or a combination of several wavelengths of NIR light. In order to further understand the mechanism of action of photobiomodulation, it is desirable to establish a reproducible tool to examine the effect of individual or a combination of parameters of NIR light on physiological functions. In addition, as a wide range of irradiance of NIR light (1 mW–5 W/cm^2) has been reported to promote photobiomodulation,[7,8,39,40,44] whereas over-dosed photoirradiation has been reported to downregulate the signalling pathways,[10,39,45] such a tool should be able to examine a reasonably wide range of parameters simultaneously to identify a causal NIR laser parameter. In response to this, the reported system was designed to have the capability of evaluating a combination of multiple wavelengths and a wide range of irradiance simultaneously.

ROS generation in response to NIR light has been demonstrated to involve modulation of the binding of gaseous monoxides, including NO and CO, to COX subunit I, between copper and iron.[46–49] In the series of studies, NIR light was shown to alter cell metabolism, as it displaces CO or NO gas molecules on histidine in the COX protein,[50] resulting in the generation of ROS led by photobiomodulation.[1,51] While most of these studies employed visible and NIR light below 950 nm,[45,52–54] some recent studies have indicated the modulatory effect of NIR light beyond 1000 nm on COX. Wang *et al*. demonstrated that brief exposure of the skin of human subjects with 1064-nm NIR light at an irradiance of 250 mW/cm^2 induced the upregulation of COX and haemoglobin oxygenation.[55] In contrast, Sanderson *et al*. showed that COX activity was strongly suppressed by dual irradiation with 750-nm and 950-nm lasers.[56] The previous chapter showed that three NIR wavelengths beyond 950 nm could possibly modulate the binding of NO to COX using a TDDFT calculation. The study further demonstrated that a combination of 1064-nm and 1270-nm lasers suppressed mitochondrial retrograde signalling, including intracellular calcium and ROS (Figure 5.5). These results suggest that NIR light beyond 1000 nm is able to act on COX, ultimately modulating ROS generation in mitochondrial ETC. This is consistent with our previous study showing that a

1064-nm NIR laser induced ROS generation in skin cells.[4] Furthermore, Schroeder *et al*. similarly demonstrated that broadband NIR light (760–1440 nm) induced mitochondria-derived ROS generation and the subsequent increase in redox potential in cultured human dermal fibroblasts.[33] Thus, the current study collectively suggests that NIR light beyond 1000 nm demonstrates photobiomodulation via mitochondrial retrograde signalling.

ROS are known to regulate the differentiation and effector functions of T cells. High environmental ROS favour the development of T helper (T_H) 2 cells with increased IL-2 and IL-4 production, skewing towards a T_H2-skewed immune response.[57,58] In contrast, low ROS promote T_H1 and T_H17 cell differentiation, and the use of antioxidants increases the production of interferon (IFN)-γ, which is a proinflammatory cytokine active in both innate and adaptive immune response, skewing the immune response to a T_H1 phenotype.[57,59,60] As such, this system can be useful for discovery research to identify a laser parameter modulating T cell function for therapeutic purposes. For example, with this system, a laser parameter to potentially ameliorate autoimmune inflammation in multiple sclerosis (MS) could be identified. MS is a neurodegenerative disorder characterised by the infiltration of autoreactive CD4 T cells against myelin in the central nervous system (CNS).[61] Since the autoreactive T cells are known to secrete high levels of T_H1 and T_H17 cytokines, and because the administration of pro-oxidants prevents the production of these inflammatory cytokines, as high environmental levels of ROS promote the development of T_H2 cells,[57,60] a parameter of NIR light to modulate ROS in T cells may reduce the severity of MS. In fact, a recent report showed that the modulation of the Nrf2-mediated antioxidant pathway in T cells prevents CD4 T cell infiltration into the CNS, thereby ameliorating autoimmune inflammation,[62] suggesting that this approach, simple irradiation by an NIR laser, would have a clinical impact. Further work is warranted to determine if this system could be broadly used to discover such a combination parameter of the NIR laser.

5.5 Summary

This chapter demonstrated an optical platform that allows for real-time, single-cell live imaging of the intracellular signalling induced with multiple doses of two wavelengths of NIR laser light simultaneously *in vitro*. Armed with this system, it was revealed that a 1-min exposure of cultured T cells with a specific combination of 1064-nm and 1270-nm NIR lasers at low irradiances suppressed intracellular calcium and mitochondrial ROS signals. These results indicate that a parameter of NIR light beyond 1000 nm promotes photobiomodulation. This novel system would be not only useful for further mechanistic studies of photobiomodulation but also constitutes a powerful tool for investigating optical and biological responses in photomedicine.

Reference

1. Da Cunha, F. M., Torelli, N. Q. & Kowaltowski, A. J. Mitochondrial Retrograde Signaling: Triggers, Pathways, and Outcomes. *Oxid. Med. Cell. Longev.* **2015**, (2015).
2. Kashiwagi, S. *et al.* Near-infrared laser adjuvant for influenza vaccine. *PLoS One* **8**, (2013).
3. Morse, K. *et al.* Near-Infrared 1064 nm Laser Modulates Migratory Dendritic Cells To Augment the Immune Response to Intradermal Influenza Vaccine. *J. Immunol.* ji1601873 (2017) doi:10.4049/jimmunol.1601873.
4. Kimizuka, Y. *et al.* Brief Exposure of Skin to Near-Infrared Laser Modulates Mast Cell Function and Augments the Immune Response. *J. Immunol.* ji1701687 (2018) doi:10.4049/jimmunol.1701687.
5. Kamiński, M. M. *et al.* T cell Activation Is Driven by an ADP-Dependent Glucokinase Linking Enhanced Glycolysis with Mitochondrial Reactive Oxygen Species Generation. *Cell Rep.* **2**, 1300–1315 (2012).
6. Sena, L. A. *et al.* Mitochondria Are Required for Antigen-Specific T Cell Activation through Reactive Oxygen Species Signaling. *Immunity* **38**, 225–236 (2013).
7. Karu, T. I. Mitochondrial signaling in mammalian cells activated by red and near-IR radiation. *Photochem. Photobiol.* **84**, 1091–1099 (2008).
8. Karu, T. Mitochondrial mechanisms of photobiomodulation in context of new data about multiple roles of ATP. *Photomed. Laser Surg.* **28**, 159–160 (2010).
9. Katagiri, W. *et al.* High-throughput single-cell live imaging of photobiomodulation with multispectral near-infrared lasers in cultured T cells. *J. Biomed. Opt.* **25**, 036003 (2020).
10. Migliario, M., Pittarella, P., Fanuli, M., Rizzi, M. & Renò, F. Laser-induced osteoblast proliferation is mediated by ROS production. *Lasers Med. Sci.* **29**, 1463–1467 (2014).
11. Chow, R. T., Johnson, M. I., Lopes-Martins, R. A. & Bjordal, J. M. Efficacy of low-level laser therapy in the management of neck pain: a systematic review and meta-analysis of randomised placebo or active-treatment controlled trials. *Lancet* **374**, 1897–1908 (2009).
12. Usumez, A. *et al.* Effects of laser irradiation at different wavelengths (660, 810, 980, and 1,064 nm) on mucositis in an animal model of wound healing. *Lasers Med. Sci.* **29**, 1807–1813 (2014).
13. Huang, Y. Y., Nagata, K., Tedford, C. E. & Hamblin, M. R. Low-level laser therapy (810 nm) protects primary cortical neurons against excitotoxicity in vitro. *J. Biophotonics* **7**, 656–664 (2014).
14. Chen, A. C. H. *et al.* Low-Level laser therapy activates NF-kB via generation of reactive oxygen species in mouse embryonic fibroblasts. *PLoS One* **6**, 1–8 (2011).
15. Avci, P., Gupta, A. & Sadasivam, M. Low-Level Laser (Light) Therapy (LLLT) in Skin: Stimulating, Healing, Restoring. (2013).
16. Salles, A. *et al.* Barcoding T Cell Calcium Response Diversity with Methods for Automated and Accurate Analysis of Cell Signals (MAAACS). *PLoS Comput. Biol.* **9**, 24–26 (2013).
17. Previte, D. M. *et al.* Reactive oxygen species are required for driving efficient and sustained aerobic glycolysis during CD4+ T cell activation. *PLoS One* **12**, 1–22 (2017).
18. Wang, H. *et al.* Low-Voltage-Activated CaV3.1 Calcium Channels Shape T Helper Cell Cytokine Profiles. *Immunity* **44**, 782–794 (2016).

19. Feske, S., Wulff, H. & Skolnik, E. Y. *Ion Channels in Innate and Adaptive Immunity*. *Annual Review of Immunology* vol. 33 (2015).
20. Trebak, M. & Kinet, J. P. Calcium signalling in T cells. *Nat. Rev. Immunol.* **19**, 154–169 (2019).
21. Sia, S. K. & Whitesides, G. M. Review Microfluidic devices fabricated in poly (dimethylsiloxane) for biological studies. *Electrophoresis* **24**, 3563–3576 (2003).
22. Cai, D. K., Neyer, A., Kuckuk, R. & Heise, H. M. Optical absorption in transparent PDMS materials applied for multimode waveguides fabrication. *Opt. Mater. (Amst).* **30**, 1157–1161 (2008).
23. Fittipaldi, S., Dimauro, I., Mercatelli, N. & Caporossi, D. Role of exercise-induced reactive oxygen species in the modulation of heat shock protein response. **5762**, (2014).
24. Galadari, S., Rahman, A., Pallichankandy, S. & Thayyullathil, F. Reactive oxygen species and cancer paradox: To promote or to suppress? *Free Radic. Biol. Med.* **104**, 144–164 (2017).
25. Xia, Q. & Nyberg, T. Inhibition of cortical neural networks using infrared laser. *J. Biophotonics* 1–12 (2019) doi:10.1002/jbio.201800403.
26. Liljemalm, R. & Nyberg, T. Damage criteria for cerebral cortex cells subjected to hyperthermia. *Int. J. Hyperth.* **32**, 704–712 (2016).
27. Liljemalm, R. & Nyberg, T. Quantification of a thermal damage threshold for astrocytes using infrared laser generated heat gradients. *Ann. Biomed. Eng.* **42**, 822–832 (2014).
28. Nakata, Y., Osawa, K. & Miyanaga, N. Utilization of the high spatial-frequency component in adaptive beam shaping by using a virtual diagonal phase grating. *Sci. Rep.* **9**, 2–6 (2019).
29. Liang, J., Kohn, R. N., Becker, M. F. & Heinzen, D. J. High-precision laser beam shaping using a binary-amplitude spatial light modulator. *Appl. Opt.* **49**, 1323–1330 (2010).
30. Saenko, Y. V., Glushchenko, E. S., Zolotovskii, I. O., Sholokhov, E. & Kurkov, A. Mitochondrial dependent oxidative stress in cell culture induced by laser radiation at 1265 nm. *Lasers Med. Sci.* **31**, 405–413 (2016).
31. Sokolovski, S. G. *et al.* Infrared laser pulse triggers increased singlet oxygen production in tumour cells. *Sci. Rep.* **3**, (2013).
32. Anquez, F., El Yazidi-Belkoura, I., Randoux, S., Suret, P. & Courtade, E. Cancerous cell death from sensitizer free photoactivation of singlet oxygen. *Photochem. Photobiol.* **88**, 167–174 (2012).
33. Schroeder, P. *et al.* Cellular response to infrared radiation involves retrograde mitochondrial signaling. *Free Radic. Biol. Med.* **43**, 128–135 (2007).
34. Zastrow, L. *et al.* The missing link - Light-induced (280-1,600 nm) free radical formation in human skin. *Skin Pharmacol. Physiol.* **22**, 31–44 (2009).
35. Darvin, M. E. *et al.* Radical production by infrared A irradiation in human tissue. *Skin Pharmacol. Physiol.* **23**, 40–46 (2010).
36. Piazena, H. *et al.* Effects of water-filtered infrared-A and of heat on cell death, inflammation, antioxidative potential and of free radical formation in viable skin - First results. *J. Photochem. Photobiol. B Biol.* **138**, 347–354 (2014).
37. Zorov, D. B., Juhaszova, M. & Sollott, S. J. Mitochondrial ROS-induced ROS release: An update and review. *Biochim. Biophys. Acta - Bioenerg.* **1757**, 509–517 (2006).
38. Passarella, S. & Karu, T. Absorption of monochromatic and narrow band radiation in the visible and

near IR by both mitochondrial and non-mitochondrial photoacceptors results in photobiomodulation This paper is devoted to the memory of Prof. Lorenzo Bolognani who was one of the pioneers in the field of photobiomodulation. *J. Photochem. Photobiol. B Biol.* **140**, 344–358 (2014).

39. Hamblin, M. R., Huang, Y. Y., Sharma, S. K. & Carroll, J. Biphasic dose response in low level light therapy - an update. *Dose-Response* **9**, 602–618 (2011).
40. Huang, Y. Y., Chen, A. C. H., Carroll, J. D. & Hamblin, M. R. Biphasic dose response in low level lightherapy. *Dose-Response* **7**, 358–383 (2009).
41. Marcus, R. A. & Sutin, N. Electron transfers in chemistry and biology. *BBA Rev. Bioenerg.* **811**, 265–322 (1985).
42. Karu, T. I. Multiple roles of cytochrome c oxidase in mammalian cells under action of red and IR-A radiation. *IUBMB Life* **62**, 607–610 (2010).
43. Karu, T. I., Pyatibrat, L. V., Kolyakov, S. F. & Afanasyeva, N. I. Absorption measurements of a cell monolayer relevant to phototherapy: Reduction of cytochrome c oxidase under near IR radiation. *J. Photochem. Photobiol. B Biol.* **81**, 98–106 (2005).
44. Karu, T. Is it time to consider photobiomodulation as a drug equivalent? *Photomed. Laser Surg.* **31**, 189–191 (2013).
45. Karu, T. I., Pyatibrat, L. V. & Kalendo, G. S. Photobiological modulation of cell attachment via cytochrome c oxidase. *Photochem. Photobiol. Sci.* **3**, 211–216 (2004).
46. Zuckerbraun, B. S. *et al.* Carbon monoxide signals via inhibition of cytochrome c oxidase and generation of mitochondrial reactive oxygen species. *FASEB J.* **21**, 1099–1106 (2007).
47. Borutaite, V., Budriunaite, A. & Brown, G. C. Reversal of nitric oxide-, peroxynitrite- and S-nitrosothiol-induced inhibition of mitochondrial respiration or complex I activity by light and thiols. *Biochim. Biophys. Acta - Bioenerg.* **1459**, 405–412 (2000).
48. Moncada, S. & Bolaños, J. P. Nitric oxide, cell bioenergetics and neurodegeneration. *J. Neurochem.* **97**, 1676–1689 (2006).
49. Boelens, R., Wever, R., Van Gelder, B. F. & Rademaker, H. An EPR study of the photodissociation reactions of oxidised cytochrome c oxidase-nitric oxide complexes. *BBA - Bioenerg.* **724**, 176–183 (1983).
50. Kim, H. P. Lightening up Light Therapy- Activation of Retrograde Signaling Pathway by Photobiomodulation. 491–496 (2014).
51. Karu, T. I. & Kolyakov, S. F. Exact action spectra for cellular responses relevant to phototherapy. *Photomed. Laser Surg.* **23**, 355–361 (2005).
52. Collman, J. P. *et al.* Interaction of nitric oxide with a functional model of cytochrome c oxidase. *Proc. Natl. Acad. Sci. U. S. A.* **105**, 9892–9896 (2008).
53. Vos, M. H. & Liebl, U. Time-resolved infrared spectroscopic studies of ligand dynamics in the active site from cytochrome c oxidase. *Biochim. Biophys. Acta - Bioenerg.* **1847**, 79–85 (2015).
54. Hamblin, M. R. Mechanisms and applications of the anti-inflammatory effects of photobiomodulation. *AIMS Biophys.* **4**, 337–361 (2017).
55. Wang, X., Tian, F., Soni, S. S., Gonzalez-Lima, F. & Liu, H. Interplay between up-regulation of cytochrome-c-oxidase and hemoglobin oxygenation induced by near-infrared laser. *Sci. Rep.* **6**, 1–10

(2016).

56. Sanderson, T. H. *et al.* Inhibitory modulation of cytochrome c oxidase activity with specific near-infrared light wavelengths attenuates brain ischemia/reperfusion injury. *Sci. Rep.* **8**, 1–12 (2018).
57. Frossi, B., De Carli, M., Piemonte, M. & Pucillo, C. Oxidative microenvironment exerts an opposite regulatory effect on cytokine production by Th1 and Th2 cells. *Mol. Immunol.* **45**, 58–64 (2008).
58. Kamiński, M. M. *et al.* Mitochondrial Reactive Oxygen Species Control T Cell Activation by Regulating IL-2 and IL-4 Expression: Mechanism of Ciprofloxacin-Mediated Immunosuppression. *J. Immunol.* **184**, 4827–4841 (2010).
59. Fu, G. *et al.* Suppression of Th17 cell differentiation by misshapen/ NIK-related kinase MINK1. *J. Exp. Med.* **214**, 1453–1469 (2017).
60. Jackson, S. H., Devadas, S., Kwon, J., Pinto, L. A. & Williams, M. S. T cells express a phagocyte-type NADPH oxidase that is activated after T cell receptor stimulation. *Nat. Immunol.* **5**, 818–827 (2004).
61. Johnson, D. A., Amirahmadi, S., Ward, C., Fabry, Z. & Johnson, J. A. The absence of the pro-antioxidant transcription factor Nrf2 exacerbates experimental autoimmune encephalomyelitis. *Toxicol. Sci.* **114**, 237–246 (2009).
62. Kuo, P. C. *et al.* 3H-1,2-dithiole-3-thione as a novel therapeutic agent for the treatment of experimental autoimmune encephalomyelitis. *Brain. Behav. Immun.* **57**, 173–186 (2016).

Chapter 6

Discussion: Future application

6.1 Laser adjuvant followed by vaccination

This study developed two optical systems for observing the behaviour of immune cells induced by NIR laser light, revealing the effect of light on biological immunity. The NIR fluorescence imaging system visualised the behaviour of vaccine molecules. In addition to the intradermally administrated vaccine that was presented in this paper, it is also possible to visualise intramuscularly injected vaccines. Most of the vaccines used in clinic today are intramuscularly administrated; however, its mechanism has yet to be revealed, owing to the lack of a proper tool to observe the dynamics of immune cells.[1,2] It is highly expected that the novel system can resolve these mysteries.

The dual laser irradiation system clarified the immediate reaction of intracellular molecules in response to NIR laser irradiation. The uniqueness of the system is that two lasers at different wavelengths are simultaneously irradiated on mouse-derived T cells. The beam shapes were adjusted to be focused and square at the focal point. Gradients were given for these irradiances in order to determine the best combination of irradiances to induce photobiomodulation. As a result, 300 mW/cm^2 of the 1064-nm and 50 mW/cm^2 of the 1270-nm laser generated a notable reduction of intracellular ROS and calcium ion accumulation. This system can be readily deployed with other wavelengths, cell types and intracellular molecules, and is expected to provide a platform for clarifying the biological effects of NIR light.

The adjuvant effect of NIR light as a potential intradermal influenza vaccine was discovered in 2013.[3] Kashiwagi *et al*. demonstrated that brief exposure of the skin to a NIR CW laser followed by influenza H1N1 vaccination prompted the acquisition of protective immunity against the viral infection. Interestingly, they also demonstrated that the same energy of a PW laser at the same wavelength does not have the same outcome as the CW laser, indicating the complexity of photobiomodulation. They also determined that the migration of DCs is attributable to the laser adjuvant effect[4]; however, there is limited understanding of the relationship between the dynamics of vaccines, such as speed, amount and destination, and the efficacy of vaccines. This thesis demonstrated a cell-tracking method for identifying the destination of vaccine molecules in real time, noninvasively.[5] The advantage of the NIR fluorophore is its depth of penetration, which can visualise vaccines regardless of how it is administrated: intravenously, intradermally or intramuscularly. Such an optical platform contributes to revealing the mechanisms and dynamics of the immune response induced by the NIR laser.

Kimizuka *et al*. developed a handheld NIR laser device with a small semiconductor laser diode that has allowed its use by medical experts in examination rooms or operation rooms.[6] The small laser device also demonstrated the same adjuvant effect as previously reported.[3] The user-friendly device could contribute to improving the safety and efficacy of vaccination.[3,4,7,8] Furthermore, Kimizuka *et al*. also showed that the different wavelengths and irradiances of NIR laser light act as an adjuvant. These findings indicate the difficulty of finding the best condition of laser irradiation: wavelength, irradiance and laser duration time. To address this problem, the optical system could be used.[9] The platform may contribute to changing the medical practice with regard to mass immunisation.

6.2 T cell activation by near infrared laser

T cells play exceptionally important roles in the immune system against fatal diseases such as infections, auto immune diseases or cancers.[10–12] The proposed system could also be used to identify a laser parameter to augment anti-tumour response. It is well established that T cells play a critical role in anti-tumour immunity. Cancer is known to produce high amounts of ROS, which suppress the immune function of T cells. Consistently, cellular antioxidant levels have been demonstrated to be critical for the anti-tumour function of T cells in the immunosuppressive tumour microenvironment. A recent study has shown that central memory

T cells with higher cytosolic glutathione, surface thiol and intracellular antioxidant levels survive longer in tumours and control tumour growth better than effector memory T cells with less antioxidant levels, and that treatment with antioxidants improved the function of tumour-infiltrating T lymphocytes (TILs), leading to the prolonged survival of patients receiving these treated TILs.[13]

The clinical outcomes of novel cancer immunotherapies, such as anti-PD-1, PD-L1 and CTLA-4 antibody therapy,[14] are highly dependent on the condition of the tumour microenvironment.[15–18] It has been demonstrated that the PD-1 signal in T cells downregulates anti-tumour immunity by suppressing mitochondrial activities.[19] Mitochondrial activities and ROS generation are key functions used to synergise tumour regression by PD-1, PD-L1, CTLA-4 blockade.[20,21] Therefore, to date, many studies have focused on regulating dysfunction in mitochondrial metabolism and seeking to establish a new cancer therapeutic method.[22,23] Considering that simultaneous dual NIR laser irradiation suppresses the expression of ROS and Ca^{2+}, which are representatives of cellular metabolism, it is possible to hypothesise that the exposure of tumours to NIR laser light could stimulate antitumor activities in TILs.

In addition to the antibody administration cancer therapy, cellular therapies are also attracting attention.[14] Currently, chimeric antigen receptor (CAR) T cell therapy for B cell lymphoma has been approved by the FDA.[24] Patient-derived T cell genes are modified to express a protein called CAR and to recognise and attack specific antigens expressed on the surface of cancer cells. The T cells that are able to produce CAR are called CAR-T cells. CAR-T cell therapy treats refractory cancer by administrating CAR-T cells to patients.[25,26] To achieve a clinical outcome, efficient and timely T cell expansion is required for the culturing process of CAR-T cells.[27] It is known that the expansion of activated T cells is regulated by nitric oxygen in LNs or secondary lymphoid organs.[28] Considering that the NIR laser may unbound NO from COX, it may also be possible to breed NO, which is stored in COX to T cell cytosol that leads to T cell proliferation *ex vivo*[9]. In addition, the adaptive transfer of T cells in which lower mitochondrial membrane potential has shown long-term survival and antitumor immunity.[29] Although CAR-T cell therapy is only applicable for hematologic tumours at present, laser-armed T cells could target solid tumours in this way.[28]

In short, the optical platform reported by current studies has great potential to resolve the mystery of immune reactions. The platform is highly anticipated to elucidate further mechanisms of photobiomodulation via the physical effect of NIR light on the system.

Reference

1. Liang, F. & Loré, K. Local innate immune responses in the vaccine adjuvant-injected muscle. *Clin. Transl. Immunol.* **5**, e74 (2016).
2. Egemen, A. *et al.* Low-dose intradermal versus intramuscular administration of recombinant hepatitis B vaccine: A comparison of immunogenicity in infants and preschool children. *Vaccine* **16**, 1511–1515 (1998).
3. Kashiwagi, S. *et al.* Near-infrared laser adjuvant for influenza vaccine. *PLoS One* **8**, (2013).
4. Morse, K. *et al.* Near-Infrared 1064 nm Laser Modulates Migratory Dendritic Cells To Augment the Immune Response to Intradermal Influenza Vaccine. *J. Immunol.* ji1601873 (2017) doi:10.4049/jimmunol.1601873.
5. Katagiri, W. *et al.* Real-Time Imaging of Vaccine Biodistribution Using Zwitterionic NIR Nanoparticles. *Adv. Healthc. Mater.* **8**, e1900035 (2019).
6. Kimizuka, Y. *et al.* Semiconductor diode laser device adjuvanting intradermal vaccine. *Vaccine* **35**, 2404–2412 (2017).
7. Kashiwagi, S., Brauns, T. & Poznansky, M. C. Classification of Laser Vaccine Adjuvants. *J. Vaccines* **7**, 1–11 (2016).
8. Kashiwagi, S., Brauns, T., Gelfand, J. & Poznansky, M. C. Laser vaccine adjuvants: History, progress, and potential. *Hum. Vaccines Immunother.* **10**, 1892–1907 (2014).
9. Katagiri, W. *et al.* High-throughput single-cell live imaging of photobiomodulation with multispectral near-infrared lasers in cultured T cells. *J. Biomed. Opt.* **25**, 036003 (2020).
10. Wherry, E. J. & Kurachi, M. Molecular and cellular insights into T cell exhaustion. *Nat. Rev. Immunol.* **15**, 486–499 (2015).
11. Sun, J. C. & Bevan, M. J. Defective CD8 T cell memory following acute infection without CD4 T cell help. *Science (80-.).* **300**, 339–342 (2003).
12. Asano, M., Toda, M., Sakaguchi, N. & Sakaguchi, S. Autoimmune Disease as a Consequence of Developmental Abnormality of a T Cell Subpopulation. *J. Exp. Med.* **184**, 384–396 (1996).
13. Scheffel, M. J. *et al.* Efficacy of adoptive T-cell therapy isimproved by treatment with the antioxidant N-acetyl cysteine, which limits activation-induced T-cell death. *Cancer Res.* **76**, 6006–6016 (2016).
14. Waldman, A. D., Fritz, J. M. & Lenardo, M. J. A guide to cancer immunotherapy: from T cell basic science to clinical practice. *Nat. Rev. Immunol.* 1–18 (2020) doi:10.1038/s41577-020-0306-5.
15. Liu, X. & Cho, W. C. Precision medicine in immune checkpoint blockade therapy for non-small cell lung cancer. *Clin. Transl. Med.* **6**, 4–7 (2017).
16. Gajewski, T. F., Schreiber, H. & Fu, Y.-X. Innate and adaptive immune cells in the tumor microenvironment. *Nat. Immunol.* **14**, 1014–1022 (2013).
17. Petitprez, F. *et al.* Quantitative Analyses of the Tumor Microenvironment Composition and Orientation in the Era of Precision Medicine. *Front. Oncol.* **8**, 1–6 (2018).
18. Nirschl, C. J. *et al.* IFNγ-Dependent Tissue-Immune Homeostasis Is Co-opted in the Tumor Microenvironment. *Cell* **170**, 127-141.e15 (2017).

19. Chowdhury, P. S., Chamoto, K. & Honjo, T. Combination therapy strategies for improving PD-1 blockade efficacy: a new era in cancer immunotherapy. *J. Intern. Med.* **283**, 110–120 (2018).
20. Chamoto, K. *et al.* Mitochondrial activation chemicals synergize with surface receptor PD-1 blockade for T cell-dependent antitumor activity. *Proc. Natl. Acad. Sci.* **114**, E761–E770 (2017).
21. Luan, Y. Y. *et al.* Effect of regulatory T cells on promoting apoptosis of t lymphocyte and its regulatory mechanism in sepsis. *J. Interf. Cytokine Res.* **35**, 969–980 (2015).
22. Pustylnikov, S., Costabile, F., Beghi, S. & Facciabene, A. Targeting mitochondria in cancer: current concepts and immunotherapy approaches. *Transl. Res.* **202**, 35–51 (2018).
23. Marrache, S., Tundup, S., Harn, D. A. & Dhar, S. Ex vivo programming of dendritic cells by mitochondria-targeted nanoparticles to produce interferon-gamma for cancer immunotherapy. *ACS Nano* **7**, 7392–7402 (2013).
24. Golchin, A. & Farahany, T. Z. Biological Products: Cellular Therapy and FDA Approved Products. *Stem Cell Rev. Reports* **15**, 166–175 (2019).
25. Barrett, D. M., Singh, N., Porter, D. L., Grupp, S. A. & June, C. H. Chimeric Antigen Receptor Therapy for Cancer. *Annu. Rev. Med.* **65**, 333–347 (2014).
26. June, C. H. & Sadelain, M. Chimeric antigen receptor therapy. *N. Engl. J. Med.* **379**, 64–73 (2018).
27. Gilham, D. E., Debets, R., Pule, M., Hawkins, R. E. & Abken, H. CAR-T cells and solid tumors: Tuning T cells to challenge an inveterate foe. *Trends Mol. Med.* **18**, 377–384 (2012).
28. Jackson, H. J. *et al.* Driving CAR T-cells forward. *Nat. Rev. Clin. Oncol.* **13**, 370–383 (2017).
29. Sukumar, M. *et al.* Mitochondrial Membrane Potential Identifies Cells with Enhanced Stemness for Cellular Therapy. *Cell Metab.* **23**, 63–76 (2016).

Acknowledgement

First of all, I would like to offer my gratitude to Prof. Kosuke Tsukada for the continuous support over five years during my master's and Ph.D. programme at the Faculty of Science and Technology, Keio University, Japan.

I would like to thank Prof. Hak Soo Choi, Prof. Satoshi Kashiwagi, Prof. Georges El Fakhri, Prof. Marc-André Tétrault, Dr. Homan Kang, Dr. Kai Bao, Dr. Kate G. Park, Dr. Shuang Hu, Dr. Shinsuke Nomura, Dr. Takeshi Fukuda, Mr. Shinya Yokomizo and all our collaborators and labmates at the Gordon Center for Medical Imaging, Massachusetts General Hospital, USA. I am grateful for their kind support, scientific discussions and ideas. I also thank Prof. Conor L. Evans and Dr. Sinyoung Jeong at the Wellman Center for Photomedicine, Massachusetts General Hospital, for giving me advice and for supporting the DLS analysis.

I would also like to thank Mr. Akira Tanushi at the Massachusetts Institute of Technology, USA, for the kind help regarding TDDFT computational simulation, and Dr. GeonHui Lee at the United States National Institute of Health (NIH) for providing wonderful ideas about the PDMS device.

I would like to thank my previous supervisors during my bachelor's and master's course: Prof. Tsunenori Arai at the Faculty of Science and Technology, Keio University; and Prof. Tobias Nyberg at the Department of Biomedical Engineering and Health Systems, Loyal Institute of Technology (KTH), Sweden.

I would like to thank Prof. Fumihiko Kannari and the Keio Program for Leading Graduate School (all-round), a cutting-edge programme that cultivates the integration of arts and sciences and educates the next generation of leaders.

Finally, to the countless number of people involved in the project, and to my family and all my friends, who cannot be listed here, I sincerely thank you all. Nothing could have been achieved without your faithful support and understanding.

Appendix

A. Copyright permission

The figures and sentences in this thesis were partially reproduced with permission from two journals[1,2].

[1] Katagiri, W., Lee, J.H., Tétrault, M., Kang, H., Jeong, S., Evans, C.L., Yokomizo, S., Santos, S., Jones, C., et al., "Real-Time Imaging of Vaccine Biodistribution Using Zwitterionic NIR Nanoparticles," Advanced Healthcare Materials 8(15), e1900035 (2019).

[2] Katagiri, W., Lee, G., Tanushi, A., Tsukada, K., Choi, H.S., and Kashiwagi, S., "High-throughput single-cell live imaging of photobiomodulation with multispectral near-infrared lasers in cultured T cells," Journal of Biomedical Optics 25(3), (2020).

B. Software program for T cell analysis

```
import numpy as np
import cv2
from tqdm import tqdm

def FindCenter(img_gauss, img_raw, threshold, kernel):
    array = []
    for x in range(kernel, img_gauss.shape[0]-kernel):
        for y in range(kernel, img_gauss.shape[1]-kernel):
            if threshold <= img_gauss[x, y] < 4095 and img_gauss[x, y] == np.max(img_gauss[x -
kernel:x + kernel, y - kernel:y + kernel]):
                array.append([x, y, img_raw[x, y]])
    return array

def FindSameCell(array_0min, array_1min, pixel):
    array = []
    adjust = 1.0
    array_0 = array_0min
    array_1 = array_1min
    len_0 = array_0.shape[0]
    len_1 = array_1.shape[0]
    for x_0 in tqdm(range(0, len_0)):
        for x_1 in range(0, len_1):
            if array_1[x_1, 0] - 1 * pixel <= array_0[x_0, 0] <= array_1[x_1, 0] + 1 * pixel and
array_1[x_1, 1] - 1 * pixel <= array_0[x_0, 1] <= array_1[x_1, 1] + 1 * pixel:
                if 0.7 < array_1[x_1, 2] * adjust / array_0[x_0, 2] < 1.3:
                    array.append([array_0[x_0, 0], array_0[x_0, 1], array_1[x_1, 2] * adjust / array_0[x_0,
2]])
    array = np.array(array)
    return array

def ConvertPixel(array):
    new_array = []

### For High

    B0_1064 = 384.3
    B1_1064 = 0.1546
    B2_1064 = -0.0007934
    B3_1064 = 9.238*10**-7
    B4_1064 = -3.934*10**-10

    B0_1270 = 95.82
    B1_1270 = 0.02091
    B2_1270 = -4.679*10**-5
```

```
    for i in range(len(array)):
        x = 1250 * array[i][1]/742
        new_x = B0_1064 + B1_1064 * x + B2_1064 * x**2 + B3_1064 * x**3 + B4_1064 * x**4
        y = 1250 * array[i][0]/742
        new_y = B0_1270 + B1_1270 * y + B2_1270 * y**2
        new_array.append([new_x, new_y, array[i][2]])
    return new_array

def DataSort(array, threshold):
    global A1_x, A1_y, A2_x, A2_y, A3_x, A3_y, A4_x, A4_y, A5_x, A5_y, B1_x, B1_y, B2_x,
B2_y, B3_x, B3_y, B4_y, B5_x, B5_y, C1_x, C1_y, C2_x, C2_y, C3_x, C4_y, C5_x, C5_y, D1_x,
D1_y, D2_x, D2_y, D3_x, D4_y, D5_x, D5_y, E1_x, E1_y, E2_x, E2_y, E3_x, E4_y, E5_x, E5_y
    array_sorted = []
    length = len(array)
    for x in range(0, length):
        A1 = A2 = A3 = A4 = A5 = A6 = B1 = B2 = B3 = B4 = B5 = B6 = C1 = C2 = C3 = C4 = C5 =
C6 = D1 = D2 = D3 = D4 = D5 = D6 = E1 = E2 = E3 = E4 = E5 = E6 = F1 = F2 = F3 = F4 = F5 = F6
= 0
        A1_x = A1_y = A2_x = A2_y = A3_x = A3_y = A4_x = A4_y = A5_x = A5_y = B1_x = B1_y
= B2_x = B2_y = B3_x = B3_y = B4_x = B4_y = B5_x = B5_y = C1_x = C1_y = C2_x = C2_y =
C3_x = C3_y = C4_x = C4_y = C5_x = C5_y = D1_x = D1_y = D2_x = D2_y = D3_x = D3_y =
D4_x = D4_y = D5_x = D5_y = E1_x = E1_y = E2_x = E2_y = E3_x = E3_y = E4_x = E4_y = E5_x
= E5_y = 0
        if array[x][0] == array[x-1][0] and array[x][1] == array[x-1][1]:
            continue
        else:
            if array[x][2] < threshold:
                if 250 + 30.0 * 4 < array[x][0] < 250 + 30.0 * 5 and 100 - 10 * 1 <= array[x][1] < 100 - 10 *
0:
                    A1 = array[x][2]
                    A1_x = array[x][0]
                    A1_y = array[x][1]
                elif 250 + 30.0 * 4 <= array[x][0] < 250 + 30.0 * 5 and 100 - 10 * 2 <= array[x][1] < 100 -
10 * 1:
                    A2 = array[x][2]
                    A2_x = array[x][0]
                    A2_y = array[x][1]
                elif 250 + 30.0 * 4 <= array[x][0] < 250 + 30.0 * 5 and 100 - 10 * 3 <= array[x][1] < 100 -
10 * 2:
                    A3 = array[x][2]
                    A3_x = array[x][0]
                    A3_y = array[x][1]
                elif 250 + 30.0 * 4 <= array[x][0] < 250 + 30.0 * 5 and 100 - 10 * 4 <= array[x][1] < 100 -
10 * 3:
                    A4 = array[x][2]
                    A4_x = array[x][0]
                    A4_y = array[x][1]
```

```
        elif 250 + 30.0 * 4 <= array[x][0] < 250 + 30.0 * 5 and 100 - 10 * 5 <= array[x][1] < 100 -
10 * 4:
            A5 = array[x][2]
            A5_x = array[x][0]
            A5_y = array[x][1]
        elif 250 + 30.0 * 3 < array[x][0] < 250 + 30.0 * 4 and 100 - 10 * 1 <= array[x][1] < 100 - 10
* 0:
            B1 = array[x][2]
            B1_x = array[x][0]
            B1_y = array[x][1]
        elif 250 + 30.0 * 3 <= array[x][0] < 250 + 30.0 * 4 and 100 - 10 * 2 <= array[x][1] < 100 -
10 * 1:
            B2 = array[x][2]
            B2_x = array[x][0]
            B2_y = array[x][1]
        elif 250 + 30.0 * 3 <= array[x][0] < 250 + 30.0 * 4 and 100 - 10 * 3 <= array[x][1] < 100 -
10 * 2:
            B3 = array[x][2]
            B3_x = array[x][0]
            B3_y = array[x][1]
        elif 250 + 30.0 * 3 <= array[x][0] < 250 + 30.0 * 4 and 100 - 10 * 4 <= array[x][1] < 100 -
10 * 3:
            B4 = array[x][2]
            B4_x = array[x][0]
            B4_y = array[x][1]
        elif 250 + 30.0 * 3 <= array[x][0] < 250 + 30.0 * 4 and 100 - 10 * 5 <= array[x][1] < 100 -
10 * 4:
            B5 = array[x][2]
            B5_x = array[x][0]
            B5_y = array[x][1]
        elif 250 + 30.0 * 2 < array[x][0] < 250 + 30.0 * 3 and 100 - 10 * 1 <= array[x][1] < 100 - 10
* 0:
            C1 = array[x][2]
            C1_x = array[x][0]
            C1_y = array[x][1]
        elif 250 + 30.0 * 2 <= array[x][0] < 250 + 30.0 * 3 and 100 - 10 * 2 <= array[x][1] < 100 -
10 * 1:
            C2 = array[x][2]
            C2_x = array[x][0]
            C2_y = array[x][1]
        elif 250 + 30.0 * 2 <= array[x][0] < 250 + 30.0 * 3 and 100 - 10 * 3 <= array[x][1] < 100 -
10 * 2:
            C3 = array[x][2]
            C3_x = array[x][0]
            C3_y = array[x][1]
        elif 250 + 30.0 * 2 <= array[x][0] < 250 + 30.0 * 3 and 100 - 10 * 4 <= array[x][1] < 100 -
10 * 3:
            C4 = array[x][2]
```

```
            C4_x = array[x][0]
            C4_y = array[x][1]
        elif 250 + 30.0 * 2 <= array[x][0] < 250 + 30.0 * 3 and 100 - 10 * 5 <= array[x][1] < 100 -
10 * 4:
            C5 = array[x][2]
            C5_x = array[x][0]
            C5_y = array[x][1]
        elif 250 + 30.0 * 1 < array[x][0] < 250 + 30.0 * 2 and 100 - 10 * 1 <= array[x][1] < 100 - 10
* 0:
            D1 = array[x][2]
            D1_x = array[x][0]
            D1_y = array[x][1]
        elif 250 + 30.0 * 1 <= array[x][0] < 250 + 30.0 * 2 and 100 - 10 * 2 <= array[x][1] < 100 -
10 * 1:
            D2 = array[x][2]
            D2_x = array[x][0]
            D2_y = array[x][1]
        elif 250 + 30.0 * 1 <= array[x][0] < 250 + 30.0 * 2 and 100 - 10 * 3 <= array[x][1] < 100 -
10 * 2:
            D3 = array[x][2]
            D3_x = array[x][0]
            D3_y = array[x][1]
        elif 250 + 30.0 * 1 <= array[x][0] < 250 + 30.0 * 2 and 100 - 10 * 4 <= array[x][1] < 100 -
10 * 3:
            D4 = array[x][2]
            D4_x = array[x][0]
            D4_y = array[x][1]
        elif 250 + 30.0 * 1 <= array[x][0] < 250 + 30.0 * 2 and 100 - 10 * 5 <= array[x][1] < 100 -
10 * 4:
            D5 = array[x][2]
            D5_x = array[x][0]
            D5_y = array[x][1]
        elif 250 + 30.0 * 0 < array[x][0] < 250 + 30.0 * 1 and 100 - 10 * 1 <= array[x][1] < 100 - 10
* 0:
            E1 = array[x][2]
            E1_x = array[x][0]
            E1_y = array[x][1]
        elif 250 + 30.0 * 0 <= array[x][0] < 250 + 30.0 * 1 and 100 - 10 * 2 <= array[x][1] < 100 -
10 * 1:
            E2 = array[x][2]
            E2_x = array[x][0]
            E2_y = array[x][1]
        elif 250 + 30.0 * 0 <= array[x][0] < 250 + 30.0 * 1 and 100 - 10 * 3 <= array[x][1] < 100 -
10 * 2:
            E3 = array[x][2]
            E3_x = array[x][0]
            E3_y = array[x][1]
```

```
            elif 250 + 30.0 * 0 <= array[x][0] < 250 + 30.0 * 1 and 100 - 10 * 4 <= array[x][1] < 100 -
10 * 3:
                E4 = array[x][2]
                E4_x = array[x][0]
                E4_y = array[x][1]
            elif 250 + 30.0 * 0 <= array[x][0] < 250 + 30.0 * 1 and 100 - 10 * 5 <= array[x][1] < 100 -
10 * 4:
                E5 = array[x][2]
                E5_x = array[x][0]
                E5_y = array[x][1]
            else:
                print('error')
            array_sorted.append([A3_x, A3_y, A3, B3_x, B3_y, B3, C3_x, C3_y, C3, D3_x, D3_y, D3,
E3_x, E3_y, E3, A4_x, A4_y, A4, B4_x, B4_y, B4, C4_x, C4_y, C4, D4_x, D4_y, D4, E4_x, E4_y,
E4, A5_x, A5_y, A5, B5_x, B5_y, B5, C5_x, C5_y, C5, D5_x, D5_y, D5, E5_x, E5_y, E5])

    return array_sorted

ExpNumber = 1

threshold_1 = 433
threshold_2 = 990
threshold_3 = 4095

#identification to import images
# T cell images are saved such as "FITC_1001.tif"
# Here you choose combination of two images that you are interested as 0 min and a certain
timepoint.

Image_number_0min = 1001
Image_number_1 = 1002
Treat_No = 2
ID = 'High'
Minute = 1
allowed_pixel = 1

#"FITC" as Fluo-4 AM, "Red" as MitoSOX Red
Color = str('FITC')

for i in tqdm(range(1001, 1033)):

    img = cv2.imread("FITC_" + str(i) + ".tif", cv2.IMREAD_UNCHANGED)

    img_Gauss = cv2.GaussianBlur(img,(3,3),0)
    ret, img_bin = cv2.threshold(img_Gauss, threshold_1, 4095, cv2.THRESH_BINARY)
    array = FindCenter(img_Gauss, img, threshold_1, 2)
    np.savetxt('Result_No' +str(ExpNumber)+ '_FITC_' + str(i) + '.csv', array, delimiter=',', fmt="%s")
```

```
for i in tqdm(range(1001, 1033)):

    img = cv2.imread("RED_" + str(i) + ".tif", cv2.IMREAD_UNCHANGED)

    img_Gauss = cv2.GaussianBlur(img,(3,3),0)
    ret, img_bin = cv2.threshold(img_Gauss, threshold_2, 4095, cv2.THRESH_BINARY)
    array = FindCenter(img_Gauss, img, threshold_2, 2)
    np.savetxt('Result_No' +str(ExpNumber)+ '_RED_' + str(i) + '.csv', array, delimiter=',', fmt="%s")

for i in tqdm(range(2001, 2033)):

    img = cv2.imread("FITC_" +str(i)+ ".tif", cv2.IMREAD_UNCHANGED)

    img_Gauss = cv2.GaussianBlur(img,(3,3),0)
    ret, img_bin = cv2.threshold(img_Gauss, threshold_1, 4095, cv2.THRESH_BINARY)
    array = FindCenter(img_Gauss, img, threshold_1, 2)
    np.savetxt('Result_No' +str(ExpNumber)+ '_FITC_' + str(i) + '.csv', array, delimiter=',', fmt="%s")

for i in tqdm(range(2001, 2033)):

    img = cv2.imread("RED_" +str(i)+ ".tif", cv2.IMREAD_UNCHANGED)

    img_Gauss = cv2.GaussianBlur(img,(3,3),0)
    ret, img_bin = cv2.threshold(img_Gauss, threshold_2, 4095, cv2.THRESH_BINARY)
    array = FindCenter(img_Gauss, img, threshold_2, 2)
    np.savetxt('Result_No' + str(ExpNumber) + '_RED_' + str(i) + '.csv', array, delimiter=',', fmt="%s")


img_0min = open('Result_No' +str(ExpNumber)+ '_' + Color + '_' +str(Image_number_0min)+ '.csv',
'r')
img_0min = np.loadtxt(img_0min, delimiter=",")
img_1 = open('Result_No' +str(ExpNumber)+ '_' + Color + '_' +str(Image_number_1)+ '.csv', 'r')
img_1 = np.loadtxt(img_1, delimiter=",")

no_laser_img_0min = open('Result_No' +str(ExpNumber)+ '_' + Color + '_'
+str(Image_number_0min+1000)+ '.csv', 'r')
no_laser_img_0min = np.loadtxt(no_laser_img_0min, delimiter=",")
no_laser_img_1 = open('Result_No' +str(ExpNumber)+ '_' + Color + '_'
+str(Image_number_1+1000)+ '.csv', 'r')
no_laser_img_1 = np.loadtxt(no_laser_img_1, delimiter=",")

Array = []
Array = FindSameCell(img_0min, img_1, allowed_pixel)
Array_no_laser_1 = FindSameCell(no_laser_img_0min, no_laser_img_1, allowed_pixel)

Array = ConvertPixel(Array)
```

```
np.savetxt('Analysis_Result_No' + str(ExpNumber) + '_' + Color + '_' + str(ID) + '_No' +
str(Treat_No) + '_' + str(Minute) + 'min_Array_test.csv', Array, delimiter=',', fmt="%s")

Array_no_laser_2 = []
for x in range(0, len(Array_no_laser_1)):
   if Array_no_laser_1[x-1][0] != Array_no_laser_1[x][0] and Array_no_laser_1[x-1][1] !=
Array_no_laser_1[x][1]:
      Array_no_laser_2.append([Array_no_laser_1[x][0], Array_no_laser_1[x][1],
Array_no_laser_1[x][2]])

Array_sorted = DataSort(Array, threshold_3)
Array_sorted.insert(0, ['A1', 'A2', 'A3', 'A4', 'A5', 'A6', 'B1', 'B2', 'B3', 'B4', 'B5', 'B6', 'C1', 'C2', 'C3',
'C4', 'C5', 'C6', 'D1', 'D2', 'D3', 'D4', 'D5', 'D6', 'E1', 'E2', 'E3', 'E4', 'E5', 'E6', 'F1', 'F2', 'F3', 'F4', 'F5',
'F6', 'No Laser'])
np.savetxt('Analysis_Result_No' + str(ExpNumber) + '_' + Color + '_' + str(ID) + '_No' +
str(Treat_No) + '_' + str(Minute) + 'min.csv', Array_sorted, delimiter=',', fmt="%s")
np.savetxt('Analysis_Result_No' + str(ExpNumber) + '_' + Color + '_' + str(ID) + '_No' +
str(Treat_No) + '_' + str(Minute) + 'min_No_Laser.csv', Array_no_laser_2, delimiter=',', fmt="%s")
```

List of Publications

1. Journal papers (related to this thesis)

[1] W. Katagiri, J.H. Lee, M.-A. Tétrault, H. Kang, S. Jeong, C. L. Evans, S. Yokomizo, S. Santos, C. Jones, S. Hu, G.E. Fakhri, K. Tsukada, H. Choi, S. Kashiwagi, "Real-Time Imaging of Vaccine Biodistribution Using Zwitterionic NIR Nanoparticles," *Advanced Healthcare Materials*, **8**, e1900035 (2019).

[2] W. Katagiri, G.H. Lee, A. Tanushi, K. Tsukada, H.S. Choi, S. Kashiwagi, "High-throughput single-cell live imaging of photobiomodulation with multispectral near-infrared laser in cultured cells," *Journal of Biomedical Optics*, **25**, 3, 036003 (2020).

2. Other journal papers

[1] Y. Kimizuka, J.J. Callahan, Z. Huang, K. Morse, W. Katagiri, A. Shigeta, R. Bronson, S. Takeuchi, Y. Shimaoka, M.P.K. Chan, Y. Zeng, B. Li, H. Chen, R.Y.Y. Tan, C. Dwyer, T. Mulley, P. Leblanc, C. Goudie, J. Gelfand, K. Tsukada, T. Brauns, M.C. Poznansky, D. Bean, S. Kashiwagi, "Semiconductor diode laser device adjuvanting intradermal vaccine," *Vaccine*, **35**, 2404-2412 (2017).

[2] K. Morse, Y. Kimizuka, M.P.K. Chan, M. Shibata, Y. Shimaoka, S. Takeuchi, B. Forbes, C. Nirschl, B. Li, Y. Zeng, R.T. Bronson, W. Katagiri, A. Shigeta, R.F. Sîrbulescu, H. Chen, R.Y.Y. Tan, K. Tsukada, T. Brauns, J. Gelfand, A. Sluder, J.J. Locascio, M.C. Poznansky, N. Anandasabapathy, S. Kashiwagi, "Near-infrared 1064 nm laser modulates migratory dendritic cells to adjuvant the immune response to intradermal influenza vaccine," *Journal of Immunology*, **199**, 1319-1332 (2017).

[3] Y. Kimizuka, W. Katagiri, J.J. Locascio, A. Shigeta, Y. Sasaki, M. Shibata, K. Morse, F.R. Sirbulescu, M. Miyatake, P. Reeves, M. Suematsu, J. Gelfand, T. Brauns, M.C. Poznansky, K. Tsukada, S. Kashiwagi, "Brief exposure of skin to near-infrared laser modulates mast cell function and augments the immune response," *Journal of Immunology*, **12**, 3587-3603 (2018).

[4] G.K. Park, J.H. Lee, E. Soriano, M. Choi, K. Bao, W. Katagiri, D.Y. Kim, J.H. Paik, S.H. Yun, J.V. Frangioni, T.E. Clancy, S. Kashiwagi, M. Henary, H.S. Choi, "Rapid and Selective Targeting of Heterogeneous Pancreatic Neuroendocrine Tumors," *iScience*, **23**, 101006 (2020).

3. International conferences

[1] W. Katagiri, T. Nyberg, "Skin Damage Evaluation by Heat for the Safety of Laser Medical Devices," 39th Annual International Conference of the Institute of Electrical and Electronics Engineers (IEEE) Engineering in Medicine and Biology Society, ThDT2-05.3, Jeju, Republic of Korea, July 11-15 (2017).

[2] W. Katagiri, K. Tsukada, "Three-Dimensional in *vivo* Analysis of Histology for Low-Level Laser Therapy," 2017 Biomedical Engineering Society Annual Meeting, FRI-318, Phoenix, USA, October 11-14 (2017).

[3] W. Katagiri, J.H. Lee, M.-A. Tétrault, H. Kang, S. Hu, S. Kashiwagi, H.S. Choi, "Real-Time Tracking of Vaccination Using NIR Fluorescence Imaging," 16th Annual Celebration of Clinical Research, Massachusetts General Hospital, 146, Boston, USA, October 4 (2018).

[4] M.-A. Tétrault, H. Kang, W. Katagiri, S. Kashiwagi, G.E. Fakhri, H.S. Choi, "Path to a real-time, full dynamic range and high sensitivity quantitative optical imaging system for surgery assistance: the photon counting camera," 16th Annual Celebration of Clinical Research, Massachusetts General Hospital, 287, Boston, USA, October 4 (2018).

[5] W. Katagiri, H.S. Choi, S. Kashiwagi, "In vivo near-infrared imaging of vaccine biodistribution using zwitterionic fluorophore," World Molecular Imaging Congress 2019, LBP015, Montréal, Canada, September 4-7 (2019).

[6] W. Katagiri, J.H. Lee, M.-A. Tétrault, H. Kang, S. Hu, S. Kashiwagi, H.S. Choi, "Real-Time Tracking of Vaccine Uptake by Antigen Presenting Cells Using NIR Fluorescence Imaging," 17th Annual Celebration of Clinical Research, Massachusetts General Hospital (MGH), 155, Boston, USA, October 3 (2019).

[7] A.D. Ulumben, W. Katagiri, M.-A. Tétrault, Homan Kang, S. Kashiwagi, H.S. Choi, "Real-Time Imaging of Vaccine Using a Zwitterionic NIR Fluorophore,' 17th Annual Celebration of Clinical Research, Massachusetts General Hospital, 329, Boston, USA, October 3 (2019).

[8] W. Katagiri, M.-A. Tétrault, H. Kang, S. Kashiwagi, H.S. Choi, "Real-Time Imaging of Vaccine Biodistribution Using Zwitterionic NIR Nanoparticle," The Japan-US Science Forum in Boston 2019, 15, Boston, USA, November 2 (2019).

[9] S. Yokomizo, W. Katagiri, Y. Kimizuda, S. Kashiwagi, "Light Technology for Rapid Translation -Use of Near -infrared Light to Modulate Immunity for Immunotherapy," The Japan-US Science Forum in Boston 2019, 28, Boston, USA, November 2 (2019).

[10] W. Katagiri, M.-A. Tétrault, H. Kang, S. Jeong, C. L. Evans, S. Kashiwagi, H.S. Choi, "Vaccine visualization using a Zwitterionic near-infrared fluorophore," SPIE BIOS 2020, 11219-5, San Francisco, USA February 1-6 (2020) (invited).

[11] S. Kashiwagi, W. Katagiri, Y. Kimizuka, "A distinct role of skin-resident dendritic cells in augmenting the efficacy of intradermal vaccine with non-pulsed near-infrared laser adjuvant," SPIE BIOS 2020, 11241-3, San Francisco, USA February 1-6 (2020) (invited).

[12] X. Wu, W. Katagiri, E.J. McDonald, C. Yang, J.L. Guerrero, R. Ikegami, A. Ulumben, S. Long, S. Kashiwagi, H.S. Choi, F. Jaffer, G.E. Fakhri, R. Zaman, "Detection of early atherosclerotic plaques with TLR4-conjugated zwitterionic near-infrared fluorophore: a pilot mice study," Society of Nuclear Medicine and Molecular Imaging Annual Meeting 2020, 1831, July 11-14 (2020).

4. Domestic conferences

[1] 片桐渉, 浜田梨沙, 竹ノ谷洋海, 黒津真璃子, 小川恵美悠, 荒井恒憲, “Talaporfin sodium の細胞外光増感反応治療による末梢神経障害: in vitro における検討,” 第 54 回日本生体医工学会大会, S264-01 (名古屋, 2015.5.9).

[2] 浜田梨沙, 松崎亮太, 片桐渉, 竹ノ谷洋海, 黒津真璃子, 小川恵美悠, 荒井恒憲, “Talaporfin sodium の細胞が異光増刊反応による血管内皮細胞障害,” 第 54 回日本生体医工学会大会, S264-02 (名古屋, 2015.5.9).

[3] 片桐渉, 君塚善文, 柏木哲, 塚田孝祐, “近赤外半導体レーザーデバイスによる免疫活性化作用の検証,” 第 38 回日本レーザー医学会総会, P1-4, (横浜, 2017.11.10).

[4] 柏木哲, 君塚善文, 片桐渉, 塚田孝祐, “低出力レーザー研究の新たな展開 近赤外光を用いた非侵襲的ワクチンアジュバント,” 第 38 回日本レーザー医学会総会, M6-2 (横浜, 2017.11.11).

[5] 片桐渉, 君塚善文, 柏木哲, 塚田孝祐, “皮内投与型ワクチンの免疫賦活化に適した近赤外レーザーデバイスの開発,” 第 39 回日本レーザー医学会総会, P-2, (東京, 2018.11.2).